

©Copyright 2012

Jonathan T. Cox

New Electrochemical Methods for Studying Nanoparticle Electrocatalysis and Neuronal Exocytosis

Jonathan T. Cox

A dissertation
submitted in partial fulfillment of the
requirements for the degree of

Doctor of Philosophy

University of Washington

2012

Reading Committee:

Bo Zhang, Chair
Xiaosong Li
Frantisek Turecek

Program Authorized to Offer Degree:
Department of Chemistry

University of Washington

Abstract

New Electrochemical Methods for Studying Nanoparticle Electrocatalysis and Neuronal Exocytosis

Jonathan T. Cox

Chair of the Supervisory Committee:
Assistant Professor Bo Zhang
Department of Chemistry

This dissertation presents the construction and application of micro and nanoscale electrodes for electroanalytical analysis. The studies presented herein encompass two main areas: electrochemical catalysis, and studies of the dynamics of single cell exocytosis.

The first portion of this dissertation engages the use of Pt nanoelectrodes to study the stability and electrocatalytic properties of materials. A single nanoparticle electrode (SNPE) was fabricated by immobilizing a single Au nanoparticle on a Pt disk nanoelectrode via an amine-terminated silane cross linker. In this manner we were able to effectively study the electrochemistry and electrocatalytic activity of single Au nanoparticles and found that the electrocatalytic activity is dependent on nanoparticle size. This study can further the understanding of the structure-function relationship in nanoparticle based electrocatalysis. Further work was conducted to probe the stability of Pt nanoelectrodes under conditions of potential cycling. Pt based catalysts are known to deteriorate under such conditions due to losses in electrochemical surface area and Pt dissolution. By using Pt disk nanoelectrodes we were able to study Pt dissolution via steady-state voltammetry. We observed an enhanced dissolution rate and higher charge density on nanoelectrodes than that previously found on macro scale electrodes.

The goal of the second portion of this dissertation is to develop new analytical methods to study the dynamics of exocytosis from single cells. The secretion of neurotransmitters plays a key role in neuronal communication, and our studies highlight how bipolar electrochemistry can be employed to

enhance detection of neurotransmitters from single cells. First, we developed a theory to quantitatively characterize the voltammetric behavior of bipolar carbon fiber microelectrodes and secondly applied those principles to single cell detection. We showed that by simply adding an additional redox mediator to the back-fill solution of a carbon fiber microelectrode, there is a significant enhancement in detection. Additionally we used solid state nanopores to detect individual phospholipid vesicles in solution. Vesicles are key cellular components that play essential biological roles especially in neurotransmission. This work represents preliminary studies in detection and size determination from vesicles isolated from individual cells.

TABLE OF CONTENTS

List of Figures.....	iv
List of Tables.....	viii
Glossary.....	v
CHAPTER 1 INTRODUCTION.....	1
1.1. Microvoltammetric Electrodes.....	1
1.2. Methods of Characterization.....	2
1.2.1. Steady-State Voltammetry.....	2
1.2.2. Characterization by Electron Microscopy.....	4
1.2.3. Scanning Electrochemical Microscopy.....	4
1.2.4. Surface Adsorption and Charging.....	4
1.3. Development of Electrode Fabrication Techniques.....	5
1.3.1. Disk Nanoelectrode Fabrication.....	6
1.4. Electrochemical Approaches to Investigate Exocytosis.....	7
1.4.1. Constant Potential Amperometry.....	8
1.4.2. Fast Scan Cyclic Voltammetry.....	9
1.5. Tables and Figures.....	10
CHAPTER 2 INSTRUMENTATION AND FABRICATION.....	11
2.1. Reagents and Materials.....	11
2.2. Fabrication Methods.....	11
2.2.1. Fabrication of Pt Nanoelectrodes.....	12
2.2.2. Fabrication of Au and Pt Microelectrodes.....	12
2.2.3. Fabrication of Carbon Fiber Microelectrodes.....	13
2.2.4. Fabrication of Silica Nanochannels.....	13
2.3. Cyclic Voltammetry.....	14
2.4. Tables and Figures.....	15
CHAPTER 3 ELECTROCHEMICAL RESPONSES AND ELECTROCATALYSIS AT SINGLE Au NANOPARTICLES.....	20
3.1. Introduction.....	20
3.2. Experimental Section.....	22
3.2.1. Preparation and Characterization of Au Nanoparticles.....	22
3.2.2. Fabrication of Au Single Nanoparticle Electrodes.....	23
3.2.3. Transmission Electron Microscopy.....	23
3.3. Results and Discussion.....	23
3.3.1. TEM Characterization of Au SNPEs.....	23
3.3.2. Underpotential Deposition of Cu at Au SNPEs.....	24
3.3.3. Voltammetric Responses of Au SNPEs in H ₂ SO ₄	25
3.3.4. Steady-State Voltammetric Response at Au Nanoparticle arrays on a Pt UME.....	26
3.3.5. Steady-State Voltammetric Response at Au SNPEs.....	26
3.3.6. Oxygen Reduction at Single Au Nanoparticles.....	28
3.4. Conclusions.....	30
3.5. Tables and Figures.....	31

CHAPTER 4 STABILITY OF Pt NANOEELECTRODES IN A SULFURIC ACID SOLUTION UNDER POTENTIAL CYCLING 43

4.1. Introduction 43
4.2. Experimental Section 44
 4.2.1. Finite-Element Simulations 44
4.3. Results and Discussion 44
 4.3.1. Electrode Characterization 44
 4.3.2. Finite Element Simulations of the Steady-State Response of a Recessed Disk Nanoelectrode 45
 4.3.3. Pt Dissolution Under Potential Cycling 47
 4.3.4. SEM characterization of a Recessed Disk Nanoelectrode 48
 4.3.5. Mechanism of Pt Dissolution 49
 4.3.6. Determination of Pt Dissolution Rate 50
4.4. Conclusions 51
4.5. Tables and Figures 53

CHAPTER 5 STEADY-STATE VOLTAMMETRY OF A MICROELECTRODE IN A CLOSED BIPOLAR CELL 62

5.1. Introduction 62
5.2. Theory 64
5.3. Results and Discussion 68
 5.3.1. Steady-State Voltammetry of a Microelectrode in a Closed Bipolar Cell 68
 5.3.2. Is “Reversible Voltammetric Behavior Obtainable in a Bipolar Cell?” 70
5.4. Conclusions 73
5.5. Tables and Figures 74

CHAPTER 6 USING BIPOLAR ELECTROCHEMISTRY TO ENHANCE DETECTION OF EXOCYTOSIS FROM PC12 CELLS 83

6.1. Introduction 83
6.2. Experimental Section 85
 6.2.1. Cell Culture 85
 6.2.2. Single Cell Measurements 85
6.3. Results and Discussion 86
 6.3.1. Characterization of a Bipolar Carbon Fiber Electrode 86
 6.3.2. Comparison of Different Backfill solutions 88
 6.3.3. Voltage Effects on Detection 93
 6.3.4. Electrode Stability 95
6.4. Conclusions 96
6.5. Tables and Figures 98

CHAPTER 7 RESISTIVE-PULSE ANALYSIS OF SINGLE PHOSPHOLIPID VESICLES USING QUARTZ NANOCHANNELS 108

7.1. Introduction 108
7.2. Experimental Section 110
 7.2.1. Preparation of Phospholipid Vesicles 110
 7.2.2. Resistive-Pulse Sensing of Single Nanoparticles and Vesicles 110
7.3. Results and Discussion 111
 7.3.1. Characterization of Cylindrical Quartz Nanochannels 111
 7.3.2. Resistive-Pulse Sensing of Polystyrene Nanoparticles 112
 7.3.3. Resistive-Pulse Sensing of Vesicles 114

7.3.4. Simultaneous Analysis of Nanoparticles and Vesicles	116
7.4. Conclusions	117
7.5. Tables and Figures	119
Bibliography	126

List of Figures

Figure 1-1 Steady-State response of microelectrodes	10
Figure 2-1 Schematic of Pt nanoelectrode fabrication	15
Figure 2-2 TEM images of a Pt nanowire and Pt nanoelectrode	16
Figure 2-3 SEM image of a Pt microdisk electrode	17
Figure 2-4 SEM image of a carbon fiber microelectrode	18
Figure 2-5 SEM image of a silica nanochannel	19
Figure 3-1 Schematic of a Au SNPE	33
Figure 3-2 TEM images of Au nanoparticles	34
Figure 3-3 Modification scheme for the fabrication of a SNPE	35
Figure 3-4 TEM image of a Au SNPE	36
Figure 3-5 UPD of Cu on a 24-nm Au SNPE	37
Figure 3-6 <i>i</i> - <i>V</i> response of 24-nm Au SNPE in 0.5 M H ₂ SO ₄	38
Figure 3-7 Voltammetric characterization of a 25- μ m Pt UME modified with Au nanoparticles	39
Figure 3-8 Voltammetric characterization of Au SNPEs in potassium ferricyanide	40
Figure 3-9 Voltammetric characterization of Au SNPEs in hexamineruthenium (III) chloride	41
Figure 3-10 <i>i</i> - <i>V</i> response of Au SNPEs in 0.10 M KOH (ORR)	42
Figure 4-1 <i>i</i> - <i>V</i> response of a 40 nm disk nanoelectrode in 0.5 M H ₂ SO ₄	54
Figure 4-2 Comsol simulation domain for the recessed disk nanoelectrode	55
Figure 4-3 Simulated steady-state behavior of a recessed disk nanoelectrode	56
Figure 4-4 <i>i</i> - <i>V</i> responses of a 2.7 nm and 150 nm disk nanoelectrodes before and after cycling	57
Figure 4-5 <i>i</i> - <i>V</i> response of a 1.2 μ m disk micro electrode before and after cycling	58
Figure 4-6 SEM image and <i>i</i> - <i>V</i> response of a recessed disk nanoelectrode	59
Figure 4-7 Effect of changing the positive potential limit on potential cycling	60
Figure 4-8 Plot of charge difference vs. electrode radius	61
Figure 5-1 Schematic of a closed bipolar cell and two electrochemical cells connected in a series	77
Figure 5-2 Theoretical <i>i</i> - <i>V</i> response and log plot for a closed BPE	78
Figure 5-3 Experimental <i>i</i> - <i>V</i> response and log plot for a closed BPE	79

Figure 5-4 <i>i-V</i> response for Fc oxidation at a Pt disk coupled to ferricyanide reduction at a Pt wire electrode.....	80
Figure 5-5 <i>i-V</i> response for Fc oxidation at a Pt disk coupled to various reduction reactions at a Pt wire electrode.....	81
Figure 5-6 <i>i-V</i> responses for Fc and DA oxidation at a CFE coupled to various reduction reactions at a cylindrical CFE	82
Figure 6-1 Schematic of a bipolar CFE and <i>i-V</i> response obtained from Fc oxidation at various bipolar CFE configurations.....	101
Figure 6-2 Representative amperometric traces obtained from DA released by exocytosis at single PC12 cells	102
Figure 6-3 Peak parameters and frequency histogram obtained from pooled cell data from amperometric detection of released DA from PC12 cells at +750 mV.....	103
Figure 6-4 Representative amperometric peaks obtained from DA injection at a bipolar CFE	104
Figure 6-5 Voltage dependence on amperometric detection of DA.....	105
Figure 6-6 <i>i-V</i> response from a bipolar CFE and frequency histograms from amperometric detection of released DA from PC12 cells at +200 mV	106
Figure 6-7 Potential cycling of DA at various bipolar CFE configurations	107
Figure 7-1 Schematic of particle detection and Lucite pressure cell	120
Figure 7-2 <i>i-V</i> response of a 640 nm nanochannel and corresponding SEM image.....	121
Figure 7-3 Amperometric detection of polystyrene spheres and size frequency histogram.....	122
Figure 7-4 Amperometric detection of vesicles and size frequency histograms.....	123
Figure 7-5 Frequency histogram from amperometric detection of multiple polystyrene populations	124
Figure 7-6 Concurrent amperometric detection of vesicles and polystyrene spheres.....	125

List of Tables

Table 3-1 Steady-state limiting currents from Au SNPEs	31
Table 3-2 Electrocatalytic activity of Au SNPEs towards ORR.....	32
Table 4-1 Pt dissolution rate for various sized nanoelectrodes	53
Table 5-1 Wave parameters obtained for theoretical and experimental <i>i</i> - <i>V</i> curves.....	74
Table 5-2 Wave parameters for Fc oxidation at a Pt BPE	75
Table 5-3 Wave parameters for Fc and DA oxidation at a CFE	76
Table 6-1 Average kinetic parameters from pooled cell data for DA detection released from single PC12 cells detected at +750 mV.....	98
Table 6-2 Average peak parameters obtained from DA injection at various bipolar CFEs	99
Table 6-3 Average kinetic parameters from pooled cell data for DA detection released from single PC12 cells detected at +200 mV.....	100
Table 7-1 Measurement of polystyrene particle diameters by different methods	119

Glossary

BPE – Bipolar Electrode

CFE – Carbon fiber microelectrode

CV – Cyclic voltammetry

DA – Dopamine

$E_{1/2}$ – Half-wave Potential

Fc – Ferrocene

FSCV – Fast Scan Cyclic Voltammetry

i_{ss} – Diffusion-limited steady-state current

ORR – Oxygen reduction reaction

SEM – Scanning electron microscopy

SNPE – Single nanoparticle electrode

TEM – Transmission electron microscopy

UME – ultramicroelectrode

UPD – underpotential deposition

Acknowledgement

There are numerous people I would like to thank for their support and guidance during my time at the University of Washington. First my advisor Dr. Bo Zhang for allowing me to work in his lab and for the research freedom and support he gave me. I wish to thank past and current members of the Zhang group for their help and encouragement. I would also like to thank Professors Edward M. Eyring and Joel M. Harris at the University of Utah. They have been great mentors to me and without their “gentle persuasion” I would have ended up as lawyer.

Secondly I need to thank all of my friends and family who supported me throughout this marathon. Karen for bringing me the sports page of the Seattle Times every morning, Kevin Garnett for reminding me that “anything is possible”, and all of my friends at the Seattle Institute of Religion for being my family away from home, most notably Todd Knowles and Debi Williams.

Lastly, I would like to thank my wife, Elisha, for her constant encouragement and for standing by me when science wasn’t working as I would have hoped. She helped me see the light at the end of the tunnel, and more importantly helped me to sprint towards it rather than wander idly in the darkness.

Dedication

This work is dedicated to my father for going to work every day without complaining in order to provide for us and teaching me the value of hard work, and also to my mother for her selfless example and encouraging me to dream big.

To “baby” Cox, I hope to be able to teach you the same.

CHAPTER 1 INTRODUCTION

1.1. Microvoltammetric Electrodes

The past three decades have seen tremendous growth in electrochemistry applied on the micro and nano scale. As fabrication methods and instrumentation have improved, research interest regarding the application of micro and nanoelectrodes in fundamental electrochemistry, electrochemical analysis, electrocatalysis, and many other research areas has increased. Nanoelectrodes typically refer to voltammetric electrodes with at least one dimension below 100 nm. They can be viewed as a special type of ultramicroelectrode (UME) with smaller critical dimensions. Most of the outstanding properties of UMEs, such as small RC time constant and fast mass-transport, have been demonstrated on nanoelectrodes and are in many cases more pronounced. More than two decades ago, Wightman predicted in one of his early papers on UMEs some of the advantages to employ sub-micrometer electrodes.¹ Penner et al. also stated that nanoelectrodes would find applications in various areas such as neurophysiology, lithography and chemical analysis.² In the years since those important publications, electroanalytical methods have allowed some of those early predictions to come to fruition and substantial research progress has come to pass.

The application of nanoelectrodes was initiated from the development of nanoband electrodes with band width as small as 5 nm.³ Penner et al. introduced glass-coated hemispherical nanoelectrodes approaching true molecular dimensions (~ 1 nm).² This afforded one many advantages because the geometric dimensions of the electrodes were smaller than the diffusion lengths normally encountered. The mass-transport rate increases as the electrode size decreases and radial diffusion becomes dominant.⁴ This allows steady-state voltammetric responses to be readily achieved.^{1,5} Other advantages include even smaller RC constants and the ability to make measurements in solutions of high resistance because of a lower influence of solution resistance.⁶

In this introductory section, we begin our discussion of electrochemistry on the micro and nanoscale with the analytical methods typically utilized to characterize UMEs. We will then review recent advances in the fabrication of nanoelectrodes highlighting some of the new methods reported in literature. We will also discuss the challenges in the fabrication of structurally well-defined nanoelectrodes.

Furthermore, the application of UMEs to study exocytosis of single cells will be presented as a large portion of the work presented in this dissertation deals with this particular application.

1.2. Methods of Electrode Characterization

It is vital to fully characterize the size and shape of an electrode because its electrochemical properties are often exceedingly sensitive to even small variations in its geometry. For example, the steady-state limiting current of a recessed nanoelectrode is smaller than a disk nanoelectrode of same size due to additional mass-transport resistance. Nanoelectrodes are typically characterized using electron microscopy including scanning electron microscopy (SEM) and transmission electron microscopy (TEM), as well as various electrochemical methods. Unfortunately, it is often very difficult to fully characterize a nanoelectrode with sufficient spatial resolution with electron microscopy mainly due to charging effects from the insulation materials. Electrochemical methods can provide a quick estimate of the size of a nanoelectrode based on the assumption of known geometry. However, such results require microscopic verification.

1.2.1. Steady-State Voltammetry

Under conventional experimental conditions, the voltammetric response of nano and micro electrodes can be characterized by a sigmoidal-shape steady-state voltammogram. Transient voltammetric responses can be obtained with sufficiently high sweep rates. For example, a 50-nm-radius nanoelectrode will require the sweep rate to be at least 1000 V/s in order to show peak-shaped transient voltammetric behavior. Under this condition the diffusion layer thickness can be estimated to be $\sim 1 \mu\text{m}$ for a redox species with a diffusion coefficient $\sim 10^{-5} \text{ cm}^2/\text{s}$.

Figure 1-1a shows a steady-state cyclic voltammogram (CV) of an 86-nm-radius Pt nanoelectrode placed in acetonitrile containing 5-mM ferrocene and 0.2 M tetra-n-butylammonium hexafluorophosphate (TBAPF₆). The oxidation of ferrocene at the surface of a nanoelectrode in solutions of high concentrations of supporting electrolyte is diffusion controlled and the steady-state limiting current, i_{ss} , is easily observed. The magnitude of i_{ss} is dependent on the size and shape of the electrode. The general equation for i_{ss} is governed by the total mass transfer resistance of the redox species from the bulk solution to the electrode and shown by the following equation,⁴

$$i_{ss} = \frac{nFC^*}{R_{MT}} \quad (1-1)$$

where n is the number of electrons transferred, F is Faraday's constant, C^* is the bulk concentration of redox species in solution and R_{MT} is the mass-transfer resistance. The electrodes fabricated in our lab and used for the experimentation in this dissertation have disk shaped geometry. For a disk-shape UME as the one used in Figure 1-1a, the steady-state limiting current can be represented using the following equation,

$$i_{ss} = 4nFD C^* a \quad (1-2)$$

where a is the radius of the disk nanoelectrode, and D is the diffusion coefficient. The mass-transfer resistance will vary for different electrode shapes and is shown in Figure 1-1b. The apparent radius for a disk-shape and hemispherical electrode is represented by a . For a nanoband electrode, l and r represent the band length and radius, respectively. The radius of the band is a geometric feature derived from the band width divided by π , this is because band geometry has the same radial diffusion field as a hemicylindrical surface.³ The time component, t , is equal to RT/Fv ,⁷ where R is the gas constant, T the temperature, and v the scan rate. Although the equation exhibits slight time dependence, at long times the current-time relationship approaches a steady-state limiting current.

There are several advantages which make steady-state cyclic voltammetry extremely useful for studies involving the use of UMEs. Steady-state CV can be utilized to quickly evaluate the size of the electrode from the diffusion-limited steady-state current based on the assumption of known shape, e.g., hemispherical electrode. Conversely the limiting current can also be easily used to analyze the concentration of redox species using nanoelectrodes of known size and shape. The shape of the voltammogram can be analyzed to provide useful information to evaluate kinetics of heterogeneous electron transfer at the electrode surfaces.^{8,9} Using electrodes of specially designed geometry, e.g., nanopore electrodes, steady-state voltammetry can be utilized to study transport of redox species in nanoscale spaces.¹⁰

1.2.2.Characterization by Electron Microscopy

Electron microscopy can be especially helpful to obtain quick and direct information about the shape and size of an electrode. The resulting information, however, is often limited by the spatial resolution of the instrumentation, the skill of the operator, and the sample properties of the electrodes. SEM can reveal very useful three dimensional information about the electrode geometry. However, it only has limited spatial resolution with conventional tungsten-filament SEM. Field-emission SEM can provide enhanced spatial resolution on the order of 1-2 nm under optimized conditions, e.g., using very conductive samples. Higher spatial resolution can be obtained by imaging nanoelectrodes with TEM. However, only certain nanoelectrodes with submicron overall dimensions can be imaged by TEM. The high-energy electrons used in TEM can penetrate the thin silica insulating material and the sub-10 nm Pt nanowire can be clearly resolved from the silica coating because of the z-contrast between the Pt and its environment.

1.2.3.Scanning Electrochemical Microscopy

Although an apparent size of an electrode can be readily extracted from steady-state CV, little or no information can be obtained about the shape of the electrode. SECM was first used to characterize nanoelectrode tips by Bard's group.⁸ In this method an approach curve is generated as a nanoelectrode is lowered towards an insulating or conductive substrate in a solution containing an electroactive species. A potential is applied at the tip to induce the desired electrochemical reaction and the current is monitored as a function of the distance from the substrate as the probe gradually approaches it. When the tip is far from the substrate the measured current is the same as i_{ss} and the radius of the electrode can be calculated from equation 1. As the tip approaches the substrate the observed current change is dependent on the distance to the substrate and its conductivity. In order to obtain a useful approach curve the tip must be moved to within one or two tip radii from the substrate. This is challenging for small nanoelectrodes, e.g., < 20 nm, with a short useful approach curve distance range.¹¹ The shape of the approach curve is governed by the mass transport at the tip and by comparing the shape of experimental approach curves to theory, the geometry of the electrode can be ascertained.^{12,13}

1.2.4. Surface Adsorption and Charging

One of the challenges that arise in research with electrodes on the micro and nano scales is the correlation between the apparent electrode size and the actual microscopic area. Recent studies have employed the usage of the underpotential deposition (UPD) at metal electrodes to obtain the actual electrochemically active surface area.^{14,15} This is usually done by electrochemically depositing a single layer of Cu atoms on the surface of the electrode by applying a potential slightly more positive than the Nernst potential for Cu.¹⁶ The Cu is then stripped from the surface by sweeping the potential producing a current peak. The amount of charge for the oxidation of Cu is used to obtain the actual microscopic area.¹⁷

Another method that has been used to estimate the microscopic surface area was demonstrated by White and co-workers.¹⁸ This method measures the electrical charge associated with the oxidation of an adsorbed complex molecule, bis(2,2'-bipyridine)chloro(4,4'-trimethylenedipyridine)osmium(II), by fast-scan cyclic voltammetry. This method has been successfully used to measure Pt nanoelectrodes as small as 70-nm in radius. After the complex is adsorbed on the electrode surface fast-scan cyclic voltammetry is especially needed in the case of nanoelectrodes because of the small number of redox molecules involved in the analysis. This method is advantageous because it is not always practical to obtain SEM or TEM images of every electrode employed in laboratory use.

1.3. Development of Electrode Fabrication Techniques

Numerous methods have been previously employed to produce small electrodes of various shapes and materials. Representative methods include micropipette pulling technology,^{12,19} partial insulation of an electrochemically-sharpened metal wire or carbon fiber in photoresist,²⁰ Teflon,²¹ electrophoretic paint,^{18,22-24} and glass.^{2,25} For a detailed summary about different materials and methods previously employed in electrode fabrication, please refer to Arrigan²⁶ and Zoski²⁷. Despite the enormous progress, the controllable fabrication of structurally well-defined nanoelectrodes and their characterization at high spatial resolution remain challenging for their successful application. Recent progress in UME fabrication has produced electrodes with the following shapes: band, disk, hemispherical, and pore-shaped as well as electrode arrays and ensembles. The micro and nanoelectrodes used for

experimentation in this dissertation were all fabricated with disk geometry and as such only this geometry will be highlighted.

1.3.1. Disk Nanoelectrode Fabrication

Substantial progress has been made in the past decade in the fabrication of disk nanoelectrodes. Many reported disk nanoelectrodes consist of glass-encapsulated metal nanoelectrodes, where a metal wire is sealed in an insulating sheath and a disk shaped cross section results from exposing the end of the wire. The geometric area of a nanodisk electrode scales with the square of the radius, which can be made as small as a few nm². Electrodes of such dimensions can be advantageous when one wants to examine faradaic reactions over a small area or probe single redox molecules or nanoparticles. However this can result in a measured current that is quite small and detection of such small currents may be limited in some cases by instrumentation.

Nanodisk electrodes evolved from sharp tip electrodes that were primarily employed for SECM⁸ and neuroscience applications.²⁸ These existing methodologies were refined and resulted in the fabrication of needle-type Pt-disk electrodes via a laser-assisted pulling process first demonstrated by Shao and Mirkin¹² and then further improved by Schumann and co-workers.²⁹ This procedure has been modified in our lab to fabricate Pt disk electrodes in the size range of 1-3 nm.³⁰ In this method a wire is sealed in a glass capillary and is pulled into a sharp tip. This procedure is described in more detail in chapter 2.

An alternative method to pulling would be to seal and expose sharp metal tips prepared by electrochemical etching.²⁵ In this method a Pt/Au microwire is electrochemically etched to a sharp tip in a NaCN/NaOH solution. The sharpened tip is sealed into a piece of glass capillary and exposed to form a nanodisk by mechanical polishing. In both methods a major factor that affects the diameter of the disk is the amount of polishing.

Although Pt nanoelectrodes are regularly fabricated by the pulling method, difficulties arise when it is desired to use a different metal. Because the melting point of quartz glass, ~1670 °C, is close to but below the melting point of Pt metal, ~1770 °C, Pt wires can be readily pulled via the previously mentioned method. In the case of Au where the melting point is substantially lower, ~1060 °C, it is more difficult to

fabricate Au nanoelectrodes. As a result it can be challenging to prepare Au nanoelectrodes with laser pulling. Mirkin and co-workers have demonstrated the fabrication of Au disk nanoelectrodes with radii down to roughly 40 nm by using borosilicate glass.³¹

Another method to fabricate Au disk nanoelectrodes of small dimensions involves the electrochemical deposition of Au in Pt nanopore electrodes.³² This is accomplished by first fabricating a Pt disk nanoelectrode of desired dimension and electrochemically etching the Pt to form a nanopore electrode.³³ In the next step Au is electrochemically reduced inside the nanopore to form a Au nanowire. The excess Au is then polished away. As expected, the diameter of the Au nanoelectrode is dependent upon the initial diameter of the Pt nanodisk electrode. By this method Au nanoelectrodes as small as 4.5 nm in radii have been obtained.

In spite of the recent progress, there are still challenges that exist in current fabrication methods for disk nanoelectrodes. Most notably would be the agreement of geometric and effective electrochemical dimensions. Sun and coworkers have recently conducted a series of nice experiments showing the correlation of the radius as determined by CV and SEM.³⁴ They have concluded that the geometric radius matches the effective radius closely when the electrode is greater than 20 nm. However when the effective radius is under that limit the observed current fluctuates from probable potential fluctuations and double layer effects. It has also been shown from a theoretical perspective that the voltammetric behavior of nanoelectrodes will differ from conventional voltammetric theory when the radius is below 10 nm.^{4,35-37} One of the factors attributing to this phenomenon is that the current density on a disk is non-uniform and greater at the edge of the electrode. Another challenge that exists in preparing nanoelectrodes of this manner is leakage¹⁴ and current fluctuation caused by mismatch in expansion coefficient and from mechanical polishing. After mechanically polishing the electrode tips, it can be difficult to know exactly whether the exposed tip is planar or non-planar. For this reason it is important to use SECM or other analytical methods to confirm the electrode geometry.

1.4. Electrochemical Approaches to Investigate Exocytosis

One area that has seen tremendous growth and advancement in microscale electrochemistry is in electroanalytical studies of neurochemistry. Neuronal communication is facilitated by exocytosis – a

process by which a secretory cell such as a neuron releases hormones or neurotransmitters. The ability to acquire chemical knowledge of neurotransmission has many biological and medical implications and as our ability to understand the chemical composition and dynamics of neurotransmission increases as does our ability to treat neurological disorders such as Parkinson's disease.^{38,39} Previous methods used to quantitatively study exocytosis traditionally centered on patch clamp measurements, however the development of microscale electrochemistry has enabled the ability to directly measure neurotransmitter release and eavesdrop on single cell communication.⁴⁰ A large fraction of neurotransmitters are electrochemically active and can be directly detected using electrochemistry. Carbon fiber microelectrodes (CFE) have come forth as the ideal tool to study exocytosis at single cells.⁴¹ Carbon as an electrode material has many advantages such as biocompatibility, large potential region and high tensile strength. Additionally the fabrication of CFEs ranging from 5 μm to 20 μm is straightforward and inexpensive.⁴² Because of the small surface area of CFEs diffusion-limited voltammetric studies can be conducted at high scan rates with very fast temporal and high spatial resolutions.⁴³ The most widely used methods which employ microelectrodes to study neurochemical dynamics are constant potential amperometry and fast scan cyclic voltammetry.

1.4.1. Constant Potential Amperometry

In constant potential amperometry a carbon fiber microelectrode is placed directly next to a cell with the potential at the electrode held at a sufficient potential to reduce or oxidize the chemical messenger of interest such that the mass transfer is diffusion limited. The current at the electrode tip is measured as a function of time. The cell is stimulated to release its contents and molecules are detected as current peaks that represent the quantal amount of chemical present in synaptic vesicles.^{40,44,45} Amperometry has been used to study exocytosis in immortalized cell lines^{44,46}, brain slices⁴⁷, intact neurons⁴⁸⁻⁵⁰, and primary cell cultures.⁵¹ Because the electron transfer occurs at a faster time scale than the release and reaction is diffusion limited, constant potential amperometry has sub millisecond temporal resolution and these studies can be used to observe the dynamics of individual exocytotic events. Analysis of the current time trace and the features of the amperometric peaks allows one to quantitatively characterize vesicular release and study the kinetics of fusion pore release.⁵²

1.4.2. Fast Scan Cyclic Voltammetry

Although amperometry provides insight into fusion pore dynamics, it lacks in the ability to chemically distinguish between different chemicals. By employing fast scan cyclic voltammetry one can chemically resolve individual secreted species based upon their voltammetric signature.⁵³ This method allows for time resolved chemical changes in the local environment near the cell. In fast scan cyclic voltammetry, individual voltammograms are recorded by repeatedly applying a triangular wave form through a range of potentials at high scan rates e. g. 400 V/s.⁵⁴ By repeatedly scanning the electrode, successive cyclic voltammograms will be recorded as any electroactive species near the electrode will be oxidized/reduced and identified on the basis of its individual electrochemical behavior.⁴⁰ Because of the high scan rates a large capacitance current arises. Voltammograms are obtained before and after stimulation, and the background current is subtracted allowing the i - V characteristics of the redox species to be readily observed.⁵⁵ The temporal resolution is limited by scan rate which limits its applications into kinetic studies. However fast scan cyclic voltammetry is an effective complementary tool to amperometry and most commonly used as a qualitative tool to identify secreted chemicals.

1.5. Figures and Tables

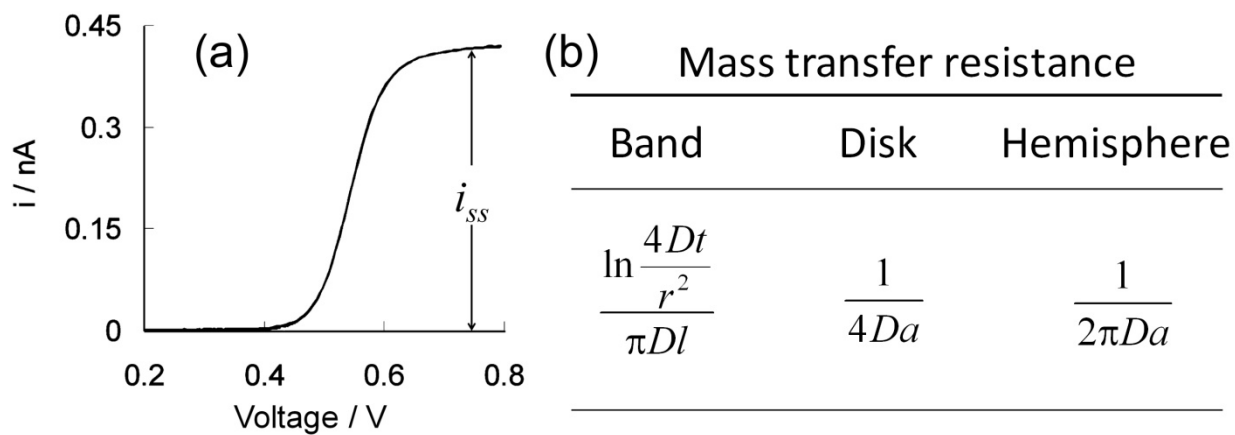


Figure 1-1. (a) The steady-state voltammetric response of a 86-nm-radius Pt disk nanoelectrode. The radius of the electrode, a , is calculated from the magnitude of i_{ss} and the mass-transfer resistance for a disk electrode geometry, (b) the equations for calculating the mass-transfer resistance of three different electrode shapes.

CHAPTER 2 INSTRUMENTATION AND FABRICATION

2.1. Reagents and Materials

The work carried out in this dissertation used the following redox molecules: ferrocene (Fc, Fluka), dopamine hydrochloride (DA, Sigma-Aldrich), hexaamineruthenium (III) chloride ($\text{Ru}(\text{NH}_3)_6\text{Cl}_3$, Aldrich), potassium ferricyanide ($\text{K}_3\text{Fe}(\text{CN})_6$, Acros Organics), and potassium ferrocyanide ($\text{K}_4\text{Fe}(\text{CN})_6$, Fluka). Supporting electrolytes: tetra-n-butylammonium hexafluorophosphate (TBAPF_6 , Aldrich), and potassium chloride (KCl, Mallinckrodt Baker). Perchloric acid (HClO_4 , Aldrich), and sulfuric acid (H_2SO_4 , Fisher) were also used in electrolyte solutions. All aqueous solutions were prepared using $\geq 18 \text{ M}\Omega\text{-cm}$ water from a Barnstead NanoPure purification system (Thermo Scientific), and organic solutions in reagent grade acetonitrile (MeCN, Mallinckrodt Baker). Oxygen reduction reactions were carried out in a 0.1 M KOH (Mallinckrodt) solution which had been bubbled with O_2 for a minimum of 20 minutes. Electrode surface modifications were done with 3-aminopropyltrimethoxysilane (APTMS, $(\text{CH}_3\text{O})_3\text{Si}(\text{CH}_2)_3\text{NH}_2$, Gelest Inc.), and 3-cyanopropyltrimethoxysilane ($\text{Cl}(\text{Me})_2\text{Si}(\text{CH}_2)_3\text{CN}$, Fluka), Dopamine hydrochloride (DA, Sigma-Aldrich).

Single cell experiments were carried out in an isotonic saline solution consisting of 150 mM NaCl, 5 mM KCl, 1.2 mM MgCl_2 , 5 mM glucose, 10 mM HEPES, and 2 mM CaCl_2 with the pH adjusted to 7.4 with 3 M NaOH. High potassium stimulant consisted of the same components with the exception of 100 mM KCl and 50 mM KCl.

For nanopore sensing experiments vesicles were prepared from 1- α -phosphatidylcholine (PC), and 1,2-dioleoyl-sn-glycero-3-phosphocholine (DOPC) (Avanti Polar Lipids). Buffer solutions were prepared with triton X-100 (Sigma-Aldrich), and 10x PBS OmniPur liquid concentrate (EMD Chemicals). 175 nm and 356 nm polystyrene microspheres were purchased from Polysciences Inc. A mini-extruder apparatus was obtained from Avanti Polar Lipids, Inc. Polycarbonate membranes for the extruder of 100 nm and 200 nm were purchased from Whatman.

2.2. Fabrication Methods

2.2.1. Fabrication of Pt Nanoelectrodes

Pt nanoelectrodes are fabricated using a laser assisted pulling process previously reported by Mirkin¹² and Schumann²⁹ and further developed by our lab to make nanodisk electrodes as small as 1-3 nm in diameter.³⁰ A schematic outlining the general fabrication process is shown in Figure 2-1. A Pt microwire (99.95%, hard, Alfa Aesar) preform is sealed inside a quartz glass capillary (o.d. = 1.2 mm, i.d. = 0.40 mm) and pulled into a sharp tip with a laser puller (Model P-2000, Sutter Instrument Co.). Before the tip is pulled it is essential that there is a good seal between the Pt wire and the glass such that the pulling process yields a continuous Pt wire. The diameter of the wire at the end of these tips can be well-controlled in a range of ~2 to 10 nm. The end of the Pt wire is enclosed in a sheath of glass and exposed by mechanical polishing.^{13,56} Because of the conical geometry of the pulled Pt nanowire it is crucial to only expose the metal directly at the end of the electrode in order to obtain the minimal size possible and due to the extremely small size of the tip it is very difficult to polish the tip in such a manner so that the wire remains continuous and does not break. As an alternative to beveling to expose the wire, the entire sharp tip is sealed in a borosilicate glass capillary with a hydrogen flame before exposing the wire. After Electrical contact is made with the unsealed portion of the wire inside the capillary by connecting it to a 150 μm tungsten wire with conductive silver paste (Dupont), the Pt tip is exposed by polishing with fine grit sand paper. The polishing process is the crucial step in determining the final size of the electrode and as such needs to be closely monitored using an optical microscope and an ultrasensitive continuity tester to ensure that polishing stops at the point when the Pt tip is exposed. After the tip is exposed the electrode is characterized by CV. A TEM image of a 1.5 nm radius Pt nanowire is shown in Figure 2-2a and a 3 nm radius Pt nanoelectrode in Figure 2-2b.

2.2.2. Fabrication of Pt and Au Microelectrodes

Metal microelectrodes were fabricated by encapsulating wire in a glass capillary. Pt and Au micro wires with a diameter of 25 μm (99.95%, hard Alfa Aesar) were partially sealed in a borosilicate capillary (o.d. = 2.0 mm, i.d. = 1.0 mm) using a vacuum and hydrogen flame. Electrical contact was made by connecting the unsealed portion of the wire to a 150 μm tungsten wire with conductive silver paste. The

sealed portion of the wire was exposed with regular sandpaper and an alumina suspension on a wet polishing cloth. An SEM image of a 12.5 μm Pt micro electrode is shown in Figure 2-3.

2.2.3. Fabrication of Carbon Fiber Microelectrodes

Carbon fiber microelectrodes (CFE) were fabricated according to our published methods.⁵⁷ A 5 μm or 7 μm carbon fiber was aspirated into a borosilicate glass capillary (o.d. = 1.2 mm, i.d. = 0.69 mm) and pulled with a micropipette puller (Model P-97, Sutter Instrument Co.). In order to obtain disk shaped electrode geometry, the end of the pulled tip was cut with a scalpel at the glass/carbon fiber interface and then sealed with epoxy (Epoxy Technology) and allowed to cure for 24h at roughly 80° C. After the epoxy was cured the tip was beveled (Model BV-10, Sutter Instrument Co) to 45°. For cylindrical geometry the exterior carbon fiber was trimmed with a scalpel to the desired length. Electrical contact was obtained by either directly connecting a tungsten wire to the interior carbon fiber with conductive silver paste or by backfilling the electrode with a solution. The contents of the backfill contained either colloidal graphite in water (Energy Beam Sciences) or an electrolyte solution such as potassium chloride, potassium ferricyanide, or hexamineruthenium (III) chloride. An SEM image of a CFE is shown in Figure 2-4.

2.2.4. Fabrication of Silica Nanochannels

The preparation of a quartz nanochannel is a multistep process which includes the fabrication of a quartz nanochannel preform and a borosilicate glass micropipette holder which has been reported by our group.⁵⁸ An ultrasharp quartz tip is drawn by using a laser micropipette puller (P-2000; Sutter Instrument Company) as a nanochannel preform. In this process a ~2 cm length of silica microcapillary (o.d. = 350 μm , i.d. = 20 μm) tubing is placed inside a 7.5-cm length quartz capillary tube (o.d. = 1 mm, i.d. = 0.3 mm) and sealed in place by heating and cooling cycles with the inner capillary under vacuum. This was repeated until the size of the microchannel was reduced to 5 μm or less. After that the vacuum was removed and a pulling program was executed to pull the capillary into two ultrasharp quartz tips.

Glass micropipette holders were made from 7.5 cm lengths of borosilicate tubing (o.d. = 2.0 mm, i.d. = 1.16 mm) which were pulled by a P-97 micropipette puller (Sutter Instrument Company) to produce blunt micropipettes with a wide opening. A quartz nanotip was carefully inserted into the glass holder

under an optical microscope until length of about 100 to 200 μm extended through the end of the channel holder. The tip was sealed in place by quickly moving it through a natural gas flame fusing only a short portion of the tip to the borosilicate micropipette. The unsealed portion of the tip is pulled out of the holder leaving only the sealed portion in place and the tip of the micropipette was cut off on an inverted microscope. An SEM image of a 640 nm silica nanochannel is shown in Figure 2-5.

2.3. Cyclic Voltammetry

Cyclic Voltammetry (CV) is a common technique which is employed in the experiments throughout this dissertation to measure the current-voltage response in order to characterize electrodes and nanochannels. All current-voltage responses were measured using a Chem-Clamp voltmeter/ampereometer (Dagan) and a PAR 175 (Princeton Applied Research) universal function generator. The potentiostat was interfaced to a Dell computer through a PCI-6251 data acquisition board (National Instruments) via a BNC-2090 analog breakout box (National Instruments). The current-voltage data was recorded and analyzed using an in-house written virtual instrumentation with LabView 8.5 (National Instruments). Two types of electrochemical cells were used, a conventional two-electrode set up and a bipolar cell configuration. A two-electrode one compartment electrochemical cell consisted of a one working electrode and a Ag/AgCl reference electrode (Bioanalytical Sciences Inc) with the preamplifier in a home built Faraday cage. For studies using bipolar electrochemical cells, the cell was constructed by connecting two cells in series with two working microelectrodes connected and two Ag/AgCl electrodes used to supply the driving voltage bias across the bipolar cell. This arrangement will be discussed in more detail in chapter 5.

2.4. Tables and Figures

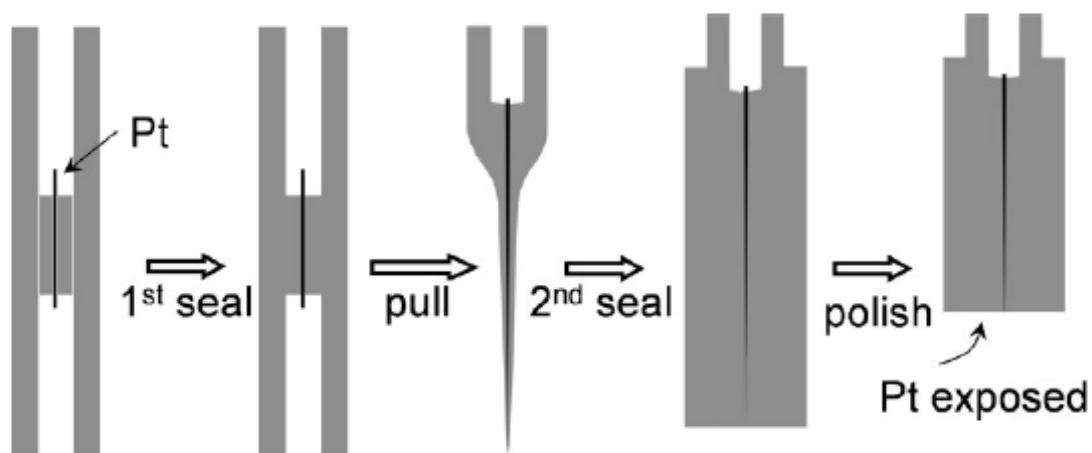


Figure 2-1. Schematic showing the modified laser-assisted pulling process for the preparation of Pt nanoelectrodes. Reprinted with permission (Anal. Chem. 2009, 81 (13), 5496-5502). Copyright American Chemical Society 2009.

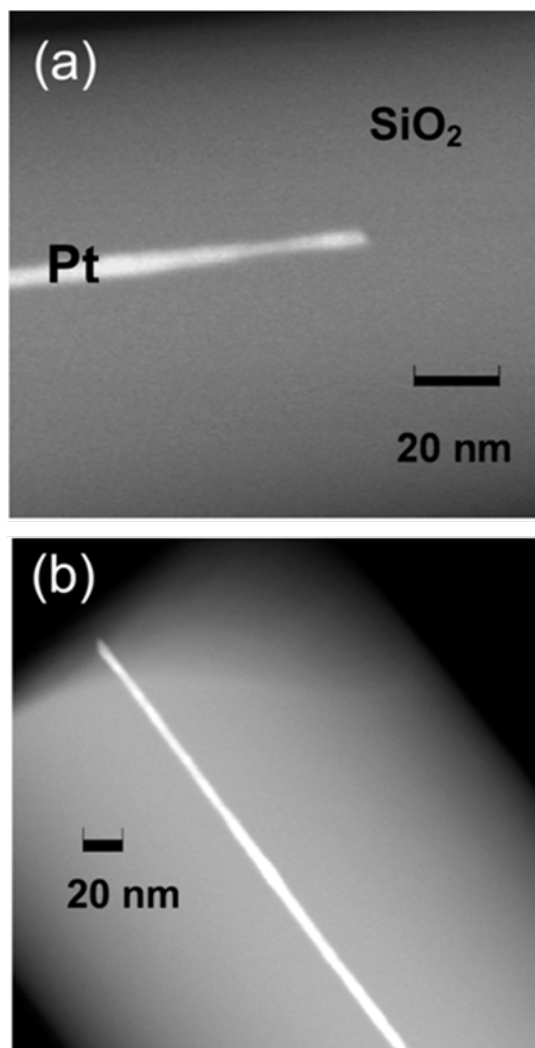


Figure 2-2. TEM image of a 1.5 nm radius Pt nanowire (a) and a 3 nm radius Pt nanoelectrode sealed in glass (b). Reprinted with permission (Anal. Chem. 2009, 81 (13), 5496-5502). Copyright American Chemical Society 2009.

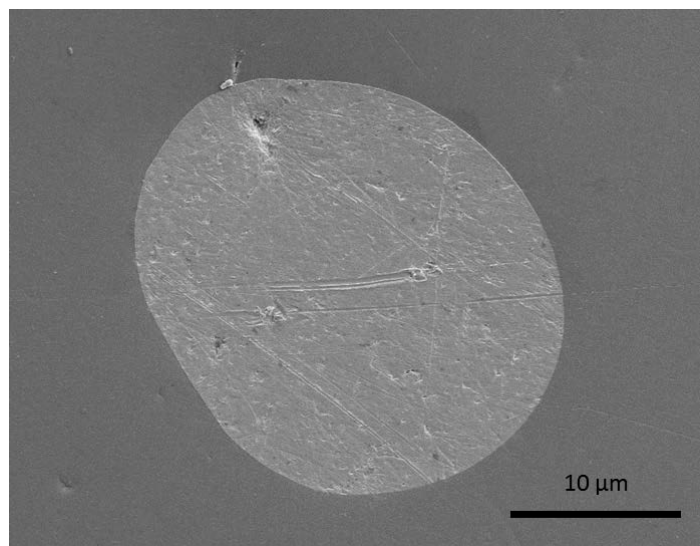


Figure 2-3. SEM image of a 12.5 μm Pt disk electrode sealed in glass.

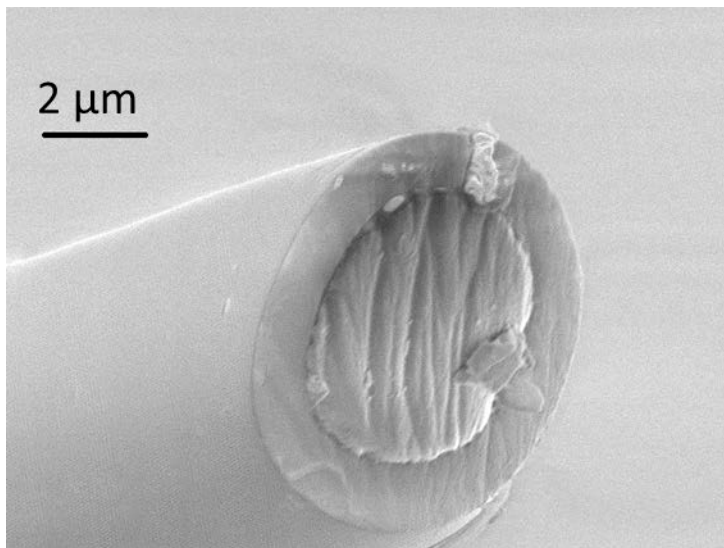


Figure 2-4. SEM image of a 5 μm carbon fiber microelectrode.

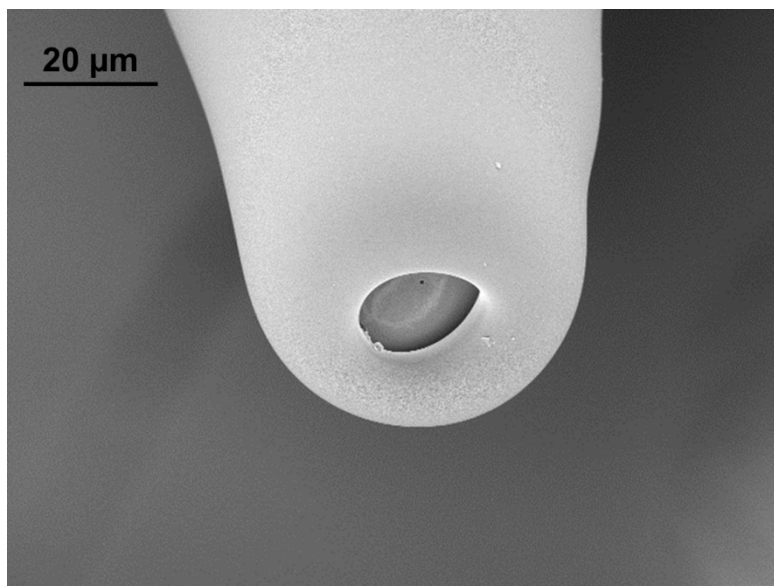


Figure 2-5. SEM image of a 640 nm Nanochannel.

CHAPTER 3 ELECTROCHEMICAL RESPONSES AND ELECTROCATALYSIS AT SINGLE Au NANOPARTICLES*

3.1. Introduction

Nanomaterials have received intensive research interest in recent decades due to their unique structure-dependent properties and potential applications in numerous fundamental and applied fields.^{59,60} For example, nanoparticles have been extensively utilized as catalysts in chemical synthesis,⁶¹ energy conversion,^{62,63} and energy storage.⁶⁴ An important aspect of nanoparticles is their structure-dependent catalytic activity.^{65,66} It has been shown that the electrocatalytic activity of metal nanoparticles is extremely sensitive to their sizes.⁶⁷⁻⁷⁰ Due to differences in electrochemical activity at different crystal surfaces, the shape of the nanoparticles also greatly alters their functionality. For example, the catalytic activity of Pt single crystals toward oxygen-reduction reaction (ORR) in H₂SO₄ at the {110} surface is significantly greater than the {100} and {111} surfaces.⁷¹ There have been numerous research efforts reported to control the shape of metal nanoparticles in order to obtain optimized activity in electrocatalysis.⁷²⁻⁷⁷ The composition of metal nanoparticles also plays critical roles in their catalytic activity.^{78,79}

Most current studies in electrocatalysis rely on the use of ensembles of nanoparticles to understand the structure-function relationship.⁸⁰⁻⁸² However, only averaged catalytic properties can be obtained from such experiments. In a typical study, metal nanoparticles are immobilized on a supporting electrode to form a nanoparticle-array electrode, and then their electrochemical responses are measured as a function of particle structure.^{68,83-86} The properties of metal nanoparticles can be complicated due to a combination of multiple effects, such as inter-particle spacing,⁸⁷ quality of the self-assembled monolayers (SAMs), and the size distribution of particles. There are some excellent examples reported to study the size effects of metal nanoparticles in electrocatalysis using the array method. For example, the Crooks group has shown that the catalytic activity of dendrimer-encapsulated Pt nanoclusters increases with increasing size for ORR.⁸⁸ The Zou group has measured the electrocatalytic activities at bare Au nanoparticles and found

* Adapted with permission from J. Am. Chem. Soc. 2010, 132,3047-3054. Copyright 2010 American Chemical Society. This work was done in collaboration with Dr. Yongxin Li.

that the catalytic activity of Au nanoparticles for the oxidation of CO reaches an optimized value when they are about 4 nm.⁸⁷

Only few attempts have been reported to directly measure the faradaic responses at individual nanoparticles. Bard et al. recently reported an innovative method to measure the diffusion-limited faradaic current at single Pt nanoparticles.⁸⁹⁻⁹¹ In their experiments, an inert ultramicroelectrode (carbon or gold) was held at a potential where there is no apparent electrochemical reaction occurring. However, when a collision between a Pt nanoparticle and the ultramicroelectrode happens, electrochemical reactions can be detected at the Pt surfaces. Chen's group recently reported a method of measuring the electrocatalytic activity at individual metal nanoparticles and single carbon nanotubes by single-molecule fluorescence.⁹² A challenge in utilizing the above methods to correlate the structure-function relationship is the subsequent structural characterization of the same metal nanoparticles with high-resolution electron microscopy. Meanwhile, it could also be difficult to obtain an entire current-voltage response at individual nanoparticles using these methods.

It has become increasingly important to understand the relationship between the functionality of nanoparticles and their structure in order to more fully utilize the unique catalytic properties of nanoparticles. However, it remains practically difficult to attribute the catalytic activity to the structure of nanoparticles. In order to precisely correlate the structure and function of nanoparticle catalysts, both electrochemical responses and high-resolution structural characterizations are needed at a single-nanoparticle level. Nanoelectrodes could provide a particularly useful avenue for this purpose due to their extremely small size. Chen and Kucernak have recently reported the study of ORR at single Pt nanoparticles electrodeposited on carbon nanoelectrodes.⁹³ Their results show that using single Pt nanoparticle in between ~50 nm to 5 μm , the effect of ultrahigh mass-transfer rate on the ORR can be readily studied. Interestingly, they have shown that the ORR pathway can be alternated from the regular direct reduction of oxygen (4-electron pathway) toward indirect reduction (2-electron pathway) when particle size decreases from >5 μm to ~50 nm due to a higher mass transfer rate of H_2O_2 at smaller particles.

Using Pt nanoelectrodes as small as 2 nm in radii,⁹⁴ we have studied the electrochemical responses and electrocatalytic activity at single Au nanoparticles. A Au SNPE has been developed for these studies by immobilizing a single Au nanoparticle at the surface of a nanoelectrode. Figure 3-1 shows a schematic diagram of a SNPE, in which a single Au nanoparticle is immobilized on a Pt nanodisk. In between the Au nanoparticle and the Pt surface are the silane linker molecules. Single Au nanoparticles in the range of 10 to 30 nm in diameter have been chemically assembled at the end of a Pt nanoelectrode, using 3-aminopropyltrimethoxysilane (APTMS) as the linker molecule. These nanoelectrodes have been characterized using TEM, UPD, and steady-state voltammetry. ORR has been examined at single Au nanoparticles using SNPEs. The steady-state voltammetric responses and the electrocatalysis results show that the electron-transfer kinetics at Au SNPEs is rapid, and that the Au SNPEs are excellent nanoprobe for studying electrocatalysis at a single-nanoparticle level. This research not only provides a new electrochemical platform for investigating electrocatalytic nanomaterials, it also suggests a new electroanalytical nanoprobe for many other research areas. For example, SNPEs could be particularly useful in studying electron-transfer kinetics between the nanoelectrode and the metal nanoparticles, therefore providing valuable information for molecular electronics and single-nanoparticle electrochemical sensor.

3.2. Experimental Section

3.2.1. Preparation and Characterization of Gold Nanoparticles

Au nanoparticles in the range of 10 to 30 nm in diameter were prepared by the reduction of HAuCl_4 with sodium citrate.^{95,96} All glassware was thoroughly cleaned with a fresh piranha solution and rinsed thoroughly with water before use. In a typical synthesis of ~14 nm Au nanoparticles, 50 ml of HAuCl_4 solution (0.01%, m/v) was brought to a vigorous boil with stirring in a round-bottom flask fitted with a reflux condenser, and 1.8 ml of (1%, m/v) sodium citrate solution was then rapidly added to the flask. The heating and stirring were continued for 15 min and then the solution was allowed to cool to room temperature with continuous stirring, and stored at 4 °C until use. Larger nanoparticles were prepared by reducing the molar ratio of sodium citrate to HAuCl_4 in the synthesis. The average sizes of the nanoparticles were determined from TEM characterizations as shown in Figure 3-2.

3.2.2. Fabrication of Au Single Nanoparticle Electrodes

The general strategy for the fabrication of Au SNPEs is depicted in Figure 3-3. Starting from a Pt disk nanoelectrode, the silanization of the silica surfaces with $\text{Cl}(\text{Me})_2\text{Si}(\text{CH}_2)_3\text{CN}$ was described by Wang et al.⁹⁷ Following the exposure of the Pt nanodisk, the electrode was rinsed completely in H_2O , EtOH, CH_3CN , and H_2O , and then soaked in a 1.0 M HNO_3 for 10 min. The electrode was rinsed with H_2O and CH_3CN and then immersed overnight in an CH_3CN solution containing ~2% v/v $\text{Cl}(\text{Me})_2\text{Si}(\text{CH}_2)_3\text{CN}$. After that, the electrode was rinsed with CH_3CN and H_2O again.

The modification of the Pt nanodisk with silane was carried out according to previously methods provided by Murray et al.⁹⁸⁻¹⁰⁰ with slight modifications. The Pt nanoelectrode from the previous step was cleaned by rinsing with ethanol and water. A layer of Pt oxide was generated by applying a potential of 1.20 V vs. Ag/AgCl in a 0.5 M H_2SO_4 until the oxidation current decayed to zero, whereupon the electrode was removed from the H_2SO_4 solution while still under potential control (1.20 V), rinsed thoroughly with water, and dried at ca. 50 °C for 30-60 min. The oxidized Pt (PtO) nanoelectrode was placed in an anhydrous toluene solution containing ca. 5% $(\text{CH}_3\text{O})_3\text{Si}(\text{CH}_2)_3\text{NH}_2$ for ~30 min under N_2 protection. The silanized PtO surface was then rinsed thoroughly with toluene, CH_3CN , and water.

In the last step, the silane modified Pt nanoelectrode was immersed into a solution of Au nanoparticles (as-prepared from previous synthesis) overnight at room temperature, and then was rinsed well with water and subjected to electrochemical measurements.

3.2.3. Transmission Electron Microscopy

TEM images of Au nanoparticles, SiO_2 -coated Pt nanoelectrodes and Au SNPEs were acquired on a Tecnai G2 F20 (FEI) microscope. The imaging of the Au nanoparticles was carried out on a carbon film (Ted-Pella). Pt nanoelectrodes and Au SNPEs were mounted on a Cu grid (SPI) using Ag paint (SPI) before TEM imaging. No additional coatings were performed prior to imaging of the nanoelectrodes or SNPEs.

3.3. Results and Discussion

3.3.1. TEM Characterization of Au Single Nanoparticle Electrodes

One of the challenges in correlating the catalytic function to the structural characteristics of nanoparticles is the direct high-resolution imaging of single nanoparticles. TEM is one of most popular methods to provide atomic resolution structural information of nanoparticles.¹⁰¹ The application of ultrasmall Pt nanoelectrodes has made it possible to directly characterize single Au nanoparticles with TEM. Figure 3-4 shows an example of a TEM image of a single Au nanoparticle immobilized on a Pt nanoelectrode. It can be seen from the TEM image that a single Au nanoparticle is attached on the Pt disk. The immobilization is mainly due to the electrostatic interaction between the Au nanoparticle and the amino-terminated surface.^{102,103} The Pt nanodisk has been measured to be ~10 nm, while the Au nanoparticle is ~15 nm in diameter. Some other Au nanoparticles can also be found on the SiO₂ surfaces far away from the Pt disk possibly due to physical adsorption. The ability of directly imaging single nanoparticles chemically attached at a nanoelectrode is important for the correlation of the structure of the nanoparticle with its functionality.

The Pt nanoelectrode used in Figure 3-4 was prepared by polishing the Pt nanotip directly on a polishing surface.¹⁰⁴ Due to bending of the Pt tip upon contacting the polishing surface and/or mechanical vibration, most of the Pt nanoelectrodes show discontinuity in the Pt nanowires. Therefore, we should point out that we had a low success rate (< 5%) in preparing useful ultrasharp Pt nanoelectrodes for TEM imaging. To obtain TEM images at even higher resolutions, a smaller tip dimension is preferred. We believe that these smaller ultrasharp Pt nanoelectrodes can be prepared by an alternative method such as focused ion-beam (FIB) milling.¹⁰⁵

3.3.2. Underpotential Deposition of Cu at Au SNPEs

UPD of Cu has been carried out at Au SNPEs to estimate the size of the nanoparticle electrodes. UPD has been widely applied to measure the areas of various electrodes.¹⁰⁶ A monolayer of adatoms is formed in the UPD process, which allows for an easy calculation of the electrode area based on the charge needed to strip the adatoms. Ag,¹⁰⁷ Pb¹⁰⁸ and Cu^{109,110} are often utilized in UPD at various electrode surfaces. Recently, Zhan and Mirkin reported the characterization of nanometer-sized Pt electrodes using Cu UPD.¹⁴

To estimate the geometric area of a single Au nanoparticle immobilized at the Pt nanoelectrode, a monolayer of Cu adatoms has been first deposited at the Au SNPE.^{111,112} Before stripping, the Au SNPE was held in a 10 mM CuSO₄ solution at 0 V (vs. Ag/AgCl) for a time period between 10 s to 5 min. Then the electrode was scanned at 100 mV/s from 0 to 0.6 V (vs. Ag/AgCl) to oxidize the Cu adatoms. Figure 3-5a shows a series of voltammetric responses of a Au SNPE after UPD of Cu for different time durations. The amount of charge for the oxidation of Cu has been integrated for each case in Figure 3-5a. Figure 3-5b shows the amount of charge plotted as a function of the holding time. One can see that the Cu deposition at the Au SNPE takes about ~120 s to saturate the Au surfaces. The surface area of the Au nanoparticle was estimated based on the number of Cu adatoms needed to saturate the Au surface. A 410 $\mu\text{C}/\text{cm}^2$ conversion factor was used to calculate the surface area of the SNPE.¹⁴ From Figure 3-5, the radius of the Au nanoparticle has been determined to be ~84 nm, which is ~7 times larger than the average radii of the Au colloids (12 nm). The corresponding roughness factor (~50) suggests that Cu UPD, most likely, took place on the lateral surface of Pt wire.¹⁴ A very long saturation time (~2 min) required for Cu UPD indeed supports this conclusion.

3.3.3. Voltammetric Responses of Au SNPEs in H₂SO₄

The presence of a single Au nanoparticle at the Pt nanodisk electrode can be indicated by continuous sweeping in a 0.5 M H₂SO₄ solution. Figure 3-6 displays the voltammetric responses of a 24-nm Au SNPE in a 0.5 M H₂SO₄ solution. One can notice the major differences between the initial scans and the subsequent scans in Figure 3-6. Initially, the voltammetric response shows a cathodic peak around +0.67 V and an anodic peak around +1.12 V, which we believe correspond to the reduction of Au oxide to Au and the subsequent oxidation of Au,¹¹³ respectively, indicating the presence of Au at the nanoelectrode. In the following cycles, the above anodic and cathodic peaks were observed to decrease gradually and eventually disappear after ~200 cycles of scanning (the blue curve), which could be due to the dissolution of Au after continuous sweeping.¹¹³ However, one should also notice the appearance of a new cathodic peak (the green curve) at 0.28 V vs. Ag/AgCl, which gradually increased with increasing sweep numbers (purple curve). We believe this new cathodic peak is originated from the reduction of Pt oxide at the Pt surface,¹¹⁴⁻¹¹⁶ indicating the possible reappearance of Pt after removing the Au and the

silane layer by sweeping. The size of the Au nanoparticle at the SNPE has been estimated to be ~38 nm in diameter, calculated from the number of Au atoms from the cathodic peak at 0.67 V in Figure 3-6, which is larger than the average diameter (24 nm) of the Au nanoparticles used in preparing the electrode. However, this result does indicate the presence of both Au and Pt at the Au SNPEs.

3.3.4. Steady-State Voltammetric Response at Au Nanoparticle Arrays on a Pt UME

Figure 3-7 displays the voltammetric responses at 10 mV/s of a 25- μ m Pt microelectrode before (black), after modification with APTMS (blue), and after modification with 14-nm Au nanoparticles (red). The diffusion-limited steady-state current at the Pt microelectrode has been reduced significantly after modifying with APTMS due to the blocking of the electron transfer by the silane layer. However, when the Au nanoparticles are assembled at the modified Pt electrode, the steady-state limiting current is greatly increased. One should notice that the steady-state current at the Au-nanoparticle array is only 30% of the total current observed at the bare Pt electrode possibly due to a relatively low density of coverage. It has been reported that increasing particle density can increase the peak current at an array of Au nanoparticles assembled on a macroscopic electrode.¹¹⁷ However, the peak current obtained at the bare electrode should represent the maximum possible current on nanoparticle arrays on the same electrode. In the case of a single Au nanoelectrode, however, the diffusion-limited steady-state current can actually exceed that obtained at the bare nanoelectrode, as shown in the following experiments.

3.3.5. Steady-State Voltammetric Response at Au SNPEs

The Au SNPEs have been examined using steady-state cyclic voltammetry. Figure 3-8 and Figure 3-9 show a comparison of the steady-state voltammetric responses of Au SNPEs, APTMS modified Pt nanoelectrodes, and bare Pt nanodisks in aqueous solutions containing 5 mM $\text{Fe}(\text{CN})_6^{3-}$ (Figure 3-8) and 5 mM $\text{Ru}(\text{NH}_3)_6^{3+}$ (Figure 3-9), respectively. From Figure 3-8a, it can be seen that a typical sigmoidal-shaped voltammetric response was observed using an 8-nm bare Pt nanoelectrode (black). After modification with APTMS at the Pt, the steady-state limiting current was greatly reduced (red), indicating the blockage of electron transfer due to the silane modification. However, when a 14-nm Au nanoparticle was immobilized at the surface of the Pt, the limiting current was greatly enhanced (green). Similar

enhancements have been previously reported using an array of Au nanoparticles at macroscopic electrodes.¹¹⁸⁻¹²⁰ It is interesting to note that the inhibition of voltammetric current for nanoelectrode is different than for 25- μm electrodes. For 25- μm electrode, the silane-modification results in around 80% inhibition of the limiting current from Figure 3-7. However, the inhibition is around 30-70% at nanoelectrodes shown in Figure 3-8 and Figure 3-9. We believe that the inhibition of voltammetric current at the silane modified electrodes is mainly due to an increase in the electron-transfer resistance caused by the increase in the electron-transfer distance, which is due to the presence of the silane self-assembled monolayer (SAM). The formation of high quality silane SAMs is possibly easier at a microelectrode than at a nanoelectrode less than 5 nm due to more edge areas at the nanoelectrode. Therefore, we believe the difference in the current inhibition at the microelectrode and the nanoelectrode is mainly due to more defects in the SAMs at the Pt nanoelectrodes.

The steady-state current shown in Figure 3-8a has been significantly enhanced than that collected from the bare Pt nanoelectrode, which might be due to the larger size of the 14-nm Au nanoparticle relative to the disk Pt nanoelectrode (diameter = 8 nm). Figure 3-8b and 3-8c show similar responses at Au SNPEs prepared using 18, and 24 nm Au colloids, respectively. Similar steady-state voltammetric responses have also been observed using $\text{Ru}(\text{NH}_3)_6^{3+}$ as redox species, as shown in Figure 3-9. The diffusion limited steady-state current at the Au nanoparticle electrode is significantly greater than that at the Pt nanodisk electrode due to a larger size of the Au compared to the Pt.

The magnitude of steady-state limiting current has been found to be determined by the size of Au nanoparticle, and less dependent on the size of the Pt nanoelectrode. The steady-state limiting current, i_{ss} , at the Au nanoparticle electrode can be estimated using the following equation, assuming a spherical geometry at an infinitely large surface,⁹⁰

$$i_{ss} = 4\pi(\ln 2)nFD C^* a \quad (3-1)$$

where D and C^* are the diffusion coefficient and bulk concentration of the redox molecule, n is the number of electrons transferred per redox molecule, and a is the radius of the Au nanoparticle, respectively. The steady-state limiting currents at Au SNPEs have been obtained from the voltammetric responses in a 5

mM $\text{Fe}(\text{CN})_6^{3-}$ solution, as listed in Table 3-1. Also listed in Table 3-1 are the values calculated using equation 3-1 based on the average size of the Au nanoparticle observed from TEM characterizations, as shown in Figure 3-2. At least five Au SNPEs have been utilized to obtain each voltammetric data shown in Table 1. From Table 3-1, it can be seen that the steady-state limiting current at Au SNPE measured from CVs (i_{cv}) is in fairly good agreement to that estimated from TEM characterizations using equation 1 (i_{cal}) for the 14, 18, and 24 nm Au nanoparticles. The measured limiting currents are 13.4%, 5.9%, and 15.4% greater than those calculated from the 14-nm, 18-nm, and 24-nm nanoparticles, respectively. We are not entirely sure why the measured limiting current is greater than estimated from size of the nanoparticles. We speculate that the Pt electrode could possibly contribute to the measured faradaic response. There are several possible methods to prevent the supporting nanoelectrode from contributing to the faradaic responses. The first method will be to decrease the size of the Pt nanoelectrode so that redox molecules will not be able to reach the supporting electrode due to hindering from the nanoparticle. Second, longer silane linker molecules could be used to further decrease electron-transfer between the Pt and the redox molecules. Alternatively, an inert electrode material could be used as the supporting electrode so that faradaic processes can only happen at the nanoparticles.³¹⁻³³

3.3.6. Oxygen Reduction at Single Au Nanoparticles

One of our goals in developing SNPEs is to study the structure-function relationship in nanoparticle-based electrocatalysis. To demonstrate that electrocatalytic responses can be obtained at a single-nanoparticle level, we have measured the voltammetric responses of the Au SNPEs in ORR. Figure 3-10a displays a comparison of the steady-state voltammetric responses in an oxygen-saturated aqueous solution containing 0.10 M KOH, of a same Pt nanoelectrode before (red) and after modification with APTMS (green), and the corresponding 18-nm Au SNPE (black). The cyan curve in Figure 3-10a shows the voltammetric response of the Au SNPE in the same solution after degassing with a flow of N_2 . In a 0.10 M O_2 -saturated KOH solution, the bare Pt nanoelectrode exhibits a two-step process for oxygen reduction with the onset potentials of ca. -0.35 V and -1.0 V (not shown), respectively, indicating a two-step four-electron reduction pathway of O_2 to OH^- (through HO_2^- as an intermediate).^{121,122} When silane monolayer is attached at the Pt electrode, the half-wave potential for oxygen reduction is shifted to about

-0.60 V and the limiting current decreased significantly, which indicates that the ORR is significantly hindered by the silane monolayer. However, the Au SNPE exhibits a one-step process for the ORR with an increased limiting current than that obtained at the bare Pt nanoelectrode, and the process has a four-electron pathway.¹²² Moreover, it can be seen that the half-wave potential for the ORR at the Au SNPE is shifted to -0.07 V compared to the bare Pt nanoelectrode. From above results, it can be concluded that the Au SNPE has good electrocatalytic activity for the ORR.

The electrocatalytic activity for the ORR has been compared at Au nanoparticles of different sizes. Figure 3-10b shows a comparison of the voltammetric responses in an oxygen-saturated aqueous solution containing 0.10 M KOH of a bare Pt nanoelectrode (black) and three Au SNPEs of different sizes (14-nm Au SNPE (red), 18-nm Au SNPE (green), and 24-nm SNPE (blue)). It can be seen that the steady-state limiting current increases with increasing size of the Au nanoparticle. The half-wave potentials at larger Au nanoparticles are also shifted to higher potentials, indicating higher catalytic activity at larger Au nanoparticles. A summary of the steady-state limiting current and the half-wave potential at three different Au SNPEs has been given in Table 3-2. The average limiting currents have been found to be 1.0, 1.7, and 2.0 pA, for the 14, 18, and 24-nm Au SNPEs, respectively. The half-wave potentials have been shifted from \sim -365 mV at bare Pt nanoelectrode to -130 mV at the 14-nm SNPEs, -75 mV at the 18-nm SNPEs, and -35 mV at the 24-nm SNPEs.

The peak current has been utilized to compare the electrocatalytic activity of nanoparticle arrays at macroscopic electrodes. However, unlike macroelectrodes that the peak current is proportional to the surface area,⁴ the limiting current is proportional to the radius of the electrode for a spherical nanoelectrode. Therefore, the steady-state limiting current should be normalized to the radius of the Au nanoparticle to estimate the electrocatalytic activity for ORR, and the results are also listed in Table 2. It can be seen that the normalized steady-state limiting currents are 0.14, 0.19, and 0.17 pA/nm, for the 14, 18, and 24-nm Au nanoparticles, respectively. The 18-nm Au nanoparticles show slightly better electrocatalytic activity for ORR than the 14 and 24 nm particles. The half-wave potentials for ORR at the Au nanoparticles are significantly higher than that at the bare Pt nanodisks, indicating higher electrocatalytic activity at the Au nanoparticles than at the Pt disks. Further investigation of the half-wave

potentials from Table 3-2 indicates that the 24-nm Au nanoparticles possibly have higher catalytic activity than the smaller nanoparticles due to a slightly higher half-wave potential toward ORR. Further experiments are needed to quantitatively understand how the voltammetric responses of the Au nanoparticles could depend on the size and the material of the nanodisk, and the properties of the linker molecules. These experiments are ongoing in our laboratory.

3.4. Conclusions

In this chapter we have demonstrated the construction and characterization of the Au SNPE. The Au SNPE has been characterized by means of TEM, steady-state voltammetry, and UPD. It has been shown that the presence of a single Au nanoparticle can greatly enhance the electron-transfer from the Pt to the redox molecules. The voltammetric response at Au SNPE depends more on the size of the Au nanoparticle than the size of the Pt nanoelectrode. The Au SNPE has been utilized to examine the ORR in a KOH solution to explore the feasibility of comparing electrocatalytic activity at a single-nanoparticle level. It has been found that Au SNPEs exhibit good size-dependent electrocatalytic activity towards ORR, which could also be affected by the Pt nanoelectrodes.

3.5. Tables and Figures

Table 3-1. The steady-state limiting currents of 5 mM $\text{Fe}(\text{CN})_6^{3-}$ using Au SNPEs measured from voltammetric response and TEM characterization.

Au diameter	14 nm	18 nm	24 nm
i_{cv} (pA)	13.5 ± 1.1	16.2 ± 2.8	22.4 ± 2.4
i_{cal} (pA)	11.9 ± 2.7	15.3 ± 3.3	19.4 ± 2.8
Difference%	13.4%	5.9%	15.4%

Table 3-2 The electrocatalytic activity for ORR using bare Pt nanoelectrodes and Au SNPEs. Pt electrode size: ~7.0 nm in diameter, CV scan rate: 10 mV/s.

Electrode type	Bare Pt	14 nm Au	18 nm Au	24 nm Au
i_{lim} (pA)	--	1.0 ± 0.2	1.7 ± 0.4	2.0 ± 0.3
$E_{1/2}$ (mV)	-365 ± 25	-130 ± 17	-75 ± 10	-35 ± 7
i_{lim}/a (pA/nm)	--	0.14	0.19	0.17

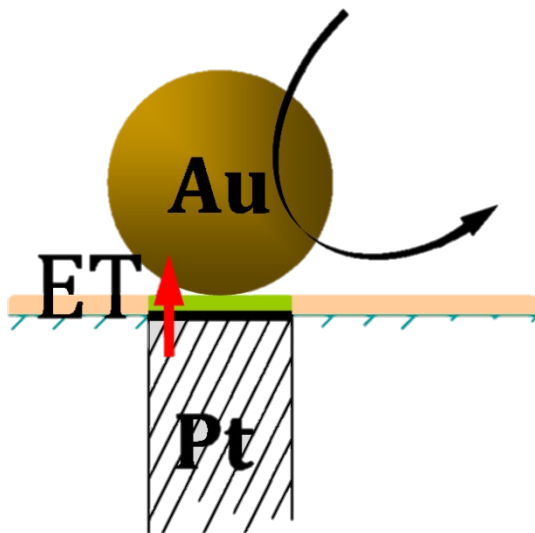


Figure 3-1. A schematic drawing of a Au SNPE.

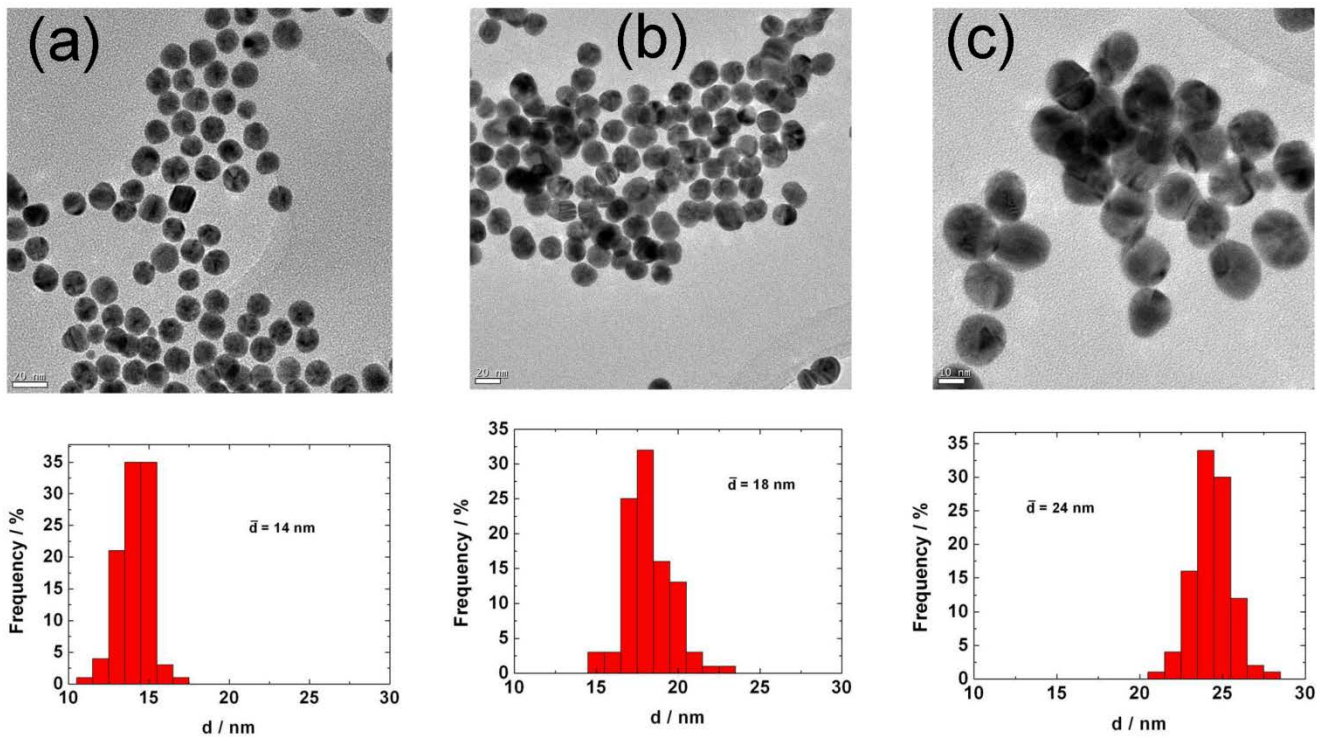


Figure 3-2. TEM Images of Au nanoparticles of three different sizes: 14, 18, and 24 nm. Scale bars are 20, 20 and 10 nm for (a), (b), and (c) respectively.

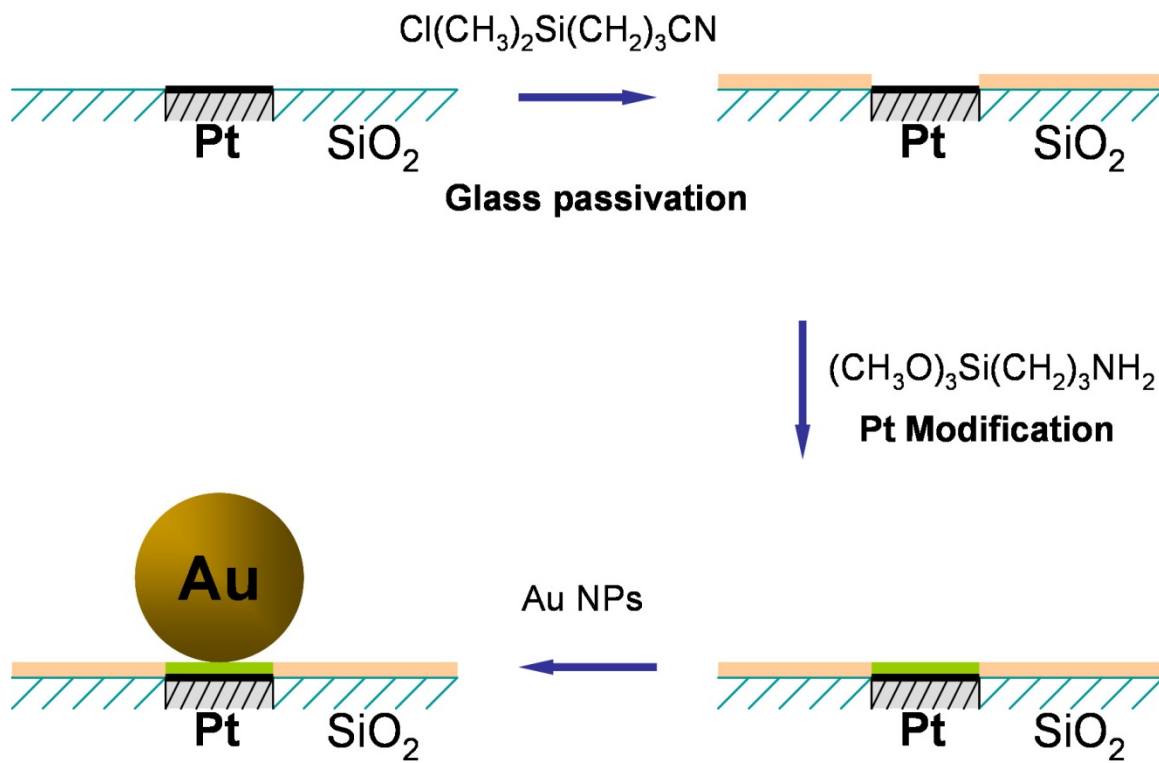


Figure 3-3. Fabrication scheme of the Au SNPE.

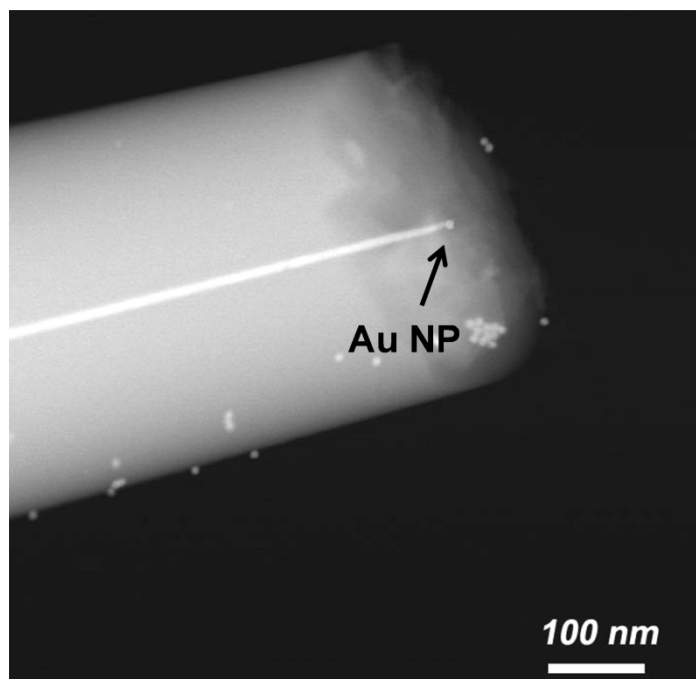


Figure 3-4. A TEM image of a single Au nanoparticle immobilized on a Pt nanoelectrode.

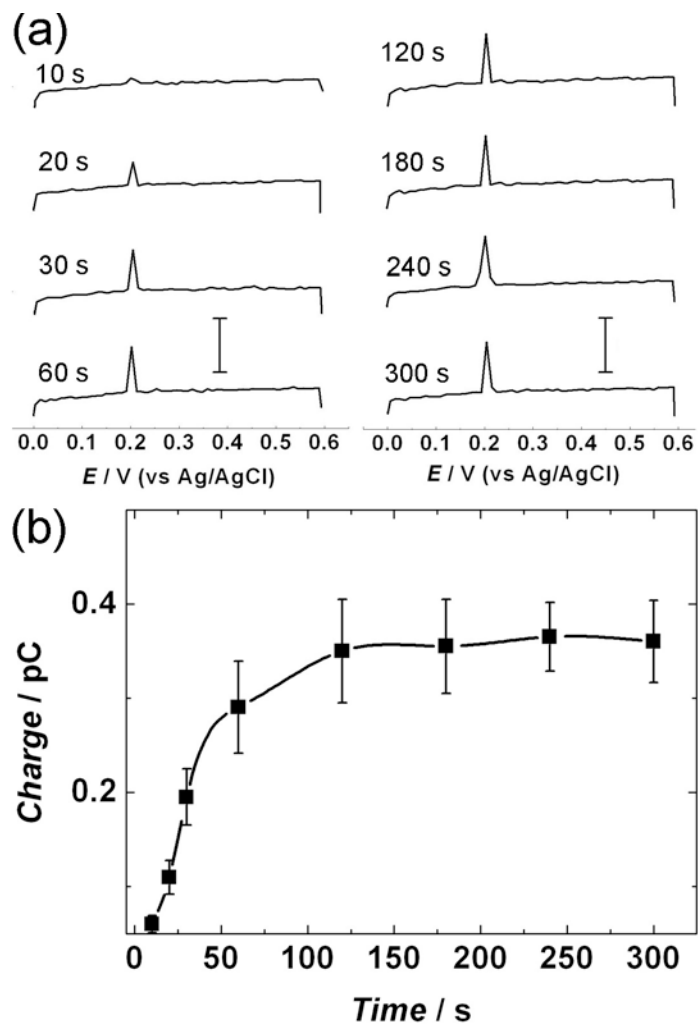


Figure 3-5. (a) Voltammetric responses of underpotential deposited copper from a 24-nm Au SNPE. Before stripping, the electrode was held at 0 V vs. Ag/AgCl for 10 s, 20 s, 30 s, 1 min, 2 min, 3 min, 4 min and 5 min. Pt electrode diameter: ~ 10 nm, Scan rate: 100 mV/s. (b) The relationship between the charge obtained from each stripping peak and the UPD holding time. The scale bars in (a) are 3 pA.

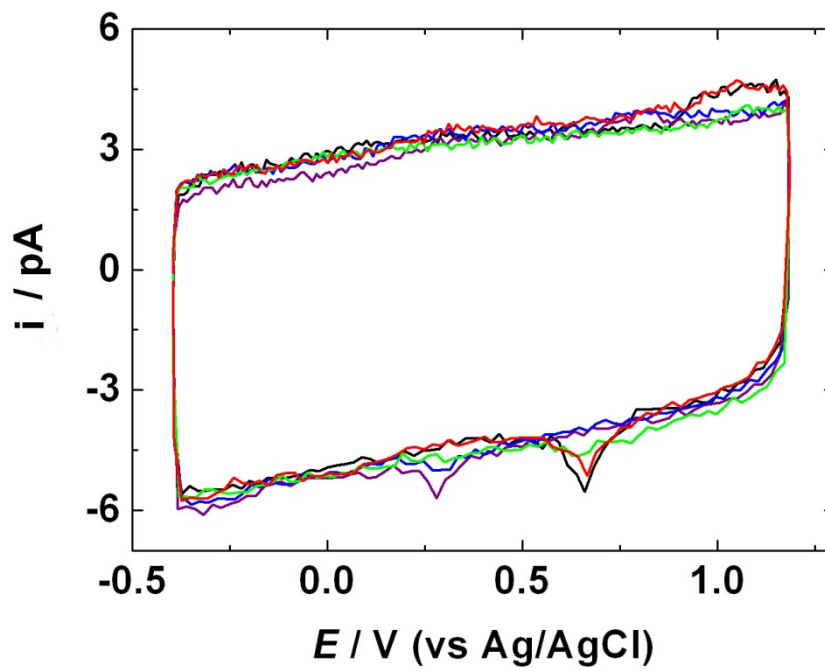


Figure 3-6. The voltammetric responses of a 24-nm Au SNPE in a 0.5 M H_2SO_4 solution after 1st time scanning (black), 10th time scanning (red), 50th time scanning (green), 200th time scanning (blue), and 500th time scanning (purple). Scan rate: 100 mV/s.

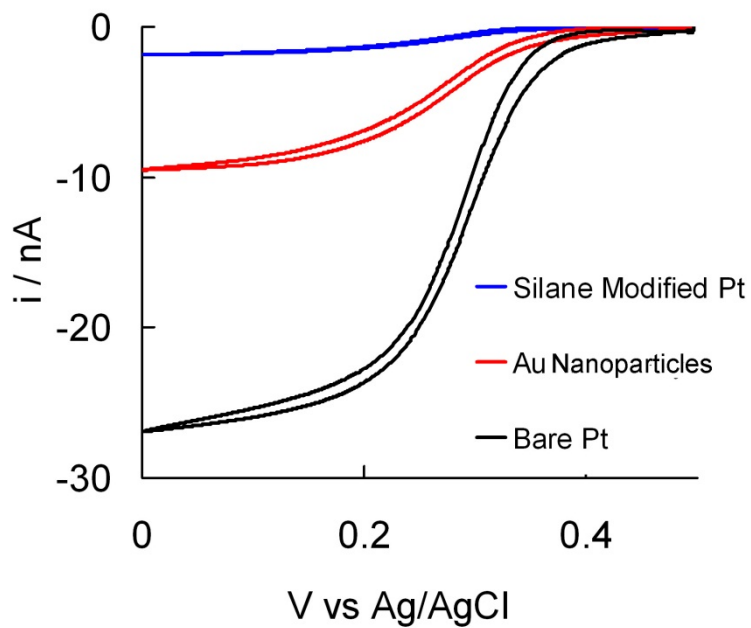


Figure 3-7. Voltammetric responses of a 25- μm Pt microelectrode in a 5.0 mM $\text{K}_3\text{Fe}(\text{CN})_6$ solution containing 0.2 M KCl before (black), after modification with APTMS (blue), and after modification with 12-nm Au nanoparticles (red). Scan rate: 10 mV/s.

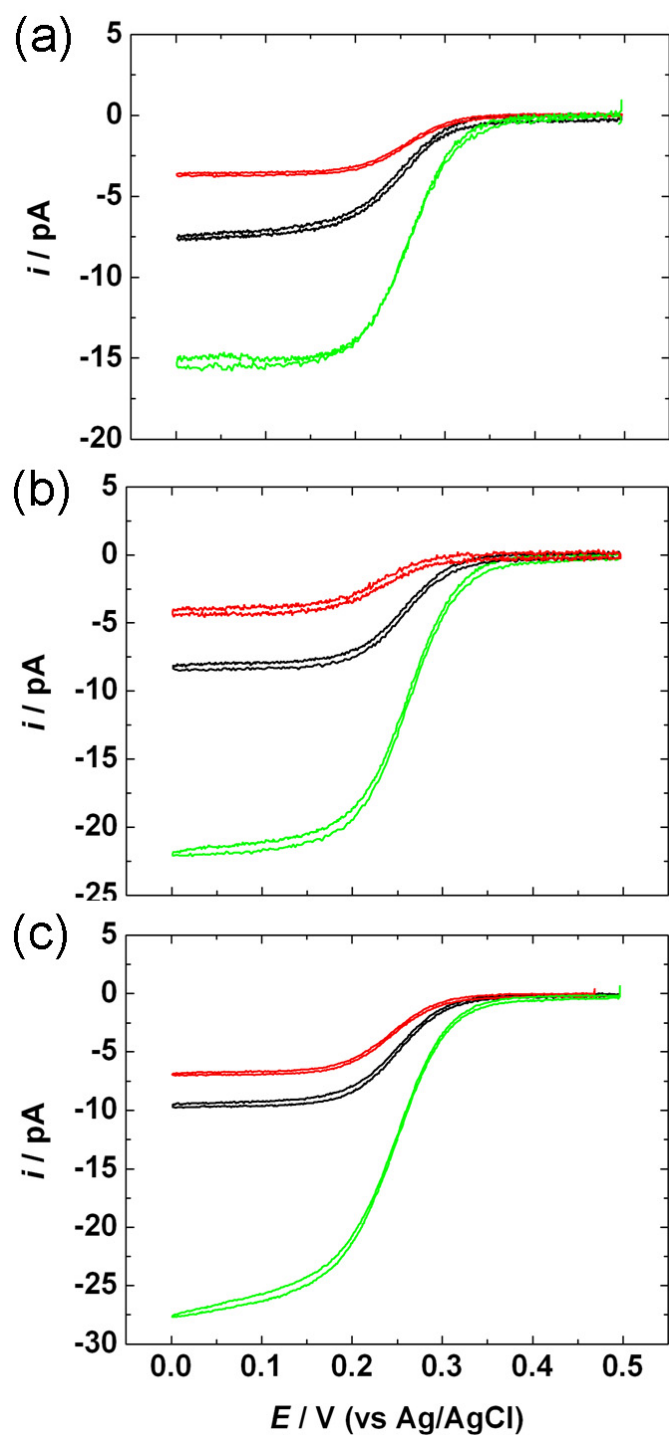


Figure 3-8. Voltammetric responses of 5.0 mM $\text{K}_3\text{Fe}(\text{CN})_6$ in a 0.2 M KCl solution using bare Pt electrodes (black), APTMS-modified Pt electrodes (red), and Au SNPEs (green). Scan rate: 10 mV/s. The diameters of the Pt electrodes and the Au SNPEs are about 8.0 nm and 14 nm (a), 9.0 nm and 18 nm (b), and 9.0 nm and 24 nm (c), respectively.

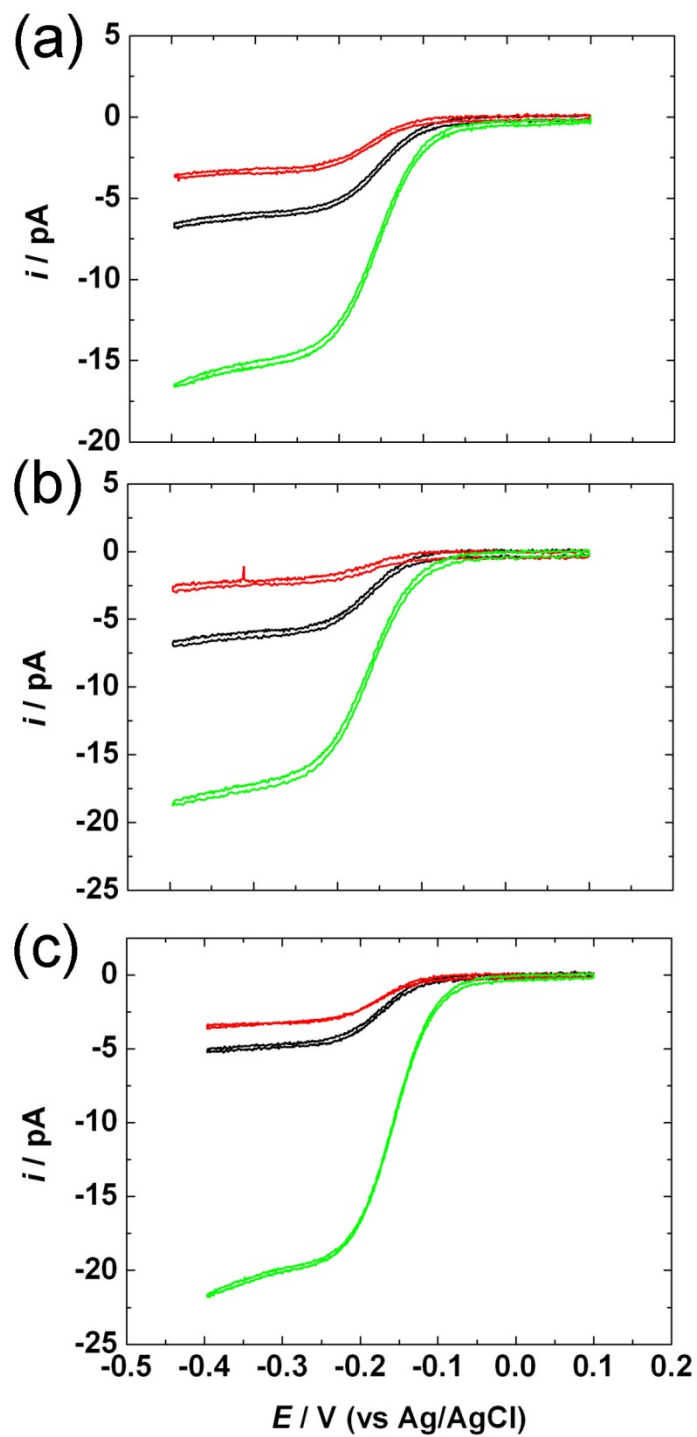


Figure 3-9. Voltammetric responses of 5.0 mM $\text{Ru}(\text{NH}_3)_6\text{Cl}_3$ in a 0.2 M KCl solution using bare Pt electrodes (black), APTMS-modified Pt electrodes (red), and Au SNPEs (green). Scan rate: 10 mV/s. The diameters of the Pt electrodes and the Au SNPEs are about 7.5 nm and 14 nm (a), 6.8 nm and 18 nm (b), and 6.2 nm and 24 nm (c), respectively.

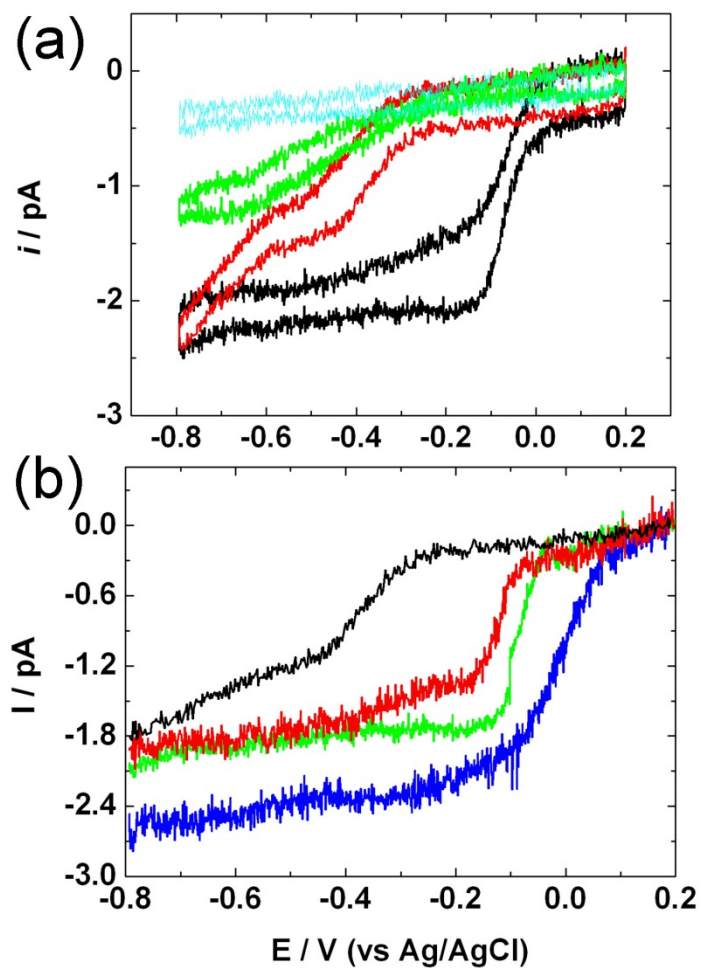


Figure 3-10. (a) Voltammetric responses of a 0.10 M KOH solution using a 18-nm Au SNPE (black), APTMS-modified Pt nanoelectrode (green), and the bare Pt nanoelectrode (red) after oxygen bubbled, and a 18-nm Au SNPE after nitrogen bubbled (cyan). (b) Voltammetric responses of an oxygen-saturated 0.10 M KOH solution using a bare 7-nm-diameter Pt nanoelectrode (black), a 14-nm Au SNPE (red), a 18-nm Au SNPE (green), and a 24-nm Au SNPE (blue). Scan rate: 10 mV/s.

CHAPTER 4 STABILITY OF Pt NANOELECTRODES IN A SULFURIC ACID SOLUTION UNDER POTENTIAL CYCLING

4.1. Introduction

The practice of potential cycling is used to activate and clean electrodes prior to experimentation.⁴ In this method electrodes are placed in solutions of sulfuric acid and the potential is swept between potential regions where hydrogen and oxygen evolution occurs. In this manner surface impurities desorb by repeatedly oxidizing and reducing the electrode surface returning the electrode to a reproducible state.¹²³ However in our studies with Pt nanoelectrodes we observed that after cycling the potential at the electrode surface to clean the electrode there was an appreciable decrease in the magnitude of the diffusion-limited steady-state current observed. This decrease in current is indicative of a hindrance on the mass transfer of the redox molecule to the electrode surface which could arise due to a decrease in electroactive surface area or a change in electrode geometry.

Potential cycling has also been used extensively to study the stability of Pt based catalytic materials.¹²⁴⁻¹²⁶ The nature of catalytic experiments require materials to be repeatedly cycled which can potentially be problematic as oxide formation and surface roughening can adversely affect the catalytic properties of a metal substrate. Pt based electrodes used in polymer electrolyte fuel cells are limited by long term stability issues especially under potential cycling conditions. Over time, the Pt surface can deteriorate due to a loss of electrochemical surface resulting in a decrease in catalytic performance.^{127,128} The loss of electrochemically active surface area can partially be attributed to Pt dissolution and as such the mechanism of Pt dissolution has garnered much research interest.¹²⁹⁻¹³³

In this work we present evidence that by potential cycling in an acidic solution, Pt nanoelectrodes are effectively etched resulting in the formation of a recessed electrode. We believe that Pt dissolution is the primary cause of this phenomenon. Pt dissolution is known to occur with larger electrodes but because the electrochemical surface area is sufficiently large small losses in electrochemical surface area are not distinguishable by steady-state voltammetry. However when the critical dimensions of an electrode approach the nanometer scale the presence of a small cavity can greatly affect the mass transfer rate and diffusion of species to the electrode surface.^{13,33,56,134} In this work we characterize the

formation of a nanopore by cyclic voltammetry, scanning electron microscopy (SEM), and finite element simulations.

The information herein also provides interesting insights into the stability of Pt-based electrocatalysts because we are able to observe the dissolution rate on Pt nanosurfaces comparable in size to the Pt nanoparticles currently utilized in many fuel-cell applications. Typical electrodes employed in previous experiments probing Pt catalytic stability have a much larger surface area and utilize either bulk Pt^{125,135} or Pt deposited on a substrate^{133,136} however in this study we are able to study the stability of Pt electrodes with an electrochemically active surface area as small as $\sim 8 \text{ nm}^2$. By evaluating the etching rate of the nanoelectrodes, we are able to study the dissolution and degradation of single layers of Pt from the electrode surface. By comparing the different etching rate of different-size Pt nanosurfaces, we can evaluate the stability of these Pt nanosurfaces. Therefore, this type of analysis can possibly shed light on the stability of Pt-based nanocatalysts in acid environments and examine the role of adsorption of surface impurities and Pt dissolution play in the fouling of Pt-based catalysts.

4.2. Experimental Section

4.2.1. Finite-Element Simulations

Steady-State and transient responses for a disk nanoelectrode, and nanopore electrode were assessed using Comsol Multiphysics software (Comsol, Inc.) operated on a Dell Precision workstation (Xeon CPU, 2.66 GHz, 8 GB RAM). Details of the model are outlined in the results and discussion section.

4.3. Results and Discussion

4.3.1. Electrode Characterization

It is essential the nanoelectrodes are characterized prior to experimentation because their electrochemical responses are sensitive to small geometric variations. As nanoelectrodes are exposed by polishing it is important to ensure that the final electrode does indeed have disk geometry and is not recessed. This is accomplished by closely monitoring the polishing process and continually checking the *i-V* response until a consistent value for the steady-state current in solution is obtained. Because the Pt

wire at the end of the sharp tip has quasi-cylindrical geometry the change in geometric area caused by polishing will only slightly offset the limiting current and a disk nanoelectrode can be readily obtained. In this experiment the steady-state behavior of nanoelectrodes were tested in a 5 mM Fc and 0.1 M TBAPF₆ in MeCN solution. After a consistent sigmoidal signal was observed the radius of the electrode was determined by cyclic voltammetry. The diffusion-limited steady-state current at an inlaid disk electrode is given by⁴

$$i_{ss} = 4nFDC^*a \quad (4-1)$$

where n is the number of electrons transferred, F is the Faraday constant, D the diffusion coefficient and C^* the bulk concentration of the redox species in solution, and a is the radius of the electrode.

Electrodes were also characterized in a sulfuric acid solution. Figure 4-1 shows a representative voltammogram of a 40 nm Pt nanoelectrode in a solution of 0.5 M H₂SO₄ before and after potential cycling. The potential at the electrode was cycled from -0.2 V to +1.4 V vs. Ag/AgCl at a scan rate of 100 mV/s. The red curve illustrates the initial scan that was obtained after the polishing procedure and the black curve is the response obtained after the potential at the electrode surface has been cycled 20 times. After 20 cycles the features characteristic for hydrogen and oxygen absorption/desorption features which are consistent for Pt in H₂SO₄ and similar to what would be obtained on a millimeter-sized electrode become more pronounced indicating a clean Pt surface.¹³⁷

4.3.2. Finite-Element Simulations of the Steady-State Response

In order to test the hypothesis that the decrease in current observed resulted from the formation of a nanopore electrode, we conducted finite-element to simulate and quantitatively characterize the voltammetric response of a disk nanoelectrode and a corresponding nanopore electrode. Figure 4-2 shows the two dimensional geometry of the model used for the numerical simulation. The model utilized a cylindrical coordinate system with the origin ($z = 0$, $r = 0$) corresponding to the center of the disk electrode and pore orifice. We followed a previously described method^{33,138} with minor modifications applying the model for cylindrical geometry. We modeled a reversible 1-electron oxidation reaction,

$R \rightarrow O + e^-$, assuming that the diffusivities of the reduced and oxidized species are equal. In this model we assume that the mass transport is due solely to diffusion and that the reaction is reversible. The boundaries of the bulk solution were fixed at $C^* = 5 \text{ mM}$ and the flux at the glass surfaces were set to zero. To model Fc the diffusion coefficient, D , was set to $2.47 \times 10^{-5} \text{ cm}^2/\text{s}$. One can derive the surface concentration of species O and R designated $C_{O,s}$, and $C_{R,s}$ respectively, from the Nernst equation, $E = E^0 + \frac{RT}{nF} \ln \left(\frac{C_{O,s}}{C_{R,s}} \right)$, and mass balance $C_{O,s} + C_{R,s} = C^*$. To simulate the i - V curves of a nanodisk and cylindrical nanopore electrodes the surface concentration of the reaction species R is given by

$$C_{R,s} = C^* / \left(1 + \exp \left[\frac{nF}{RT} (E^0 - E(t)) \right] \right) \quad (4-3)$$

where E^0 is the formal potential, and E is the electrode potential. For simplicity in our experiments the formal potential was set to zero. An infinite-Fourier series was used to model the triangular-shaped waveform is given by the following equation

$$E(t) = \frac{8(E_{range})}{\pi^2} \sum_{k=0}^{\infty} (-1)^k \frac{\sin((2k+1)\omega t)}{(2k+1)^2} \quad (4-4)$$

where E_{range} is the range of the voltage scan, ω is the angular frequency of the wave which is given by $\frac{\pi v}{(2E_{range})}$. An accurate waveform was obtained by using values of k from 0 to 7. Equation 4-3 was set as the boundary condition at the electrode surface in our model.

Figure 4-3a shows the simulated i - V response of a 5 nm disk electrode, and the corresponding nanopore electrode with a 5 nm pore orifice. It is observed that as the depth of the pore increases the value for the steady-state current decreases. The steady-state response of various sized disk nanoelectrodes and their corresponding nanopore electrodes were also simulated using Comsol. This decrease in current is attributed to an increase in the mass transfer resistance. As a pore is formed, the additional solution mass transfer resistance for the solution within the pore must be accounted for. The total mass transfer resistance will be a summation of the external mass transfer resistance and the mass

transfer resistance inside the pore. Accounting for this additional resistance Bond et. al. derived an analytical expression for the steady-state current at a recessed disk microelectrode,¹³⁹

$$i_{ss} = \frac{4\pi nFDC^*a^2}{4d+\pi a} \quad (4-5)$$

where d represents the depth of the nanopore and a the pore orifice. Further work was conducted by Sun to apply that theory to recessed nanoelectrodes, in which the conclusion is made that in a nanometer sized cavity the diffusivity of a redox species due to a “random walk” process could differ from bulk behavior.⁵⁶

Figure 4-3b shows a plot of the current obtained at a nanopore electrode normalized to a disk electrode with the same pore orifice ($i_{ss}/i_{ss}^{d=0}$) plotted against ratio d/a . It is observed that as the depth of the pore increases the magnitude of the current will proportionately decrease. This plot is used to calculate the pore depth in our experiments by comparing the ratio of the steady-state current measured before and after potential cycling to the ratio of d/a . We compared the values for pore depth obtained from our simulations and calculated from equation 4-5 and found that they were mostly in agreement. For electrodes less than 10 nm our simulated results agreed within 5% of equation 4-5 and for larger electrodes the percent difference was slightly higher at around 10%.

4.3.3. Pt Dissolution Under Potential Cycling

We have observed that as an undesired result of potential cycling, especially in the case of Pt nanoelectrodes, the magnitude of the steady-state current decreases. Figure 4-4a shows the steady-state voltammetric response of a Pt disk nanoelectrode of Fc oxidation before and after potential cycling in H₂SO₄ from -0.2 V to +1.2 V at 100 mV/s. The radius of the nanodisk as obtained from the magnitude of the steady-state current (black curve) and equation 4-1 is 2.7 nm. After cycling the electrode for 20 cycles in H₂SO₄ the electrode was thoroughly rinsed with water and allowed to dry. Afterwards the electrode was placed again the Fc solution and a CV was recorded. We observed a 33% decrease in the magnitude ($i_{ss}/i_{ss}^{d=0} = 0.66$) of the steady-state current (red curve). This corresponds to a pore depth of 1.0 and 1.1 nm as determined from our simulation and equation 4-5 respectively. After an additional 20

cycles the pore was further etched to a depth of 3.9 nm. Similar results were observed at slightly larger electrodes such as the example shown in figure 4-4a. The radius of the electrode as obtained from the initial steady-state response is 160 nm. After 20 cycles the current had decreased by 6% ($i_{ss}/i_{ss}^{d=0} = 0.94$) corresponding to a pore depth of 7.8 nm. The observed decrease in current is much smaller when compared to the decrease observed in the electrode utilized in figure 4-4a after a similar number of potential cycles. As the electrode was continually scanned in sulfuric acid, we observed that the magnitude of the steady-state current continually decreased. However the rate of decrease in current was significantly slower than observed at the smaller electrode.

Figure 4-5 shows the i - V response of a 1.2 μm electrode before and after potential cycling. The black curve is the initial CV and the red curve is the response after the electrode has been cycled for 220 cycles. The current has only decreased to 97% of the original value corresponding to a 26 nm pore depth. Because d/a is so large, a pore of that magnitude has little effect on the steady-state response. In the case of larger electrodes ($a > 500$ nm) repeated cycling in sulfuric acid doesn't cause a significant decrease in the magnitude of the steady-state current. As illustrated in our simulations in figure 4-3b, a disk electrode exhibits a 50% decrease in current when the d/a ratio is roughly 1. This implies that in order for an inlaid disk electrode with a radius of 500 nm to have a 50% decrease in current the pore depth would need to reach 500 nm. We also tested 12.5 μm Pt disk electrodes and observed no significant decrease in the magnitude of current observed after 200 cycles.

4.3.4.SEM Characterization of a Recessed Disk Nanoelectrode

One of the inherent difficulties which arise in working with nanoelectrodes is the inability to visualize the electrode surface via conventional microscopic techniques. Cyclic voltammetry alone is unable to conclusively support our hypothesis, however combined with an advanced imaging technique such as SEM; we can correlate the observed effects of potential cycling from cyclic voltammetry to a geometrical change. Figure 4-6a shows an SEM image of a Pt disk nanoelectrode after potential cycling in H_2SO_4 and figure 4-6b shows the i - V behavior before and after cycling. From the initial voltammogram the radius is calculated to be 230 nm and by analysis of the current ration before and after cycling the calculated pore depth was 280 nm. Both of these values are in agreement with the SEM data and the

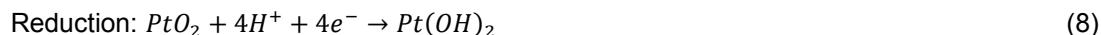
SEM image clearly reveals a nanopore electrode confirming our initial hypothesis. The electrodes prepared for SEM imaging followed the same fabrication method with the exception of the sealing of the pulled tip in the borosilicate glass. The omission was necessary to remove the thick insulating glass which interfered with imaging.

4.3.5. Mechanism of Pt Dissolution

Both steady-state and SEM confirm our hypothesis that potential cycling causes the etching of the nanodisk surface. We believe this etching phenomenon occurs because of Pt dissolution. The two main pathways for Pt dissolution occur either through a direct dissolution of the metal or the production of an oxide film and a subsequent reduction. Studies on the stability of Pt in acidic media have shown that under potential cycling conditions Pt dissolution occurs via the second mechanism, the formation of metal oxides on the electrode surface and their reductions through potential cycling.^{125,140} The formation of Pt oxides occurs through the oxidation of Pt:



One proposed mechanism of Pt ion formation from dissolution involves two steps, as the oxide is first reduced from $Pt(IV) \rightarrow Pt(II)$ or $Pt(II) \rightarrow Pt(I)$ with the second step being an ionization reaction that ionizes the reduced Pt hydroxide compound to its respective Pt ion.^{124,135} This reaction is shown for the Pt (IV)



The above reactions are still under consideration but it is believed that Pt dissolution occurs not due to a direct dissolution of the metal but via an intermediate surface oxygen species.^{132,141} A recent report by Sugawara et. al., outlined a proposed mechanism demonstrating the formation of Pt oxides occurs from 0.8 to 1.1 V vs. SHE and that surface coverage increases with increasing potential.¹³² Pt dissolution is significantly enhanced when the upper potential limit is above 1.2 V vs. SHE and only occurs when the lower limit of the cycling potential is less than 0.6 V vs. SHE where Pt oxides are reduced completely back to Pt.

To test the applicability of Pt dissolution being the primary mechanism for the observed decrease in the magnitude of steady-state current, we cycled electrodes of different sizes in 0.5 M H₂SO₄ at with varying potential ranges. Figure 4-7 shows the effect that changing the upper potential limit during cycling has on the magnitude of steady-state current on a 50 nm and 130 nm Pt disk nanoelectrode. Electrodes were cycled for 20 cycles at a given range, e. g., -0.2 V to +0.4 V and the steady-state response was obtained in 5 mM Fc before and after potential cycling. It was observed that the decrease in limiting current was not statistically significant until the positive potential reached +1.2V and that the observed decrease in current magnitude became much larger as the potential was increased above that limit. As supported by the proposed Pt dissolution mechanism the positive potential limit must reach a high enough potential such that Pt oxidation occurs. These observations are in agreement with results presented by Yadav et. al. that significant Pt dissolution occurs upon potential cycling when the potential reaches higher than 1.4 V vs. SHE.¹⁴² From these results we conclude that the observed decrease in steady-state current arises as a result of Pt dissolution and a subsequent increase in the mass transfer resistance due to the formation of a nanopore.

4.3.6.Determination of Pt Dissolution Rate

The dissolution rate was obtained by cycling electrodes of sizes in 0.5 M H₂SO₄ at a voltage range between -0.2 V to +1.2 V for a total of 200 cycles. Electrodes were cycled in 20 cycle increments and after every 20 cycles the steady-state behavior in Fc was obtained. From the decrease in the steady-state current the pore depth was calculated by figure 4-3b and the volume of Pt displaced was calculated. In this calculation we assume that the etching effect is isotropic and that the volume displaced has cylindrical geometry. Assuming an atomic volume of 9.10 cm³/mol for Pt we were able to calculate the amount of Pt dissolved in a single cycle. Table 1 shows the calculated Pt dissolution rate as determined from steady-state voltammetry for various sized nanoelectrodes. The calculated dissolution rate ranged from 33.0 ± 7.4 ng cm⁻² per cycle for a 2.7 nm disk nanoelectrode to 711.7 ± 79.1 ng cm⁻² per cycle for a 240 nm disk nanoelectrode. Previously observed Pt dissolution rates under conditions of potential cycling with the upper limit between 1.2 and 1.5 V vs. SHE have typically ranged between 2 – 5 ng cm⁻² per cycle.^{124-126,136} Our results are significantly larger than those previously observed. We believe that the

significant difference arises because of the increased mass transfer rate of nanoelectrodes compared to macroscopic electrodes. In the previous studies the dissolution rate was calculated at electrodes with a much larger electrochemically active surface area, typically in the range of 1.5 cm^2 . In contrast, a 240 nm disk electrode has a surface area of roughly $1.8 \times 10^{-9} \text{ cm}^2$ which is multiple orders of magnitude smaller. Because of this such small electrode size radial diffusion will dominate as opposed to a linear diffuse profile at macroscopic electrodes.⁴ Because of the radial diffusion profile, when a Pt atom is dissolved from the substrate it will diffuse away quickly and be unable to redeposit to the electrode surface. This is unlike electrodes with larger surface areas where Oswald ripening can occur and the dissolved Pt species can redeposit on larger particles.^{143,144} In previous studies dissolved Pt from potential cycling has been detected using inductively coupled plasma mass spectrometry (ICP-MS),¹³⁶ colorimetry,¹²⁶ or atomic absorption spectroscopy.¹²⁵ However we are unable to confirm our results with any of these methods because the amount of Pt dissolved from a nanoelectrode is well under their detection limits.

Another metric that has been used to study Pt dissolution is the charge difference between the anodic and cathodic charges from in the oxygen adsorption and desorption regions in the *i-V* curve in H_2SO_4 . Figure 4-8 contains a plot of the charge difference normalized to the electrode area for electrodes of different sizes. We observed that as the electrode size decreased, the charge difference increased. This difference in charge implies that not all of the Pt oxide compounds are reduced back to Pt and that a sufficient amount of Pt dissolution could occur during anodic scans. The magnitude of charge difference was also significantly higher than that observed at macroscopic electrodes by Rand et. al. They observed a positive charge difference which was consistent with the amount of solvated Pt ions the detected by atomic absorption spectroscopy.¹²⁵ We believe that at nanoelectrodes the large accumulation of anodic charge will cause an increase in the Pt dissolution rate. This effect could work in synergy with the increased mass transfer inherent to nanoelectrodes to cause a larger dissolution rate.

4.4. Conclusions

In this work we have demonstrated that under potential cycling conditions Pt dissolution will occur at inlaid Pt disk nanoelectrodes effectively etching the surface forming a nanopore electrode. Although potential cycling is frequently used to clean larger electrodes, one must be careful when using potential

cycling to clean nanoelectrodes because they are unstable under these conditions and the magnitude of current can be substantially decreased depending on the cycling conditions. By observing the decrease in the diffusion-limited steady-state current before and after potential cycling and we are able to quantitatively characterize pore formation and we were able to confirm these results by SEM. We have shown that in order for a substantial decrease in the steady-state current to be observed, the upper limit of the potential cycle needs to exceed 1.0 V vs. Ag/AgCl. The Pt dissolution rate was observed to be larger than that previously reported at macroscopic electrodes. We believe that the enhancement in dissolution rate arises twofold: first from the increase in mass transport by radial diffusion to nanoelectrodes and secondly from the larger charge density observed.

4.5. Tables and Figures

Table 4-1. Pt dissolution rate as calculated from steady-state voltammetry

Disk Radius, nm	Dissolution Rate ng cm ² / cycle
2.7	33.0 ± 7.4
4.5	49.8 ± 6.1
21.0	44.3 ± 12.5
53.7	464.5 ± 60.4
143.7	789.5 ± 54.1
236.0	711.7 ± 79.1

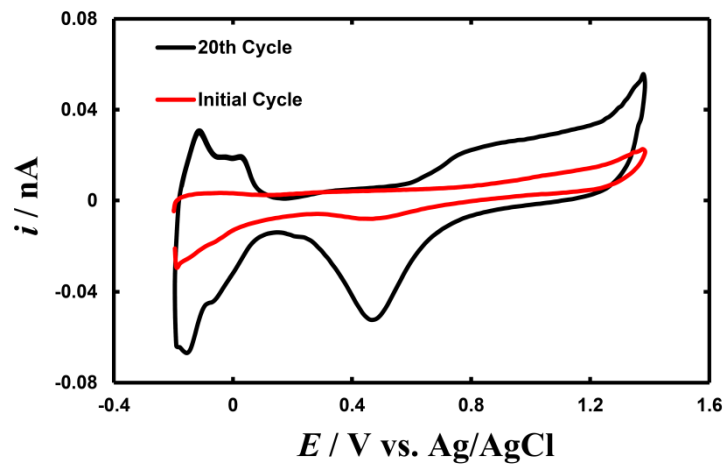


Figure 4-1. i - V response of a 40 nm Pt disk nanoelectrode in a solution of 0.5 M H_2SO_4 . The red curve is the initial CV and the black curve was obtained after potential cycling for 20 cycles at 100 mV/s.

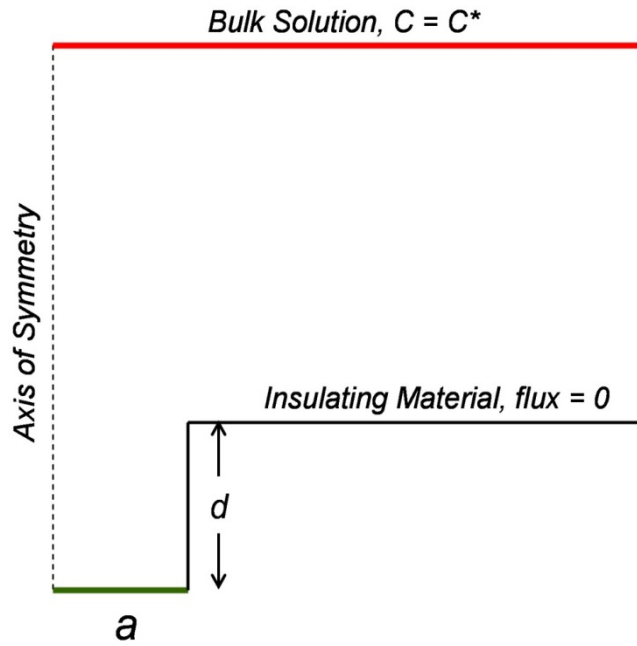


Figure 4-2. Simulation domain in Comsol for the nanopore electrode, where a is the radius of the electrode and d is the depth of the pore. Red indicates the outer solution boundary; black is the insulating glass and green is the electrode surface.

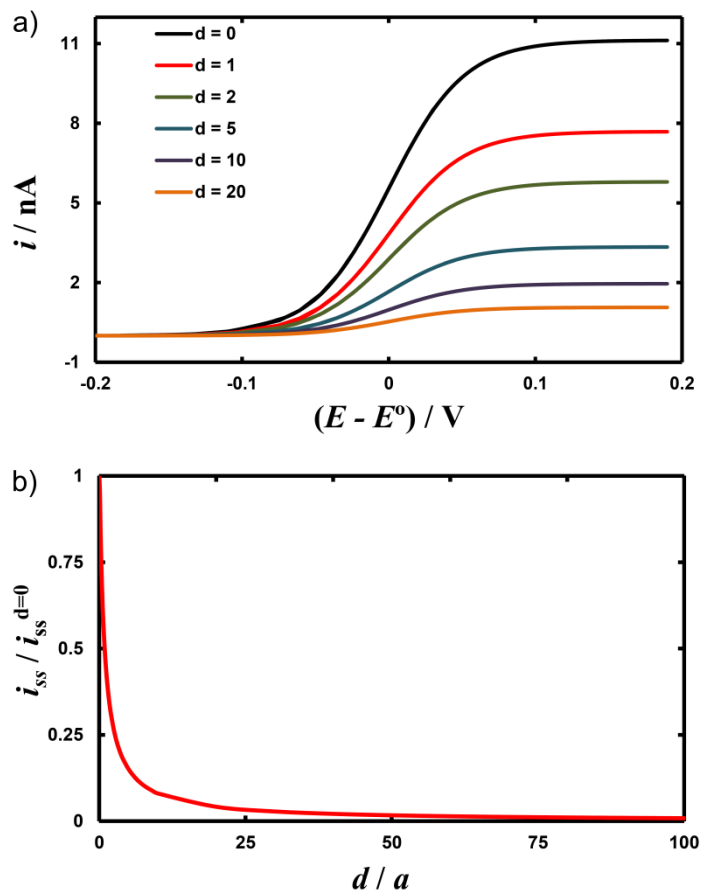


Figure 4-3. (a) Simulated steady-state i - V response of a 5 nm disk electrode before and after formation of a cylindrical nanopore of increasing depth. (b) Plot of the steady-state current normalized with respect to an inlaid disk electrode vs. the ratio of pore depth, d , to pore orifice, a .

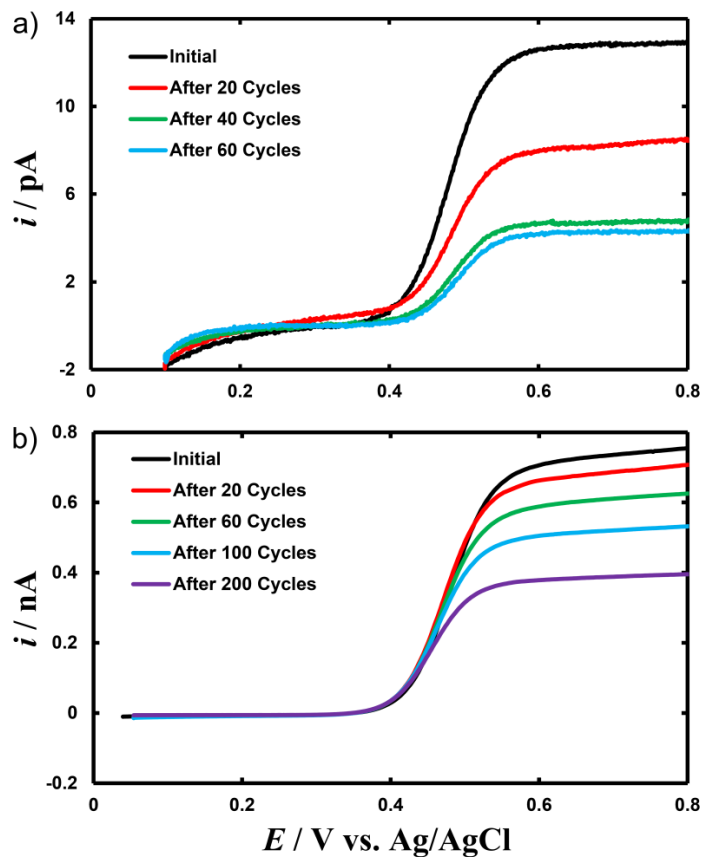


Figure 4-4. i - V responses of two Pt disk nanoelectrodes in a MeCN solution containing 5 mM Fc and 0.1 M TBAPF₆ before and after potential cycling in 0.5 M H₂SO₄ for a different number of cycles. The pore orifices are (a) 2.7 nm and (b) 150 nm. Only the forward scans are shown for clarity. The scan rate is 20 mV/s.

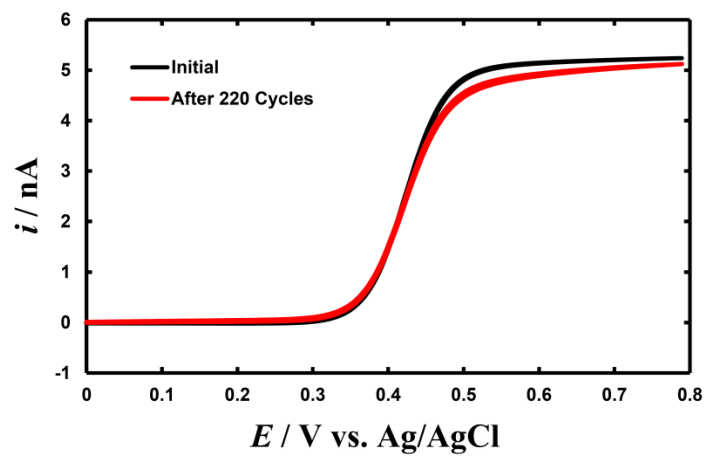


Figure 4-5. i - V response of a 1.2 μm Pt disk electrode in a MeCN solution containing 5 mM Fc and 0.1 M TBAPF₆ before (black) and after (red) potential cycling in 0.5 M H₂SO₄ for 220 cycles at a scan rate of 100 mV/s.

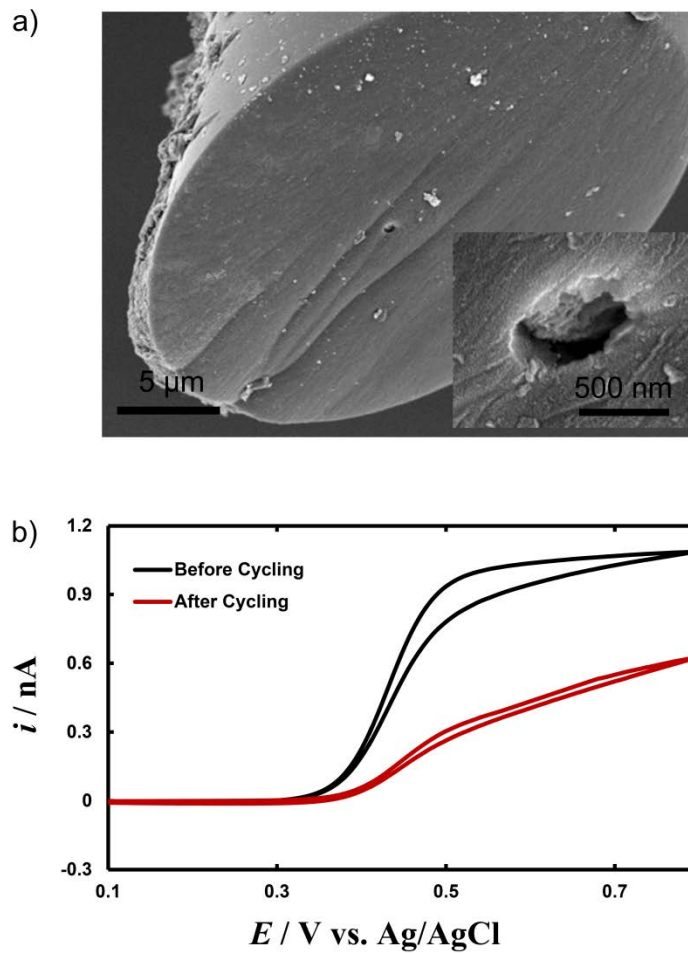


Figure 4-6. SEM image (a) and i - V response in a MeCN solution containing 5 mM Fc and 0.1 M TBAPF₆ before and after potential cycling for 100 cycles in 0.5 M H₂SO₄ from -0.2 V to +1.2 V at 100 mV/s. The approximate radius of the electrode as determined by equation 4-1 is 230 nm, and the depth of the pore is 280 nm as determined from our simulations. The inset is a zoomed in image of the surface of the recessed Pt nanoelectrode.

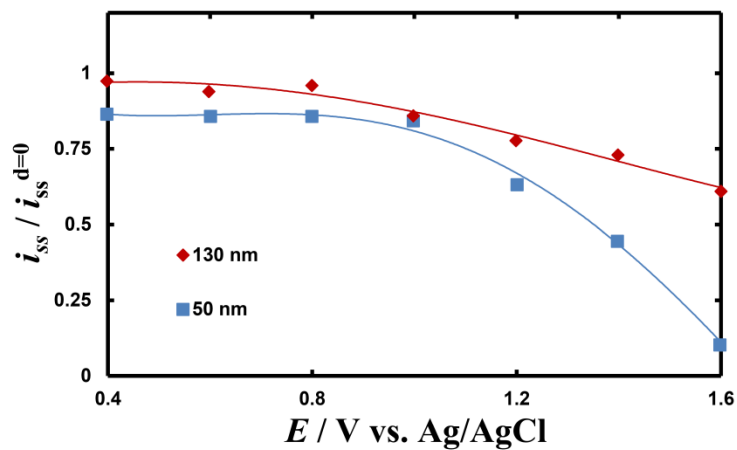


Figure 4-7. The effect of the changing the positive potential limit on steady-state voltammetry. A 50 nm (blue) and a 130 nm (red) disk nanoelectrode were cycled in a 0.5 M H_2SO_4 solution by applying a wave form between -0.2 V to a variable upper limit for 20 cycles at a scan rate of 100 mV/s. The steady-state current was obtained before and after potential cycling in a MeCN solution containing 5 mM Fc and 0.1 M $TBAPF_6$. The current magnitude was normalized with respect to the initial current and plotted against the value for the upper potential limit.

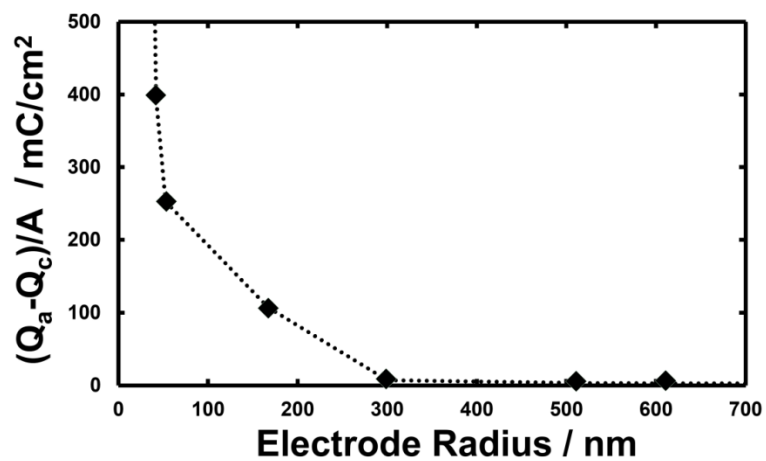


Figure 4-8. Dependence of the charge difference ($Q_a - Q_c$) on the electrode radius for Pt nanoelectrodes in a 0.5 M H₂SO₄ solution. The potential was swept from -0.2 to +1.2 V at a scan rate of 100 mV/s.

CHAPTER 5 STEADY-STATE VOLTAMMETRY OF A MICROELECTRODE IN A CLOSED BIPOLAR CELL[†]

5.1. Introduction

Bipolar electrochemistry has emerged as a useful tool for a number of important analytical applications,¹⁴⁵ such as electroanalysis,¹⁴⁶⁻¹⁵¹ separation,¹⁵² preconcentration,¹⁵³⁻¹⁵⁵ and neurochemical sensing using carbon-fiber microelectrodes.⁴¹ In addition, bipolar electrochemistry mechanisms have been utilized in industrial processes for many decades.¹⁵⁶⁻¹⁵⁷ Other recent applications of bipolar electrochemistry include synthesis and manipulation of nanomaterials,¹⁵⁸⁻¹⁶¹ and fast screening of electrocatalysts.¹⁶² A unique aspect of bipolar electrochemistry is that it uses an electrode with opposite polarity on two ends to allow for direct coupling of two different redox reactions. In a conventional two or three-electrode electrochemical cell, one focuses primarily on electrochemical reactions at the working electrode. The reference and counter electrodes function only to provide a reference potential and balance the current on the working electrode. The counter electrode is usually sufficiently large so that it does not limit the faradaic process on the working electrode. A bipolar electrochemical cell, on the other hand, involves two separate electrochemical interfaces coupled directly on a bipolar electrode (BPE). A pair of driving electrodes (usually much greater than the bipolar electrodes) supplies the voltage needed to drive the electrochemical reactions on the BPE. The overall electrochemical response of the BPE could thus be affected by both poles.

Electroanalytical studies involving BPEs have mainly been carried out using open BPEs. An open BPE cell uses a microfluidic channel to host a conductive microelectrode. A voltage bias is applied along the length of the microchannel from a pair of driving electrodes allowing two coupled electrochemical reactions to occur at each of the poles of the BPE. Open BPEs have been especially useful for performing wireless electrochemistry in a microfluidic environment.¹⁶² We¹⁶³ and others^{164,165} have recently discussed series-coupled electrochemical reactions on closed BPEs. As shown in figure 5-1a, a closed BPE cell contains two separate compartments connected via a metallic wire electrode. The electrochemical current on the closed BPE can be directly measured due to the lack of the microchannel

[†] Adapted with permission from *Anal. Chem.* 2012, 84, 8797-8804. Copyright 2012. American Chemical Society. This work was done in collaboration in Joshua P. Guerrette

and ionic current path. A closed BPE is analogous to two electrochemical cells connected in series as shown in figure 5-1b. In this configuration, the faradaic reaction occurring on the disk electrode is electrochemically coupled to the reaction on the large cylinder electrode. By our convention we refer to the pole where the limiting process occurs as the limiting pole and the other as the excess or coupling pole.

As an important application of closed bipolar setup, one can make direct electrochemical recordings on a microelectrode without the need to make direct electrical wire contact to the electrode. This is, in many cases, preferable to significantly simplify experimental procedures. For example, one can use a bipolar setup to measure electrochemical response of single nanowires and their arrays prepared in an insulating membrane. Additionally, carbon-fiber microelectrodes (CFEs),^{43,55,166} when a salt solution is used to establish electrical continuity, use a closed bipolar mechanism to detect fast changes in catecholamine concentration.

Although a microelectrode can be used in a closed bipolar setup to make direct electrode recordings, its electrochemical behavior can be quite different from its “normal” behavior in a two or three-electrode setup. For example, in a previous study we have shown that the voltammetric response of a microelectrode in a closed bipolar cell is related to the properties of the excess pole with a shift in the response as a function of the difference in formal potentials of both poles. Additionally, there is a clear dependence of the half-wave potential on the redox concentration at, and relative size of the excess pole.¹⁶³ However, in this previous report we did not reach a quantitative understanding of this relationship. In order to fully extend the potential use of BPEs for fundamental electrochemical studies as well as key bioanalytical applications it became critical to develop a more comprehensive understanding of the steady-state voltammetric response of a microelectrode in a closed bipolar setup.

In this chapter, we discuss work in our lab to elucidate the theory to quantitatively describe the steady-state voltammetry of closed bipolar microelectrodes. We focus our attention on the steady-state voltammetry of a microelectrode used as a limiting pole of a BPE and how it is affected by the processes occurring at the excess pole. We show that the voltammetric response can be readily expressed by considering the individual responses of both poles separately in conventional two or three-electrode configurations and that the wave shape depends strongly on the ratio of the limiting currents of both

individual poles. We have also provided experimental results to support our theoretical prediction. Additionally, we discuss methods to obtain a fast and nearly reversible voltammetric response from a microelectrode when used in a closed bipolar electrochemical configuration. These methods could be useful for improving performance of microscale BPEs such as CFEs routinely used for quantitative analysis in biological systems.

5.2. Theory

In order to understand the voltammetric response of a microelectrode in a closed bipolar cell, it is beneficial to first consider the steady-state response of individual poles. Under simple mass-transport control, the reversible voltammetric response of a microelectrode in a conventional two-electrode cell can be readily expressed by the following equation,⁴

$$E = E^{o'} + \frac{RT}{nF} \ln \frac{D_O}{D_R} - \frac{RT}{nF} \ln \left(\frac{i_{ss} - i}{i} \right) \quad (5-1)$$

where E and $E^{o'}$ are the applied electrode potential and the formal potential for a simple n -electron redox reaction, $R_{ed} \rightarrow O_x + ne^-$, R is the gas constant, T is the absolute temperature, n is the number of electrons transferred per redox molecule, D_R and D_O are the diffusion coefficients for the redox species R_{ed} and O_x , respectively, i is the faradaic oxidation current at voltage E , and i_{ss} is the steady-state limiting current. As previously shown in chapter 1, our experiments the microelectrodes have inlaid disk geometry, and the limiting current is given by,¹⁶⁷

$$i_{ss} = 4nFDC^*a \quad (5-2)$$

where C^* is the concentration of redox species in the bulk and a is the radius of the microelectrode. Assuming the diffusion coefficients of the R_{ed} and O_x are approximately the same, equation (5-1) is further simplified as,

$$E = E^{o'} - \frac{RT}{nF} \ln\left(\frac{i_{ss} - i}{i}\right) \quad (5-3)$$

A closed bipolar electrode allows one to couple two electrochemical reactions such that the faradaic currents on the anodic pole and the cathodic pole have the same magnitude and opposite sign due to electroneutrality. Additionally, the overall bias voltage across the BPE is equal to the difference in the applied potentials on both poles. This voltage can thus be expressed by combining the equations (5-3) for both cathodic pole and the anodic pole,

$$E = E_a - E_c = (E_a^{o'} - E_c^{o'}) + \frac{RT}{F} \left\{ \frac{1}{n_a} \ln\left(\frac{i_a}{i_{ss}^a - i_a}\right) - \frac{1}{n_c} \ln\left(\frac{i_{ss}^c - i_c}{i_c}\right) \right\} \quad (5-4)$$

where i_{ss}^a and i_{ss}^c are the limiting currents on the anodic pole and the cathodic pole, and $E_a^{o'}$ and $E_c^{o'}$ are the formal potentials for the reactions on the anodic and cathodic poles, respectively. *Here, we define the anodic current as positive and cathodic current as negative current.* Because of electroneutrality in a closed bipolar cell, the magnitude of the oxidation current on the anodic pole should be equal to that of the reduction current on the cathodic pole, or, $i = i_a = -i_c$. By further assuming both reactions are 1-electron processes, equation (5-4) becomes,

$$E = (E_a^{o'} - E_c^{o'}) + \frac{RT}{F} \left\{ \ln\left(\frac{i}{i_{ss}^a - i}\right) + \ln\left(\frac{-i}{i_{ss}^c + i}\right) \right\} \quad (5-5)$$

Equation (3-5) now shows a more complicated relationship between the total current i and the voltage across the bipolar electrode, which is closely dependent on the limiting currents of both poles. Several important conclusions can be drawn from equation (5-5). First, the limiting current of the bipolar electrode will be limited by the pole with smaller limiting current. If i_{ss}^a is smaller than $-i_{ss}^c$, the anodic pole will be

the limiting pole and the limiting current of the BPE will be i_{ss}^a . Furthermore, the $E_{1/2}$ can be derived from equation (5-5),

$$E_{1/2} = (E_a^{o'} - E_c^{o'}) - \frac{RT}{F} \ln \left(-2 \left(\frac{i_{ss}^c}{i_{ss}^a} \right) - 1 \right) \quad (5-6)$$

Equation (5-6) indicates that the $E_{1/2}$ is not only a function of the difference of the formal potentials but also related to the ratio of the limiting currents. The greater the $(-i_{ss}^c/i_{ss}^a)$, the more the i - V response would shift negatively.

Additionally, the steady-state i - V response of a microelectrode in a closed bipolar setup can be predicted from equations (5-4) and (5-5). Let us first consider a case where we have a simple $1e^-$ oxidation process, $R_{ed} \rightarrow O_x + 1e^-$, coupled to its corresponding reduction process. Since they are complimentary reactions, their formal potentials are the same. As such, equation (5-5) becomes

$$E = \frac{RT}{F} \left(\ln \left(\frac{i}{i_{ss}^a - i} \right) + \ln \left(\frac{-i}{i_{ss}^c + i} \right) \right) \quad (5-7)$$

Figure 5-2a shows three predicted i - V responses assuming the limiting current on the cathodic pole is 1, 10, and 100 times of that on the anodic pole. Also shown in figure 5-2a is the i - V response of the anodic pole in a conventional two-electrode setup. This i - V response has been generated assuming a 0-V formal potential for simplicity and easy comparison of the i - V responses. All the current in figure 5-2 has been normalized to the limiting current on the anodic pole for easy comparison.

One can immediately see that when compared to the i - V response in a conventional two-electrode setup, all bipolar i - V responses have similar sigmoidal shape. However, the bipolar responses clearly show a *slower* current increase with voltage. The 1:1 current ratio gives the slowest current increase and requires a higher applied voltage to reach steady-state. We believe that this apparent wave broadening or slower i - V response is solely due to additional energy (or voltage) requirement to drive the

second faradaic reaction on the excess pole. The higher the cathodic limiting current, the faster the current increases with voltage. We can anticipate that when the cathodic steady-state limiting current is much higher than that on the anodic pole, the overall i - V response would resume the reversible shape of the CV in the conventional two-electrode setup. Figure 5-2a also shows a clear negative shift of the $E_{1/2}$ of the bipolar response as the ratio of the limiting currents increases, which is in agreement with our previous observation.¹⁶³

In order to more quantitatively understand the change in the shape of the bipolar i - V response, we have generated the E vs. $\log[i/(i_{ss}-i)]$ plots of the bipolar electrode and that of the conventional setup. Often times a plot of E vs. $\log[i/(i_{ss}-i)]$ is prepared to show whether a process is reversible or not on a microelectrode.⁴ If this plot is linear with a slope equal to $59.2/n$ mV the process is said to be reversible. For a non-linear plot with a slope greater than this the system is typically considered quasireversible or irreversible. The conventional direct connect configuration in figure 5-2b shows a linear relationship with a slope of 59.2 mV as expected. On the other hand, for the bipolar setup, a linear relationship is obtained only when both poles have the same limiting current, in which case, the slope of the curve is 118 mV. When the cathodic pole has a greater limiting current than the anodic pole, a nonlinear relationship is obtained between E and the $\log[i/(i_{ss}-i)]$ as predicted from equations (5-4) and (5-5). The slope of the line at $E_{1/2}$ is a function of the ratio, $-i_{ss}^c/i_{ss}^a$, and is between 59 mV and 118 mV. We can anticipate that when this ratio goes to infinity, the slope of the line would approach 59 mV at half-wave potential.

This increased slope may be mistakenly understood to be an indication of irreversibility. Instead it is the result of directly coupling two reversible processes and is not itself indicative of any kinetic limitations. An alternative approach to determine the reversibility of an electrochemical process is to apply the Tomeš criterion of reversibility which states that for a reversible charge transfer the difference in quartile potentials, $|E_{3/4} - E_{1/4}| = 56.4/n$ mV, where $E_{3/4}$ and $E_{1/4}$ refer to the three-quarter and one-quarter wave potentials respectively.⁴ From Equation 5-5 we can derive the modified Tomeš criterion of reversibility for two coupled electrochemical reactions at a BPE to be:

$$|E_{3/4} - E_{1/4}| = \frac{RT}{F} \ln \left(27 \left(\frac{i_{ss}^c + 0.25i_{ss}^a}{i_{ss}^c + 0.75i_{ss}^a} \right) \right) \quad (5-8)$$

This will allow for a more complete description of processes occurring at a microelectrode when used in a closed bipolar cell configuration as a tool for electrochemical analysis. By applying this criterion to the simulated results, values of 113 mV, 86 mV and 85 mV for 1:1, 10:1 and 100:1 are calculated respectively.

5.3. Results and Discussion

5.3.1. Steady-State Voltammetry of a Microelectrode in a Closed Bipolar Cell

Our theory has shown that when a microelectrode is used as the limiting pole in a closed bipolar setup, it would show a sigmoidal shape current-voltage response. Compared to its voltammetric response in a conventional two-electrode setup, the bipolar response has the same limiting current. However, the $E_{1/2}$ and the shape of the voltammetric response are strongly dependent on the property of the excess pole. In general, the bipolar response is slower than the response in a conventional two-electrode cell as evident by the broadening of the wave. The distortion is however unrelated to electron-transfer kinetics and is simply due to electrochemical coupling in a bipolar electrode cell.

Figure 5-3 displays the voltammetric responses of a 25- μm -diameter Au disk electrode in an aqueous solution of 1 mM ferrocyanide and 3 M KCl in three different setups. The black curve is the i - V response of the electrode in a two-electrode cell. A nice sigmoidal shape response is obtained for the oxidation of $\text{Fe}(\text{CN})_6^{4-}$. The limiting current is 3.69 nA in good agreement with the prediction of 3.66 nA from equation 5-2. The blue, red, and green curves are i - V responses recorded from the same electrode in a closed bipolar cell. A second Au disk electrode of the same size is used as a cathodic pole. In this case, the cathodic pole is placed in an aqueous solution containing 1 mM ferricyanide and 3 M KCl (blue curve). Since $\text{Fe}(\text{CN})_6^{3-}$ has the same concentration and roughly the same diffusion coefficient as $\text{Fe}(\text{CN})_6^{4-}$, the cathodic pole would yield a reduction limiting current equal to the oxidation limiting current on the anodic Au electrode (i.e., the electrode of interest), or, $-i_{ss}^c/i_{ss}^a = 1$. One can clearly see that the i - V response (blue) has roughly the same limiting current as that recorded in the two-electrode setup (black). However, the bipolar response is clearly slower than that of the two-electrode setup. This result is in good agreement with prediction from figure 5-2a. The slower i - V response in the bipolar setup can be

qualitatively understood by the additional energy requirement to drive the electrochemical process on the cathodic pole. The higher the redox concentration in the cathodic pole, the less voltage needed to drive the same amount of current on the cathodic pole. In a second experiment, the cathodic pole is placed in a 10 mM $\text{Fe}(\text{CN})_6^{3-}$ solution (red curve). This would correspond to a situation in which the cathodic limiting current is roughly 10 times greater than the anodic pole, or $-i_{ss}^c/i_{ss}^a = 10$. Compared to the blue curve, the red i - V response indeed becomes much faster due to the increase in the cathodic limiting current. An even stronger effect is observed when the cathodic Au electrode is placed in a 100 mM $\text{Fe}(\text{CN})_6^{3-}$ solution (green curve). Additionally, there is a clear negative shift in the $E_{1/2}$ as the concentration of $\text{Fe}(\text{CN})_6^{3-}$ is increased, which is in good agreement with equation 5-6 and results in figure 5-2.

We have plotted the voltage across the bipolar electrode with respect to the logarithm of the limiting current ($\log[i/(i_{ss}-i)]$), as shown in figure 5-3b. Also shown is the same plot for the electrode in the two-electrode setup (the black curve). The two-electrode setup yields a linear curve with a slope of 59.3 mV as expected indicating reversible response. Conversely, the blue curve is the plot for the same electrode in the bipolar setup with $-i_{ss}^c/i_{ss}^a = 1$. The blue curve is also found to be linear with a slope of 113.5 mV in agreement with prediction in figure 5-2b. The red and green curves are the plots of the same electrode in the bipolar setup corresponding to when $-i_{ss}^c/i_{ss}^a$ is ~ 10 and ~ 100 , respectively. These are nonlinear plots and the slopes at $E_{1/2}$ are 93.9 mV and 83.3 mV. The values obtained for $|E_{3/4} - E_{1/4}|$ are shown in table 1 and are in agreement with the derived modified Tomeš criterion of reversibility. In summary, our experimental results have confirmed the theoretical prediction.

Both theory and experimental results have revealed that when a microelectrode is used in a bipolar setup, its voltammetric response may change significantly depending on the properties of two coupling poles. Most significantly, a microelectrode shows a slower i - V response in a bipolar setup than its corresponding response in a conventional two or three-electrode cell. This sluggish voltammetric behavior is a result of electrochemical coupling and extra energy requirement to drive complimentary current at the other pole. A greater limiting current on the coupling pole could lower this energy requirement. Therefore, it could likely facilitate the observation of a faster voltammetric response.

5.3.2. Is “Reversible” Voltammetric Behavior Obtainable in a Bipolar Cell?

A bipolar mechanism can greatly simplify experimental setup in certain experiments involving ultramicroelectrodes and nanoelectrodes by eliminating direct wire contacts to the electrodes. For example, carbon-fiber microelectrodes use a salt solution to establish electrical contact which makes it convenient to quickly change electrodes during single-cell measurements. However, the electrochemical coupling between the two poles could complicate the analysis of the voltammetric behavior of a micro- or nanoelectrode by slowing down its i - V response. Although the limiting current is unlikely affected, the shape of the voltammetric response could depend strongly on the condition of the coupling pole. This could have significant impacts for electroanalytical applications where the shape of the voltammetric response is important. For example, the shape of the steady-state voltammogram of very small nanoelectrodes can be used to analyze heterogeneous electron-transfer kinetics.^{18,57} Additionally, the sluggish voltammetric response of microelectrodes in a bipolar setup may cause increased uncertainty in certain electroanalytical sensing experiments, such as detection of electroactive neurotransmitters in single-cell measurements. It is reasonable to believe that a faster voltammetric response would be preferable in almost all electroanalytical experiments involving the use of microelectrodes and nanoelectrodes and a bipolar mechanism to establish electrical contact.

It is thus important to explore possible methods to obtain a nearly “reversible” voltammetric response in a closed bipolar setup. Because the slow voltammetric response is a result of additional energy requirement from the coupling pole, we believe that a greater limiting current at the coupling pole could facilitate the observation of a nearly “reversible” voltammetric response. Since the limiting current on the coupling pole depends on the concentration of the redox species and electrode size and both factors are relatively easy to adjust, we set out experiments to obtain fast voltammetric responses by changing redox concentrations and greatly increasing the size of the excess pole.

Figure 5-4 shows a series of i - V responses of a 25- μ m-diameter Pt disk microelectrode in a closed bipolar setup in acetonitrile containing 50 μ M Fc and 0.1 M TBAPF₆. A second 25- μ m-diameter Pt disk electrode is used as the excess cathodic pole and is placed in an aqueous solution containing 3 M KCl and Fe(CN)₆³⁻ of various concentrations. This electrochemical cell configuration is shown in figure 5-1b. Here, the oxidation of Fc on the first Pt microelectrode is coupled to the Fe(CN)₆³⁻ reduction on the

cathodic pole, which also limits the overall i - V response of the BPE. All the i - V responses shown in figure 5-4 have nearly the same limiting current due to Fc oxidation. The measured limiting current agrees well with prediction according to equation 5-2.

A general trend is observed in figure 5-4: the Fc oxidation current increases much more quickly with voltage as the concentration of $\text{Fe}(\text{CN})_6^{3-}$ increases. In the absence of $\text{Fe}(\text{CN})_6^{3-}$, the oxidation of Fc is likely coupled to the reduction of soluble oxygen on the cathodic pole. A much slower i - V response is observed due to a smaller reduction current of oxygen. The oxidation of Fc becomes much faster in the presence of $\text{Fe}(\text{CN})_6^{3-}$. The higher the $\text{Fe}(\text{CN})_6^{3-}$ concentration, the faster the current increases with voltage. Because the reduction current of $\text{Fe}(\text{CN})_6^{3-}$ is roughly proportional to its concentration, the observed concentration effect on the i - V response is analogous to the effect of current ratio of two poles.

It is advantageous in a closed bipolar setup to use a high redox concentration on the coupling pole. However, the redox concentration is often limited in many conditions. For example, the concentration of saturated $\text{Fe}(\text{CN})_6^{3-}$ is ~ 1.4 M at room temperature.¹⁶⁸ Since the limiting current on the coupling pole is also directly related to its size, it is in many conditions convenient to use a large coupling pole to obtain a fast voltammetric response on the limiting pole.

Figure 5-5 shows a series of i - V responses of a 25- μm -diameter Pt disk microelectrode in acetonitrile containing 0.5 mM Fc and 0.1 M TBAPF₆. The Pt disk electrode has been coupled to a 25- μm -diameter 2-mm-length Pt wire electrode used as an excess pole. The Pt microwire was placed in three different aqueous solutions of 5 mM $\text{Fe}(\text{CN})_6^{3-}$, 5 mM $\text{Ru}(\text{NH}_3)_6^{3+}$, and oxygen saturated 0.1 M NaOH. The blue curve is the i - V response of the same 25- μm -diameter Pt disk electrode in 0.5 mM Fc in a two-electrode setup for comparison. One can see that all i - V responses in figure 5-5 show very similar sigmoidal shape except for a noticeable shift in their $E_{1/2}$. The i - V response shows the minimum shift in position when the disk electrode is coupled to the reduction of oxygen on the Pt wire. The greatest $E_{1/2}$ shift is observed when the disk electrode is coupled to the reduction of $\text{Fe}(\text{CN})_6^{3-}$. The shift in $E_{1/2}$ can be qualitatively explained by considering the formal potentials of the redox species on both poles and the effect of the limiting current ratio. The formal potential of Fc oxidation is ~ 0.55 vs. NHE.⁴ When the disk electrode is coupled to oxygen reduction with a formal potential of ~ -0.065 V vs. NHE,¹⁶⁹ an $E_{1/2}$ around $+0.61$ V is anticipated. The purple i - V response shows an $E_{1/2}$ around 0.4 V, a negative shift of 0.21 V,

which is caused by the large limiting current of oxygen reduction. Similar potential shifts have been observed in figures 5-2 and 5-3. Similarly, the reduction of $\text{Fe}(\text{CN})_6^{3-}$ has a formal potential of 0.36 V vs. NHE,⁴ which would result in an $E_{1/2}$ of the bipolar response around 0.2 V. It is observed in figure 5-5a that the $E_{1/2}$ is around 0 V, a negative shift of ~ 0.2 V again caused by the large ratio of the limiting current. The reduction of $\text{Ru}(\text{NH}_3)_6^{3+}$ has a formal potential of ~ 0.1 V vs. NHE,⁴ which gives a predicted $E_{1/2}$ around 0.45 V. However, the observed $E_{1/2}$ is around 0.2 V due to a negative shift of ~ 0.25 V.

Importantly, a quick examination of figure 5-5a reveals that all i - V responses are very similar in overall shape. Figure 5-5b shows all four curves superimposed on each other. There is hardly any differences observable between the two-electrode response and those of the bipolar setups in $\text{Fe}(\text{CN})_6^{3-}$ and $\text{Ru}(\text{NH}_3)_6^{3+}$. To quantitatively describe potential differences in wave shapes, the wave slope and $|E_{3/4} - E_{1/4}|$ are shown in table 2. The calculated values show a slight increase in wave slope and $|E_{3/4} - E_{1/4}|$ for the bipolar configurations, as expected. The fact that all i - V responses have similar shapes and no major distortion is observed in the bipolar setups could be due to the significantly larger faradic current on the Pt wire electrode. A CV response of the Pt wire electrode in 5 mM $\text{Fe}(\text{CN})_6^{3-}$ (not shown) shows a reduction current of ~ 2500 nA, which is roughly 275 times greater than the limiting current on the Pt disk. The results shown in figure 5-5 are encouraging because it indicates that one can obtain nearly reversible i - V response even in a bipolar setup when a microelectrode is coupled to a large excess pole. This is an important result because it implies that when a bipolar setup is used in electroanalytical applications, one should use a large coupler electrode in order to more accurately examine the voltammetric properties of a microelectrode or to detect quick changes in analyte concentrations.

Due to the wide usage of carbon-based microelectrodes in bioanalytical sensing, it is important to verify the above conclusions with CFEs. As shown in the figure 5-6, similar observations have been obtained with carbon-fiber microelectrodes. Figure 5-6a is a series of i - V responses collected from a closed bipolar cell consisting of a 5- μm -diameter disk CFE in a 50 μM Fc solution containing 0.1 M TBAPF₆ and a CFE with an exposed 5- μm -diameter, 2-mm-length carbon fiber in varying reduction reactions. The i - V response of the same disk CFE in a two-electrode cell is given as the blue curve, in

which a direct electrical contact was made to the fiber from inside the glass capillary using silver epoxy. Figure 5-6b is the overlaid i - V responses after correcting their $E_{1/2}$ shifts. One can see that all the i - V responses in the bipolar setup have similar shapes and limiting currents, which are nearly indistinguishable from the response in the two-electrode setup.

In addition to using Fc oxidation as a model reaction, we have studied the oxidation of dopamine on a 5- μ m-diameter CFE. Figure 5-6c shows a series of i - V responses collected on a 5- μ m-diameter CFE in 100 μ M dopamine when coupled to the reduction of several different redox species including $\text{Fe}(\text{CN})_6^{3-}$, $\text{Ru}(\text{NH}_3)_6^{3+}$, saturated oxygen in 0.1 M NaOH, and soluble oxygen in 3 M KCl. The resulting i - V responses all show very similar shapes and are almost indistinguishable from the one collected in a two-electrode setup on the same electrode, as shown in figures 5-6c and 5-6d. The wave slope and $|E_{3/4} - E_{1/4}|$ for the curves in figures 5-6a and 5-6c are shown in table 3 and demonstrate little variance between bipolar configurations. The results shown in figure 5-6 have further confirmed that when a microelectrode is used in a bipolar setup, a large coupler electrode is needed to obtain nearly reversible voltammetric responses.

5.4. Conclusion

In this chapter we have discussed the theory and corresponding experiments to more fully understand the steady-state voltammetric response of a microelectrode used in a closed bipolar setup. Our theory shows the voltammetric response is likely distorted when a microelectrode is used in a bipolar setup and is often slower than that in a conventional two-electrode setup. The slower response in the bipolar setup is likely due to additional energy requirement to drive the faradaic reaction at the coupling pole. The shape of the bipolar voltammetric response depends on the ratio of limiting currents on both poles. A large faradic current on the excess coupling pole facilitates the observation of a fast voltammetric response. This can be realized by increasing the redox concentration and the electrode size on the excess coupling pole.

5.5. Tables and Figures

Table 5-1. A comparison of the wave parameters obtained from the predicted i - V curves in Fig. 1 and that measured from experimental i - V curves in Fig. 2 for different $-i_{ss}^c/i_{ss}^a$ ratios. The corresponding wave parameters for the two-electrode cell are also listed for comparison.

$-i_{ss}^c/i_{ss}^a$	Wave Slope (mV)	Wave Slope _{calc} (mV)	$ E_{3/4}-E_{1/4} $ (mV)	$ E_{3/4}-E_{1/4} _{calc}$ (mV)
Two-electrode	59.3	59.2	56	56.4
1:1	113.5	118	111	113
10:1	93.9	86	87	86
100:1	83.3	85	79	85

Table 5-2. The wave parameters obtained from the i - V curves in Fig. 4 for Fc oxidation at a Pt BPE. The corresponding wave parameters for the two-electrode cell are also listed for comparison.

Coupling redox	Wave Slope (mV)	$ E_{3/4}-E_{1/4} $ (mV)
Two-electrode	68.1	65
$K_3Fe(CN)_6$	89.1	85
$Ru(NH_3)_6Cl_3$	84.9	81
Oxygen	75.5	72

Table 5-3. The wave parameters obtained from the i - V curves in Fig. 5 for Fc oxidation and dopamine oxidation at a carbon fiber microelectrode filled with different redox species. The corresponding wave parameters for the two-electrode cells are also listed for comparison.

Redox species (limiting pole)	Redox species (coupling pole)	Wave Slope (mV)	$ E_{3/4}-E_{1/4} $ (mV)
Ferrocene	Two-electrode	60.8	59
	$K_3Fe(CN)_6$	69.2	66
	$Ru(NH_3)_6Cl_3$	68.1	65
	Oxygen	70.8	67
	KCl	68.1	65
Dopamine	Two-electrode	78.6	74
	$K_3Fe(CN)_6$	83.8	80
	$Ru(NH_3)_6Cl_3$	78.6	75
	Oxygen	89.1	85
	KCl	83.8	80

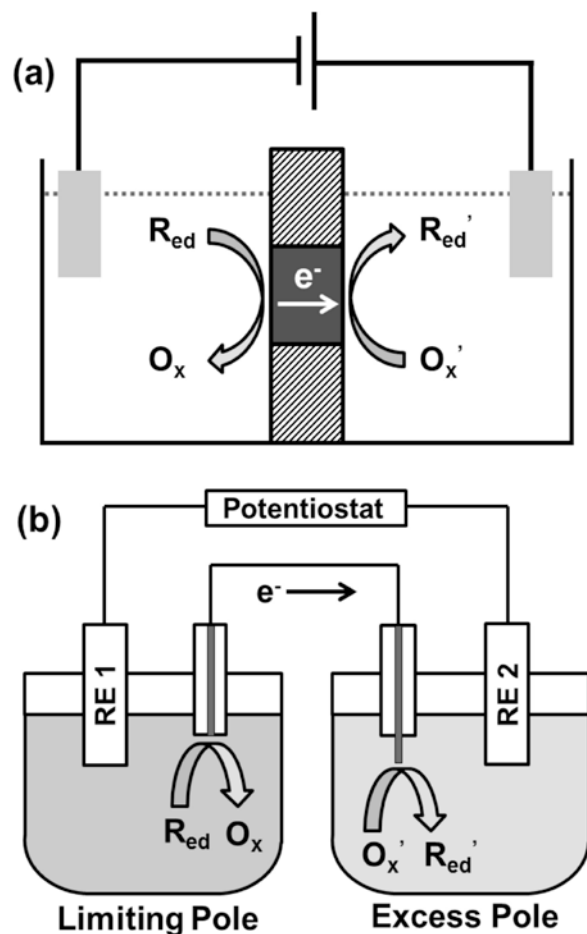


Figure 5-1. (a) A schematic of a closed bipolar electrode cell. (b) A schematic of a series-coupled bipolar cell containing a disk microelectrode in one compartment and a cylindrical microelectrode in the other compartment. The working electrode lead from the potentiostat is connected to reference electrode 2 (RE2) and the reference lead to reference electrode 1 (RE1). The anodic pole is limiting and the cathodic pole is in excess.

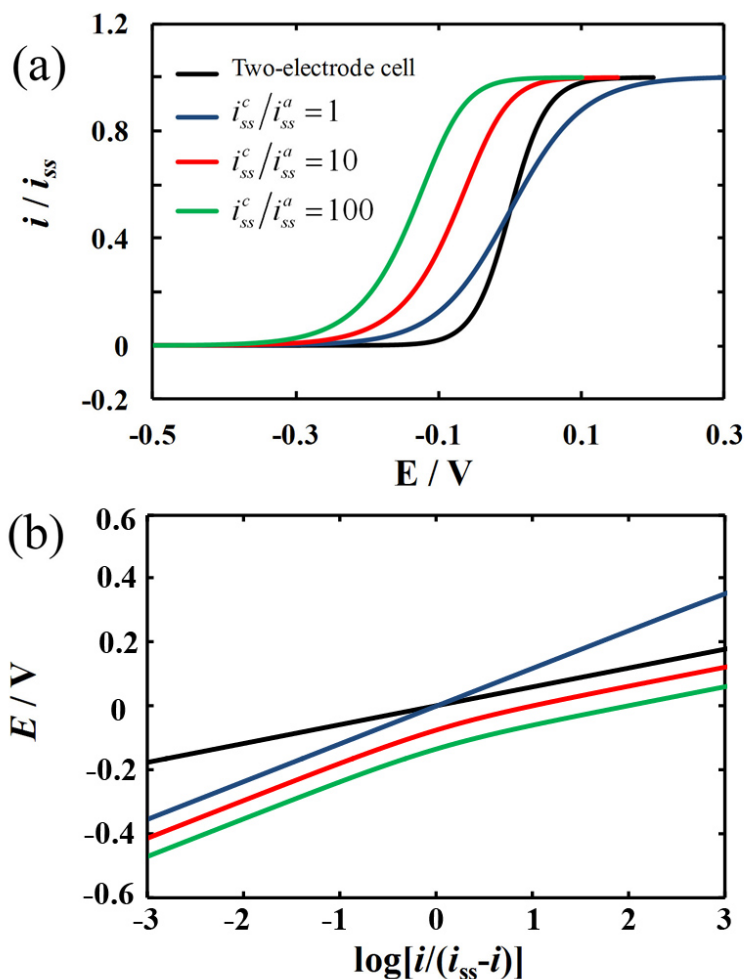


Figure 5-2. (a) Theoretical i - V responses of a microelectrode in a two-electrode cell (black) and in a closed bipolar electrode setup when coupled to a cathodic pole. The blue, red, and green curves correspond to when the ratio of limiting currents, $-i_{ss}^c/i_{ss}^a$, are 1, 10, and 100, respectively. The formal potentials of the oxidation reaction on the microelectrode and the cathodic reaction on the coupling electrode have been assumed to be 0 V. The voltage for the bipolar setup is the voltage applied across the bipolar electrode and the voltage for the two-electrode setup is the voltage applied on the microelectrode with respect to the reference electrode. (b) A plot of the voltage applied across the bipolar electrode (for the blue, red, and green curves) as a function of the $\log[i/(i_{ss}-i)]$ for the i - E curves given in (a). Only voltages between $E_{1/4}$ and $E_{3/4}$ are plotted in (b).

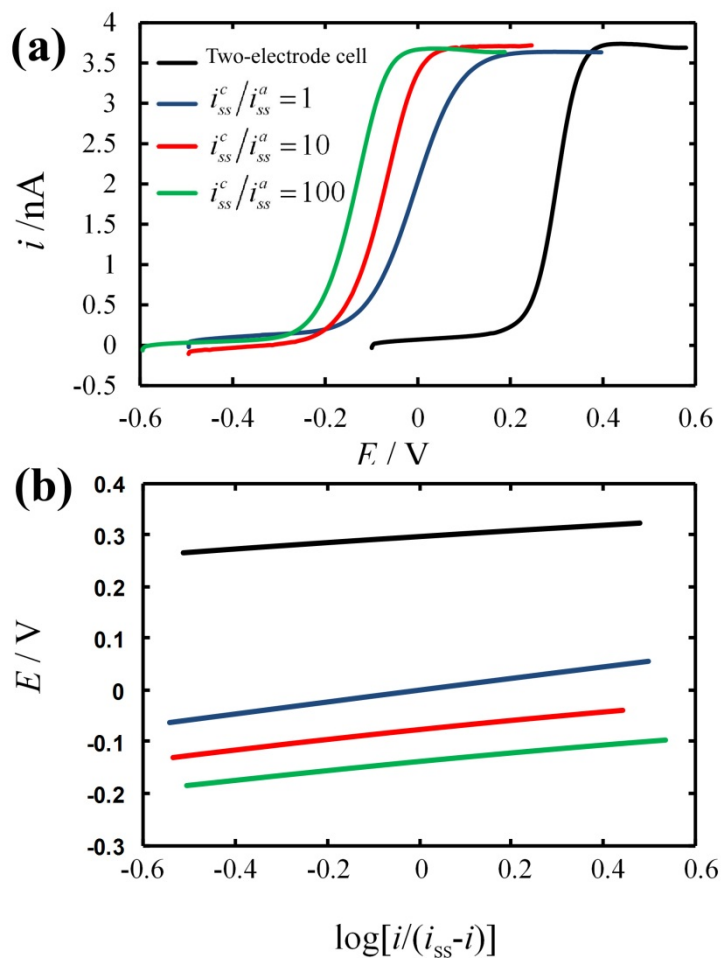


Figure 5-3. a) The i - V responses of a 25- μ m-diameter Au disk microelectrode in a solution of 1 mM $\text{Fe}(\text{CN})_6^{4-}$ and 3 M KCl in a two-electrode set-up (black curve) and closed bipolar cell when coupled to a second 25- μ m-diameter Au disk electrode as a cathodic pole. The cathodic pole was placed in a 3 M KCl solution containing $\text{Fe}(\text{CN})_6^{3-}$ of various concentrations: 1 mM (blue curve), 10 mM (red curve), and 100 mM (green curve). The scan rate was 20 mV/s for all scans. The voltage for the bipolar setup is the voltage applied across the bipolar electrode as illustrated in figure 5-1b and the voltage for the two-electrode setup is the voltage applied on the microelectrode with respect to a Ag/AgCl reference electrode. (b) A plot of the voltage applied across the bipolar electrode (for the blue, red, and green curves) as a function of the $\log[i/(i_{ss}-i)]$ for the i - E curves given in (a). Only voltages between $E_{1/4}$ and $E_{3/4}$ are plotted in (b).

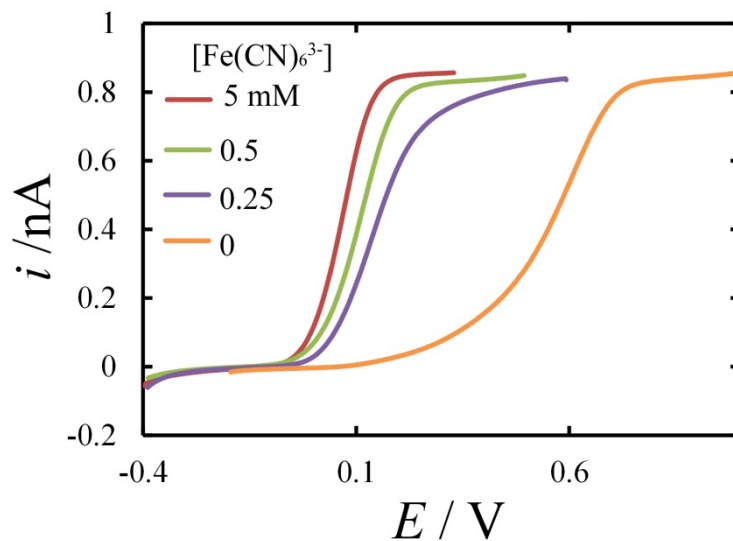


Figure 5-4. The i - V responses of a 25- μm -diameter Pt disk electrode in acetonitrile containing 50 μM Fc and 0.1 M TBAPF₆. The oxidation of Fc was coupled to the reduction of ferricyanide of varying concentrations in a 3 M KCl solution on another 25- μm -diameter Pt microelectrode.

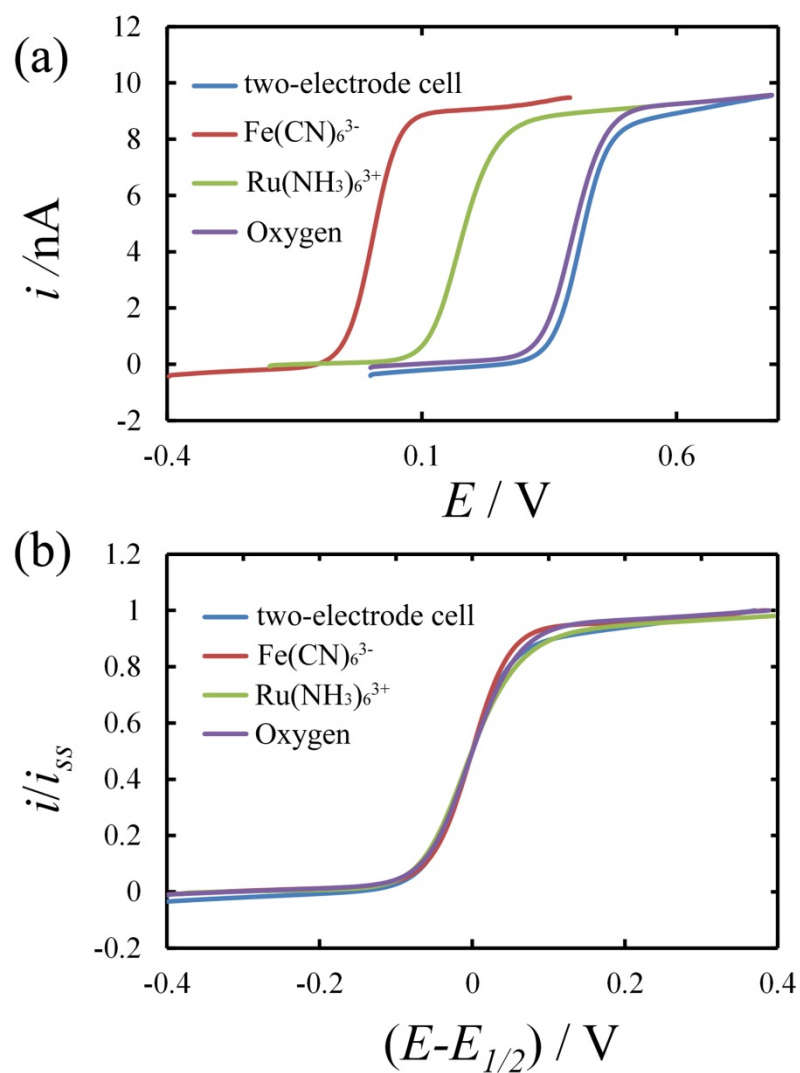


Figure 5-5. (a) The i - V responses of a 25- μ m-diameter Pt disk electrode in acetonitrile containing 0.5 mM Fc and 0.1 M TBAPF₆. The oxidation of Fc was coupled to the reduction of three different redox species, 5 mM Fe(CN)₆³⁻, 5 mM Ru(NH₃)₆³⁺, and saturated oxygen in 0.1M NaOH on a 25- μ m-diameter, 2-mm-length Pt wire. The i - V response of the same electrode in a two-electrode cell is given as the blue curve for comparison. (b) An overlay plot of the normalized CVs in (a) highlighting the change in wave shape.

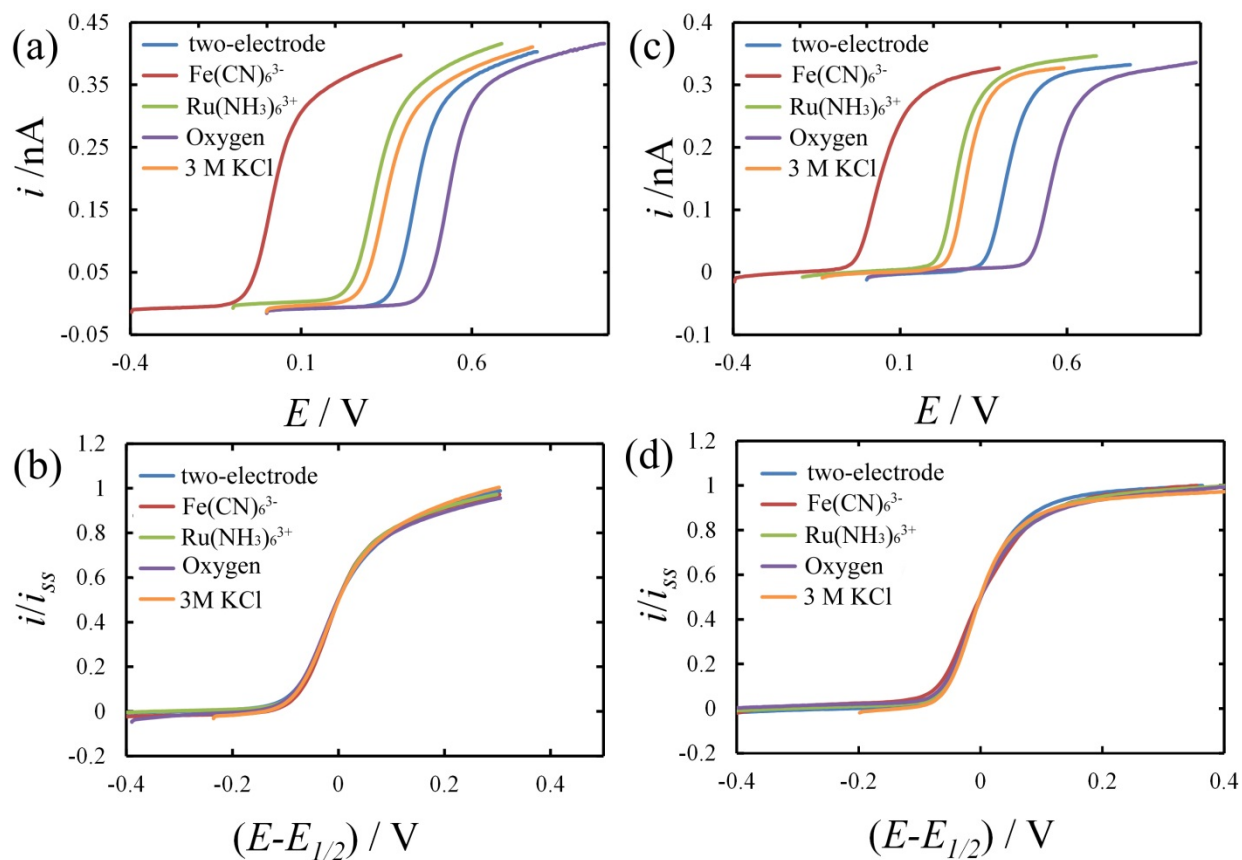


Figure 5-6. The i - V responses of a 5- μm -diameter carbon-fiber disk electrode in a solution of (a) 50 μM Fc 0.1M TBAPF₆ and (c) 100 μM dopamine coupled to a 5- μm -diameter, 2-mm-length carbon fiber in a solution containing different redox molecules including 5 mM $\text{Fe}(\text{CN})_6^{3-}$, 5 mM $\text{Ru}(\text{NH}_3)_6^{3+}$, saturated oxygen in 0.1M NaOH, and 3 M KCl. The CV response of the same disk electrode in a two-electrode cell is given for comparison. An overlay plot of the normalized CVs is given in (b) for Fc and (d) for dopamine to highlight the change in wave shape.

CHAPTER 6 USING BIPOLAR ELECTROCHEMISTRY TO ENHANCE DETECTION OF EXOCYTOSIS FROM PC 12 CELLS WITH CARBON FIBER MICROELECTRODES[‡]

6.1. Introduction

Carbon fiber microelectrodes (CFE) have emerged as the premier tool for electrochemical analysis to study exocytosis and the electrochemistry of biological systems^{40,41,170}. Their millisecond temporal resolution, high spatial resolution from their small size, biocompatibility, and low capacitance current make them ideal probes to study the dynamics of neurotransmission. First employed by Wightman¹⁷¹ to study catecholamine release from chromaffin cells, CFEs are widely used in constant potential amperometry to gain further insight into the neurotransmission process and quantitatively describe exocytosis in a variety of cells types such as intact neurons⁴⁸⁻⁵⁰, primary cell cultures⁵¹, immortalized cell lines^{44,46}, and brain slices⁴⁷. This is achieved by measuring current transients at single cells from individual exocytotic events by way of fusion of intracellular vesicles with the cell membrane and subsequent release of vesicular contents upon stimulation¹⁷².

Although CFEs have many inherent advantages for neurochemical studies, they are not without fault. As sensing occurs, biomolecules and oxidative products can adsorb to the surface of the CFE, fouling the electrode surface and significantly decreasing the electrode's selectivity and sensitivity. To overcome this, much research has been conducted to modify the surface of the carbon fiber. For instance, Adams et. al has shown there is a significant increase in sensing activity when the surface of a CFE is modified with a network of gold nanoparticles⁵⁷. A variety of other materials have been used in surface modifications, including photoresist¹⁷³, Nafion¹⁷⁴⁻¹⁷⁶, single-walled carbon nanotubes^{177,178}, 4-sulfobenzendiazonium tetrafluoroborate¹⁷⁹, and hydrolyzed cellulose acetate¹⁸⁰. With every modification, there are disadvantages and one must make sure the improved sensitivity does not sacrifice key attributes like temporal resolution or response time²⁸. Additionally, it has been shown that the effects of surface absorption can be offset by oxidative etching to renew the CFE surface¹⁸¹. Alterations to the size¹⁸² and shape of the electrode are another common approach to improve detection and methods

[‡] Portions of this chapter are adapted from a manuscript in preparation to be submitted to Analytical Chemistry.

using nanoscale CFEs¹⁸³ and microelectrode arrays¹⁸⁴ have all been employed. Although these methods do demonstrate technological advancement, a literature search yields little results on studies that investigate the role of the interior carbon fiber in analysis, specifically how the electrochemistry on the interior carbon fiber can affect the observations being made with the electrochemical sensors.

A typical CFE consists of an individual carbon fiber that has been sealed inside a glass capillary and pulled into a micropipette⁴². In early work with CFEs, electrical contact was made by back-filling the capillary with mercury¹. Because of concerns regarding the toxicity of mercury and its practicality, other methods have been developed to establish electrical contact with the interior carbon fiber. These methods include back-filling the capillary with colloidal graphite^{42,182} or an aqueous solution containing an electrolyte such as potassium chloride^{43,46} or potassium acetate^{55,185}. Back-filling the electrode with an electrolyte solution has emerged as the popular choice because it allows for simple and rapid exchange of CFEs during experimentation. In this method, electrical contact is made indirectly with the carbon fiber and it is assumed that the electron transfer on the interior carbon fiber is sufficiently high enough that any observed electrochemical process is limited solely by the kinetics and mass transfer occurring at the exterior CFE disk surface. We show in this report that this assumption is not entirely valid and that distortions in amperometric data can arise when the electrochemistry on the interior carbon is ignored. By indirectly establishing electrical contact via an electrolyte solution, a CFE will behave as a closed bipolar electrode (BPE)¹⁶³ and the electron transfer is facilitated by electrochemically coupling reactions on the both ends of the carbon fiber¹⁸⁶.

A closed BPE is analogous to two electrical cells connected in series and consists of two separate compartments connected via a metallic wire¹⁶⁴. The voltage bias is applied by two driving electrodes in the external solution of each compartment and current is restricted to only flow directly through the metallic wire connecting the two cells. The applied potential polarizes the metallic wire and faradaic processes occur and are observed on both poles. The schematic shown in Figure 1a illustrates the bipolar nature of a CFE back-filled with an electrolyte solution. As the driving voltage is applied between two Ag/AgCl reference electrodes a molecule of interest – in this case dopamine – will be oxidized at the disk surface. This oxidization is electrochemically coupled to a reduction reaction which occurs at the

interior carbon fiber. By convention, we refer to the outer disk as the anodic pole or sensing electrode and the interior carbon fiber as the cathodic pole.

In this work, we investigate the effect that a bipolar system has on the amperometric detection of dopamine from PC12 cells via constant potential amperometry. We compare how different methods to establish electrical continuity in a traditional CFE affect peak characteristics observed from current transients. From this analysis we can observe the limitations imposed by electrochemical coupling and how the size and shape of amperometric peaks are affected. We show that although the distribution of vesicular content observed and calculated from peak parameters are similar for different bipolar configurations, their kinetic peak parameters differ significantly. The differences in kinetic parameters demonstrate that the method for establishing electrical contact in a CFE matters and cannot be ignored. By applying an understanding of bipolar electrochemistry, kinetic limitations from the cathodic reaction on the interior carbon fiber can be overcome. We will show that by simply changing the electrochemistry at the cathodic pole, the electrochemical behavior can be improved and brought to a level near that of directly connecting to the carbon fiber. Furthermore, we also demonstrate that bipolar electrochemistry allows for meaningful detection at lower overpotentials.

6.2. Experimental Section

6.2.1. Cell Culture

PC12 cells were purchased from the American Type Culture Collection (Manassas, VA) and maintained as previously described^{187,188}. In short, cells were grown in cell growth media consisting of phenol red-free RPMI 1640 (Mediatech) with 10% equine serum (HyClone), 5% fetal bovine serum (HyClone), and 100 units/ mL penicillin/streptomycin (HyClone) on mouse collagen IV-coated culture dishes (BD Biosciences). Cells were maintained at 7% CO₂ atmosphere at 37° C and subcultured when confluency was reached, approximately every 7-9 days. Cell culture media was exchanged every 2-3 days throughout the lifetime of all cultures. Amperometric measurements were conducted on cells between days 4 and 5 after subculturing to minimize biological variances within the cell population.

6.2.2. Single Cell Measurements

Amperometric recordings at single cells were made using an inverted microscope (IX71, Olympus) positioned on top of a vibration isolation table (Model 63-563, Technical Manufacturing Corporation) inside a home-built Faraday cage. During experimentation, culture dishes were kept at 37 ± 1 °C using an automatic temperature controller (Model TC-344B, Warner Instrument Corp.). A carbon fiber electrode was positioned onto a cell by a micromanipulator (Model MHW-3, Narshige Inc) . The electrode was lowered until a slight deformation in the outline of the cell was observed. Using a second micromanipulator, a glass micropipette was positioned roughly 10-20 μm away from the cell and used to inject a high K^+ solution (isotonic saline solution with 100 mM KCl) directly onto the cell surface. A 5-second, 25 psi pulse (Femto Jet, Eppendorf/Brinkman Instruments) stimulated release of dopamine via exocytose. For a given cell, high K^+ pulses were applied every 45 seconds for 3 intervals. A constant potential was applied across the bipolar CFE to two Ag/AgCl reference electrodes, with the one inside the carbon fiber electrode as the working terminal and the other in the external solution as the reference terminal.

Amperometric data from single PC12 cells was recorded using an Axopatch 200B amplifier (Molecular Devices) and observed in real-time with the Axoscope software package (Molecular Devices). Data was acquired using a Digidata 1440a (Molecular Devices) interfaced with a Dell personal computer. During data acquisition, a 1.0 kHz low-pass filter was used and no further filtering was applied. Amperometric peaks were analyzed using the MiniAnalysis software detection algorithm (Synptosoft). A detection event was recognized when a signal with a local maxima and area under the curve exceeded a detection threshold of 5 times the root-mean-squared noise (RMS) acquired from a 2-second recording at the beginning of each individual amperometric trace. Post algorithm, the peaks were manually inspected to reject any electrical noise and to include peaks that were excluded due to their proximity to other amperometric events. Peaks which possessed a non-uniform top, double peaks, or overlapping peaks without a clear baseline were manually excluded in the analysis⁵². All statistical values are reported \pm standard error of the mean.

6.3. Results and Discussion

6.3.1.Characterization of a Bipolar Carbon Fiber Electrode

CFEs behave as closed bipolar electrodes and prior to single cell measurements, electrodes were characterized by cyclic voltammetry. This is an essential step in the experimental process so that the observed differences in amperometric experiments can be accurately attributed to the given bipolar configuration and not to any variance in electrode geometry. The voltammetric behavior of a microelectrode in a closed bipolar cell has been described previously¹⁸⁶. The magnitude of the diffusion-limited steady-state current is limited by the mass transfer at the anodic pole¹⁶³ which, in this case, is approximated to be disk-shaped geometry and is given by⁴

$$i_{ss} = 4nFDC^*r \quad (6-1)$$

where n is the number of electrons transferred, F is the Faraday constant, D is the diffusion coefficient for a given species, C^* is the bulk concentration of a redox species, and a is radius of the disk. Because of electroneutrality in a closed BPE the magnitude of current generated at the anode is equal to the current magnitude at the cathode. The overall shape and position of the i - E curve is dependent on the electron transfer reactions occurring at both poles and the half wave potential, $E_{1/2}$, is given by the following equation¹⁸⁶

$$E_{1/2} = (E_a^{o'} - E_c^{o'}) - \frac{RT}{F} \ln \left(-2 \left(\frac{i_{ss}^c}{i_{ss}^a} \right) - 1 \right) \quad (6-2)$$

where R is the gas constant, T is the absolute temperature, i_{ss}^a and i_{ss}^c are the limiting currents on the anodic pole and the cathodic pole, respectively, and $E_a^{o'}$ and $E_c^{o'}$ are the formal potentials for the reactions on the anodic and cathodic poles, respectively. As the ratio of the mass transfer between the cathodic and anodic poles approaches unity, the $E_{1/2}$ is equal to the difference in formal potentials.

The effect of changing the back-fill solution is illustrated in Figure 1b. Here the normalized steady-state voltammetric response of two 5- μ m carbon fiber electrodes is shown for a solution of 100 μ M DA using different configurations to establish electrical contact. Only forward scans are shown for clarity.

When the CFE is back-filled with colloidal graphite (black), the colloidal graphite comes into direct contact with both the interior carbon fiber sensor electrode and the Ag/AgCl reference electrode creating a pseudo-direct electron transfer similar to that of a continuous wire. Conversely, when a CFE is back-filled with 3 M KCl (blue), 5 mM $\text{K}_3\text{Fe}(\text{CN})_6$ in 3 M KCl (red), and 5 mM $\text{Ru}(\text{NH}_3)_6\text{Cl}_3$ in 3 M KCl (green) results in an indirect electron transfer via a bipolar mechanism. Here electron transfer is facilitated by the electrochemical coupling of the reactions occurring at the opposing poles of the carbon fiber. A noticeable shift in the position of the voltammogram can be attributed to this electrochemical coupling is quantitatively explained by Equation 2. For example, $E_{1/2}$, shown for the colloidal graphite electrode is ~ 0.4 V vs. Ag/AgCl and the $E_{1/2}$ for the $\text{Fe}(\text{CN})_6^{4-}$ molecule is ~ 0.3 V vs. Ag/AgCl, yielding a difference of ~ 0.1 V. Additionally the electrochemical surface area of the interior carbon fiber is significantly larger than the exterior sensing disk at the anode, hence the mass transfer ratio will favor the inner reaction and is manifested by an additional shift in the half wave potential towards negative potentials. For an electrode back-filled with 5 mM $\text{Fe}(\text{CN})_6^{4-}$, the observed $E_{1/2}$ was approximately 0.0 V. Similar logic can be applied to the formal and half-wave potentials for other back-filling solutions. The observed potential shifts are in good agreement with previous results obtained using a carbon fiber electrode electrochemically coupled to a carbon fiber in a closed bipolar cell¹⁸⁶.

It is difficult to control the length of the interior carbon fiber during electrode fabrication, which is important because as the interior carbon fiber length increases, the mass transfer rate at the cathodic pole increases, shifting the position of $E_{1/2}$. Electrodes were initially characterized using 3 M KCl as the back-fill solution. Only electrodes with an $E_{1/2}$ between + 0.15 and + 0.25 mV and i_{ss} between 0.12 and 0.20 nA were used for single cell experiments. This criterion was established based the expected $E_{1/2}$ of dopamine oxidation at a CFE and the expected current from a 2-electron transfer from DA oxidation at a 5 μm disk as calculated per Equation 1. Because of this specific criterion, any changes observed in the cell amperometry data can be attributed to the change in the back-filling solution and not to slight differences in electrode geometry.

6.3.2. Comparison of Different backfill solutions

PC12 cells were selected for analysis because it is a well-characterized cell line for the study of the dynamics of DA release via exocytosis¹⁸⁹. Because electrochemical sensing experiments require high temporal resolution to measure fast concentration changes at the electrode surface, the aim of these experiments is to examine the role that the electron transfer at the cathodic pole plays in the amperometric response of current transients observed. To investigate this effect, we chose to introduce redox molecules with different electron transfer kinetics at carbon fiber interfaces into the interior of the carbon fiber electrode and compare their amperometric responses. In the traditional back-fill solution, KCl, oxygen reduction is the primary Faradaic process occurring at the cathodic pole¹⁶³ which is known to have slow and sluggish kinetics¹⁶⁹. $\text{Fe}(\text{CN})_6^{4-}$ and $\text{Ru}(\text{NH}_3)_6^{3+}$ were chosen as redox mediators because of their fast electron transfer kinetics¹⁹⁰. As a base for comparison, electrodes were also back-filled with colloidal graphite.

Here we compare current transients observed from stimulated exocytosis of PC12 cells using these 4 different CFE configurations. Examples of amperometric traces obtained from a single stimulation event at each CFE are shown in Figure 2. A CFE back-filled with colloidal graphite (Figure 2a) was used to act as a pseudo-direct connect response while 3 M KCl (Figure 2b), 5 mM $\text{Fe}(\text{CN})_6^{4-}$ in 3 M KCl (Figure 2c), and 5 mM $\text{Ru}(\text{NH}_3)_6^{3+}$ in 3 M KCl (Figure 2d) were used as electrolyte solutions to examine indirect electron transfer via a bipolar mechanism. In conventional constant potential amperometry the voltage at the electrode surface is held at a high overpotential such that the electrochemical process at the sensing electrode is diffusion limited. For this reason a constant voltage of +750 mV was chosen and applied across the BPE for all configurations. Cell data was pooled from multiple amperometric traces of each electrode configuration: colloidal graphite (n = 13 cells using 6 different electrodes), $\text{Ru}(\text{NH}_3)_6^{3+}$ (n = 13 cells using 4 different electrodes), $\text{Fe}(\text{CN})_6^{4-}$ (n = 7 cells using 3 different electrodes), and KCl (n = 13 cells using 3 different electrodes). By qualitatively comparing the sample traces, slightly larger peaks are observed from the electrodes back-filled with colloidal graphite and $\text{Ru}(\text{NH}_3)_6^{3+}$. The relative frequency of detection is unaffected by the differences in electrode configurations. To confirm this qualitative observation, a Student's t-test was performed on the pooled data to compare the frequency of events detected after a single stimulation. At the 95% confidence level, the apparent difference in detection frequency is not statistically different between configurations. This

suggests that changes of the electrode back-filling solution does not significantly impact the mean number of detection events per stimulation.

Common metrics that are used to quantitatively describe amperometric data and qualitatively characterize vesicular release include the peak rise time, peak decay time, and peak half-width. Other characteristics include the peak amplitude and charge passed at the electrode surface. Applying Faraday's law to the peak area, the number of dopamine molecules detected can be determined from the following equation

$$Q = nNF \quad (6-3)$$

where Q is the charge passed, n is the number of electrons transferred per molecule (2 for dopamine), and N is the amount of substance detected in moles. The kinetic and charge parameters for each amperometric peak were resolved and characterized for the pooled cell data. Figures 3a and 3b summarize the quantified peak characteristics for each CFE configuration and the differences in detection become more pronounced. The numerical data is summarized in table 1. Electrodes back-filled with colloidal graphite demonstrated the highest average peak amplitude at 16.2 ± 0.5 pA and the peak amplitudes from 5 mM $\text{Ru}(\text{NH}_3)_6^{3+}$, 5 mM $\text{Fe}(\text{CN})_6^{4-}$, and 3 M KCl were 14.8 ± 0.3 , 13.8 ± 0.7 , and 8.7 ± 0.3 pA respectively. Because the RMS noise does not differ significantly between configurations, larger peak amplitudes also correlate to an increased signal-to-noise ratio. Figure 3b captures a large variance in the kinetic parameters observed for the different electrode configurations. The features that most highlight the difference in observed kinetics are the rise time and decay time. The rise time is directly related to the time it takes for the fusion pore to open and catecholamines to diffuse to the electrode surface, and the decay time represents the time duration needed for the fusion pore to close or all the vesicular contents to be consumed. The average rise time for colloidal graphite was 1.58 ± 0.04 ms, 1.59 ± 0.04 ms for 5 mM $\text{Ru}(\text{NH}_3)_6^{3+}$, 1.84 ± 0.06 ms for 5 mM $\text{Fe}(\text{CN})_6^{4-}$, and 2.24 ± 0.05 ms for 3 M KCl. The rise time for colloidal graphite and $\text{Ru}(\text{NH}_3)_6^{3+}$ are similar to each other while the rise times for $\text{Fe}(\text{CN})_6^{4-}$ and KCl when compared to colloidal graphite have increased by about 17% and 40%,

respectively. Similar trends were observed for the decay time and half-width suggesting more time is needed to consume the released dopamine for the electrolyte solutions.

These results suggest the kinetics of electron transfer at the cathodic pole cannot be assumed to be in sufficient excess to facilitate amperometric detection without contributing to the observed signal. Because the bipolar mechanism involves the electrochemical coupling of two Faradaic processes, the electron transfer rate at the cathode will partially limit the response. Colloidal graphite acts a direct connection for the carbon fiber and represents a standard of comparison. Noting the decreased peak amplitude and longer time components observed for 3 M KCl, there is a statistically significant decrease in kinetics when oxygen reduction is coupled to DA oxidation. These results show that the sluggish kinetics of oxygen reduction significantly distort the data towards lower current magnitudes and slower kinetics. A significant improvement in the kinetics is observed when an additional redox mediator such as $\text{Fe}(\text{CN})_6^{4-}$ is added to the back-fill solution. Furthermore, when $\text{Ru}(\text{NH}_3)_6^{3+}$ is present at the cathode, release kinetics similar to that observed using colloidal graphite can be obtained. We believe that the faster response for $\text{Ru}(\text{NH}_3)_6^{3+}$ arises because it exhibits faster electron transfer kinetics than $\text{Fe}(\text{CN})_6^{4-}$ at carbon surfaces¹⁹⁰.

In addition to release kinetics, the normalized frequency histogram depicting the amount of chemical released was plotted in Figure 3c. The data was plotted as the cube root of the catecholamine released as calculated from the charge; in this manner the event distribution is Gaussian and would serve better for comparison between different electrode configurations. Additionally, the assumption that the catecholamine concentration within each vesicle remains constant and the radius of the vesicle is proportional to vesicle content lends credence to plotting the data in this manner^{45,172}. The distributions from each electrode configuration were fit to Gaussian curves as shown by the dashed lines in Figure 3c. The Gaussian distributions for colloidal graphite, $\text{Ru}(\text{NH}_3)_6^{3+}$, and $\text{Fe}(\text{CN})_6^{4-}$ are in close agreement with each other while the distribution for KCl is shifted slightly towards a smaller vesicle content and is statistically different from colloidal graphite. It is important to note that this result arises not because there is an actual change in the distribution of relative vesicle content within the cells, but because of the slower kinetics of oxygen reduction in the case of KCl effectively distorting the data. This distortion could be quite significant in quantal studies. To frame this distortion differently, the average peak area for the

colloidal graphite configuration is 24.7 ± 0.6 fC and 21.2 ± 0.6 fC for 3 M KCl. The smaller peak area from the 3 M KCl data leads to a 14% decrease in total number of molecules detected compared data obtained when colloidal graphite was used. Conversely when $\text{Ru}(\text{NH}_3)_6^{3+}$ is present in the back-fill solution the average peak area is 24.0 ± 0.5 fC showing a less than 3% decrease in the number of molecules detected than colloidal graphite. The only variable that has been changed in this study is the content of the back-fill solution and our results indicate that the electrochemistry at the does affect amperometric measurements.

Our previous studies have shown that a limitation imposed on observed response can be minimized by increasing the mass transfer rate at the excess pole¹⁸⁶. This is accomplished by either increasing the electroactive surface area or the concentration of redox molecule at the cathodic pole. As previously mentioned, it can be difficult to control the length of the interior carbon fiber. Increasing the concentration of redox molecule present in the back-fill solution may be an easier parameter to control. We conducted additional cell experiments where the concentration of redox molecule was increased to 100 mM for both $\text{Fe}(\text{CN})_6^{4-}$ and $\text{Ru}(\text{NH}_3)_6^{3+}$. The results from $\text{Fe}(\text{CN})_6^{4-}$ demonstrated a slight kinetic increase from the lower concentration with an overall 3% increase in peak amplitude. The rise time increased while both the decay time and peak half-width decreased to similar values obtained from colloidal graphite. Increasing the $\text{Ru}(\text{NH}_3)_6^{3+}$ concentration also caused a minimal increase in kinetics, but it was not determined to be statistically different than the results observed from the lower concentration. The frequency histograms did not suggest a significant shift in relative vesicle content.

Additional experiments were conducted to test detection efficiency to fast concentration changes at a bipolar CFE surface by a controlled injection of analyte. A micropipette filled with 100 μM DA and a 5 μm CFE were placed in a solution of isotonic saline and positioned adjacent to one another using two micromanipulators with the tip of the electrode positioned directly next to the opening of the micropipette. Dopamine was injected directly on to the electrode surface by applying a 40 psi pulse for 0.1 s from the femtojet and the applied voltage bias was +750 mV. Figure 4 shows representative peaks obtained from the amperometric detection of injected DA at different bipolar configurations. Data was pooled from a minimum of 75 injections collected from 3 different electrodes at each configuration. Data from quantitatively peak analysis is shown in table 2. The representative peaks display samples whose current

magnitude is near the average from the pooled data. It was observed when colloidal graphite was used as the back-fill solution, the peaks were of significantly larger peak area than when electrolyte solution was used. The peak areas decreased to 96% for $\text{Fe}(\text{CN})_6^{3-}$, 84% for $\text{Ru}(\text{NH}_3)_6^{3+}$, and most notably when 3 M KCl was used the peak area was only 56% of the average value obtained with colloidal graphite. The injection parameters were kept constant and we believe this contrast arrives from the slower kinetics of oxygen reduction inefficiently coupling the dopamine oxidation at the sensing electrode surface.

These results are similar to those obtained from our single cell experiments in that the observed amperometric peaks vary with the mechanism of electron transport in the interior carbon fiber. In contrast to the cell experiments the released chemicals are spatially confined by the cell and electrode positions, the dopamine molecules in the injected stream move freely around the electrode and can cause significant variance in the detected peak. We believe that this also accounts for potential decreases in the amount of DA detected. In summation, we believe these results in combination with our cell data confirm that the distribution of current transients and observed kinetic parameters are dependent on bipolar electrochemistry and significant distortions occur if the electrochemical process at the cathodic pole is not fast enough. This distortion can be minimized by the addition of a redox mediator with fast electron transfer kinetics at the cathodic pole.

6.3.3. Voltage Effects on Detection

Figure 5 clearly illustrates one of the principle advantages to a bipolar approach to single cell analysis, namely the ability to observe exocytotic release with a lower applied electrode potential. Figure 5a is a current versus time amperometric trace collected with a CFE back-filled with 3 M KCl held at +100 mV near a cell and upon stimulation no amperometric peaks were detected. However, when the back-fill solution was exchanged to 3 M KCl containing 5 mM $\text{Fe}(\text{CN})_6^{4-}$ at +100 mV, secretory events were detected upon cell stimulation (Figure 5b). It's worth noting that the amperometric trace shown in Figure 5b was collected from the same cell using the same electrode and at the same voltage as Figure 5a. The only difference is the presence of $\text{Fe}(\text{CN})_6^{4-}$ in the back-fill solution of the CFE.

This phenomenon is explained by considering the steady-state voltammogram obtained from a CFE in a 100 μM DA solution. Figure 6a shows two voltammograms obtained from a single CFE back-

filled initially with 3M KCl and then with 3 M KCl containing 5 mM $\text{Fe}(\text{CN})_6^{4-}$. As observed in Figure 6a, in the voltammogram collected with 3M KCl as the back-fill solution (black trace) the DA oxidation is not diffusion limited at +0.1 V and zero current was measured. Conversely, in the presence of $\text{Fe}(\text{CN})_6^{4-}$ (Figure 6a, red trace), the voltage region where DA oxidation is under mass transfer control shifts towards more negative potentials as a result of electrochemical coupling. This allows current transients from DA oxidation from cells to occur at lower applied potentials.

To test the utility of amperometric detection at lower voltages, we conducted single cell experiments with electrodes back-filled with 3M KCl and 100 mM $\text{Fe}(\text{CN})_6^{4-}$ at +200 mV applied potential. The lower overpotential of +200 mV was selected based upon the i - E curves shown in figure 6a. At +200 mV the oxidative current is observable for both configurations; however in the case of KCl it is not mass transfer limited and there is an additional kinetic limitation. The vertical lines in Figure 6a indicate the relative position of this selected potential on the i - E curve. Current transients were measured and kinetic parameters were quantitated for both 3 M KCl ($n = 12$ cells, 4 electrodes) and 100 mM $\text{Fe}(\text{CN})_6^{4-}$ ($n = 15$, 6 electrodes) and are shown in table 3. The mean peak amplitude observed for 100 mM $\text{Fe}(\text{CN})_6^{4-}$ and 3M KCl was 10.4 ± 0.4 and 8.4 ± 0.2 pA, respectively. The kinetic parameters are slower for both cases as compared to the values obtained with the similar bipolar configurations at +750 mV. Although the characteristics observed at +200 mV for $\text{Fe}(\text{CN})_6^{4-}$ are slightly slower than at +750 mV, overall the results still indicate faster kinetics than that of 3 M KCl observed at both voltages. This data suggests that improved detection can be observed with an electrode back-filled with $\text{Fe}(\text{CN})_6^{4-}$ at a lower potential than that of an electrode filled only with KCl at a higher overpotential. This could have important implications for biological systems sensitive to high voltage application at the sensing electrode surface. Furthermore, the potential window of detection could be catered and tuned for different electroanalytical applications by choosing redox mediators with different formal potentials.

The distribution of vesicle content is also affected by lowering the applied voltage. Frequency histograms comparing the relative vesicle content detected at +200 mV and +750 mV for KCl and $\text{Fe}(\text{CN})_6^{4-}$ are shown in Figure 6b and 6c, respectively. From the distribution, it is observed that there is a significant shift towards greater vesicular content observed at the lower voltage for KCl, whereas the distribution for 100 mM $\text{Fe}(\text{CN})_6^{4-}$ is not statistically different between +200 mV and +750 mV. The

distortion which occurs in the KCl data arises not because of a sudden change in vesicular content within the cell population, but rather because there is a lower amount of smaller peaks detected. By decreasing the voltage applied the amount of current obtained from a release event decreases. Because peaks are only observed and quantitated when they exhibit a peak amplitude and area greater than the 5 times RMS noise threshold, the decrease in peak amplitude occurring at the lower voltage will cause peaks from small vesicles to be even smaller in magnitude and precluded in the analysis effectively distorting the data towards larger events. As evident from the kinetic parameters, the peaks which are observed have a shorter magnitude and a longer time duration, leading to slightly larger peak areas thus skewing the distribution. This doesn't occur in the case of ferricyanide because the decrease in average current magnitude and increase in kinetic parameters occurs proportionately such that the observed peak area doesn't shift the distribution of vesicle content.

6.3.4. Electrode Stability

To assess electrode stability, electrodes were exposed to repeated potential cycling of DA. Electrodes were placed in a solution of 100 μM DA and the potential was cycled at 100 mV/s to repeatedly oxidize DA at the electrode surface. The potential range for each bipolar configuration was adjusted based on the observed $E_{1/2}$ such that the total voltage range spanned 1.2 V for each. In this manner, the relative scan range would be similar for each bipolar configuration. Figure 7a contains a plot of the normalized steady-state current versus the number of cycles. The steady-state current is normalized with respect to the steady-state current obtained during the initial scan, i_{ss}^* . It is observed that the steady-state current for the colloidal graphite configuration remains relatively constant after 300 cycles with an observed decrease of less than 3%. Conversely, the magnitude of the steady-state current decreased to 90%, 84%, and 81% of the initial value for $\text{Fe}(\text{CN})_6^{4-}$ and $\text{Ru}(\text{NH}_3)_6^{3+}$ and KCl respectively. We believe this results from a combination of electrode fouling and consumption of redox molecule inside the capillary. As the potential is cycled and DA is repeatedly oxidized, the electrochemically-coupled redox mediator inside the capillary will be depleted.

From the voltammograms obtained during the potential cycling, we can gain insight into the role redox molecule depletion has on electrode response. Figure 7b shows the voltammetric response of a

CFE back-filled with 3 M KCl at different stages during the potential cycling. The solid line represents the initial voltammogram and the dashed line represents the voltammogram obtained after 300 cycles. After 300 cycles, the $E_{1/2}$ has shifted to a more positive potential and the current has decreased and does not reach a clear steady-state response. A similar positive shift in $E_{1/2}$ was also observed from the other bipolar configurations after potential cycling, and no matter how great the decrease in current magnitude was after continuous potential cycling, the potential needed to drive the reaction to steady-state increased. After initial cycling, a fresh injection of 3 M KCl was back-filled into the capillary to replenish any consumed oxygen from the previous cycling to see if the original response could be recovered. The voltammetric response was generated in the same DA solution and is represented by the dotted curve in Figure 7b. The magnitude of the steady-state was recovered to 96% of its original value. This suggests that the loss in current magnitude results directly the depletion of redox mediator and can be recovered. The $E_{1/2}$ is slightly shifted in the negative direction and there is an increase in the charging current. We believe that these are consequences of the irreversible adsorption of byproducts of DA oxidation to the electrode surface. Similar results were obtained from the $\text{Fe}(\text{CN})_6^{4-}$ and $\text{Ru}(\text{NH}_3)_6^{3+}$ configurations. In the case of $\text{Fe}(\text{CN})_6^{4-}$ after 300 cycles the current had decreased to 90% of its initial value and after replenishing the electrolyte in the capillary 96% of the current was recovered. For $\text{Ru}(\text{NH}_3)_6^{3+}$ after 300 cycles the current had decreased to 84% of the initial value and after addition of additional $\text{Ru}(\text{NH}_3)_6^{3+}$ 90% of the current was recovered. In summation, the results of our stability experiments show that electrode fouling still occurs when a redox molecule is present in the back-fill solution but losses in current magnitude can be recovered by replenishing the electrolyte.

6.4. Conclusion

We have demonstrated the effect that bipolar electrochemistry has on the detection of exocytosis from PC12 cells. When an electrolyte solution is used to indirectly establish electrical conductivity in a CFE, a bipolar mechanism facilitates electron transfer. The observed response is dependent on the kinetics of the reaction on the interior carbon fiber and when the coupled reaction is oxygen reduction (such as for a KCl solution), the cathodic reaction cannot keep up with oxidation on the exterior sensing electrode. This, ultimately, is observed as a distortion in the recorded data. In order to overcome these

kinetic limitations, a redox mediator such as hexamineruthenium (III) chloride can be added to the back-fill solution. By applying bipolar electrochemical principles, the voltage at which current transients occur can be altered and meaningful detection can be obtained at lower voltages with $\text{Fe}(\text{CN})_6^{4-}$ present in the back-fill solution. We have also demonstrated that although electrode fouling occurs independently of the back-fill solution, the loss of current magnitude can be offset by simply supplying more redox molecules to the back-fill solution.

6.5. Tables and Figures

Table 6-1. Average kinetic parameters obtained from pooled amperometric data for the electrochemical detection of dopamine released from PC12 cells at +750 mV applied potential.

Back-fill Solution	Amplitude (pA)	Rise Time (ms)	Decay Time (ms)	Half Width (ms)	Area (fC)
Colloidal Graphite	16.2 ± 0.5	1.58 ± 0.04	1.64 ± 0.04	1.67 ± 0.03	24.7 ± 0.6
5 mM Fe(CN) ₆ ³⁻	13.8 ± 0.7	1.84 ± 0.06	1.85 ± 0.08	1.84 ± 0.07	22.9 ± 1.1
5 mM Ru(NH ₃) ₆ ³⁺	14.8 ± 0.4	1.59 ± 0.04	1.71 ± 0.03	1.76 ± 0.03	24.0 ± 0.5
3 M KCl	8.70 ± 0.3	2.24 ± 0.05	2.26 ± 0.06	2.16 ± 0.05	21.2 ± 0.6

Table 6-2. Average peak area obtained from peaks obtained in **figure 6-4**. Data is averaged from a minimum of 75 peaks obtained from 3 different electrodes at each configuration.

Back-fill Solution	Amplitude (pA)	Half Width (ms)	Area (pC)	% of total
Colloidal Graphite	341 ± 7	112 ± 2	341 ± 1	100.
5 mM Fe(CN) ₆ ³⁻	351 ± 8	98.2 ± 1.4	327 ± 1	96.0
5 mM Ru(NH ₃) ₆ ³⁺	309 ± 8	97.9 ± 1.7	287 ± 1	84.1
3 M KCl	195 ± 9	88.8 ± 3.3	190 ± 1	55.6

Table 6-3. Average kinetic parameters obtained from pooled amperometric data for the electrochemical detection of dopamine released from PC12 cells at +200 mV applied potential.

Back-fill Solution	Amplitude (pA)	Rise Time (ms)	Decay Time (ms)	Half Width (ms)	Area (fC)
5 mM Fe(CN) ₆ ³⁻	10.4 ± 0.4	1.89 ± 0.04	2.22 ± 0.04	2.16 ± 0.04	22.5 ± 0.7
3 M KCl	8.4 ± 0.2	2.34 ± 0.05	3.25 ± 0.06	2.80 ± 0.05	28.4 ± 0.9

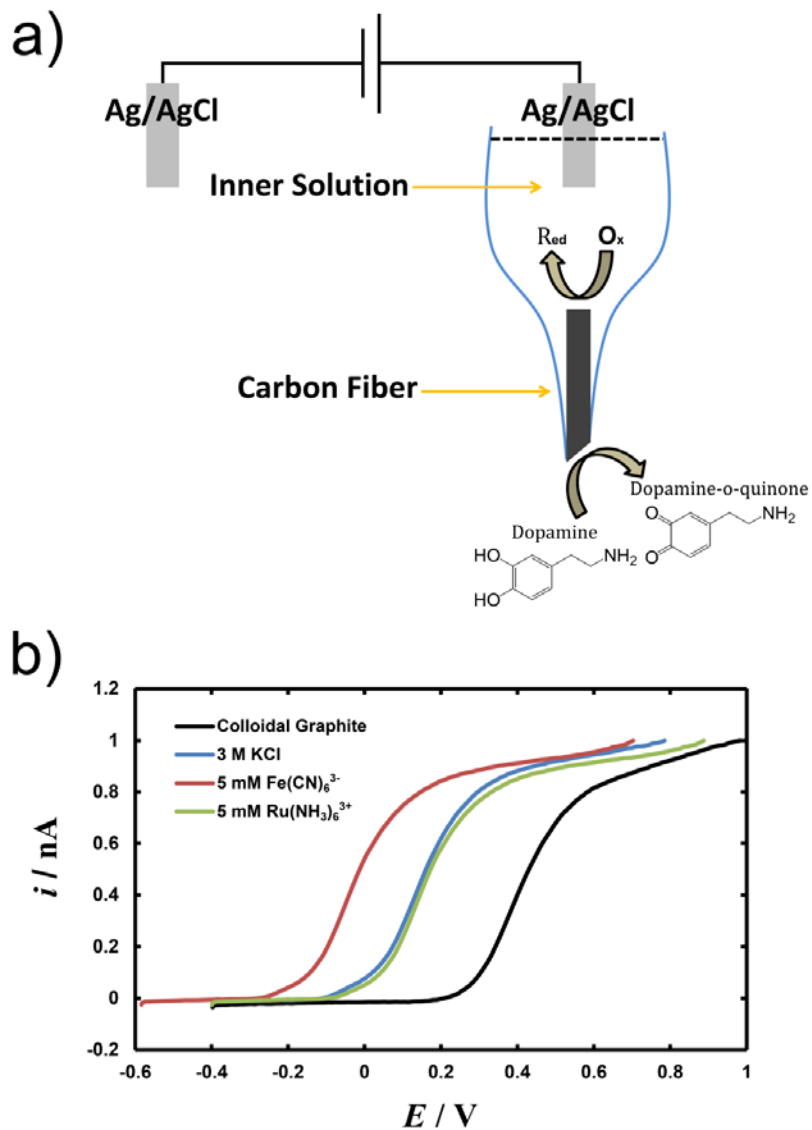


Figure 6-1. a) Schematic of a carbon fiber electrode depicting its bipolar nature. b) Normalized steady-state response observed from the oxidation of 100 μM DA at 2 different 5 μm carbon fiber electrodes. The first electrode was back-filled with colloidal graphite (black) for a pseudo-direct connection to the fiber, the second was back-filled with various electrolyte solutions: 3 M KCl (blue), 5 mM $Fe(CN)_6^{4-}$ in 3 M KCl (red), and 5 mM $Ru(NH_3)_6^{3+}$ in 3 M KCl (green). Scan rate 100 mV/s.

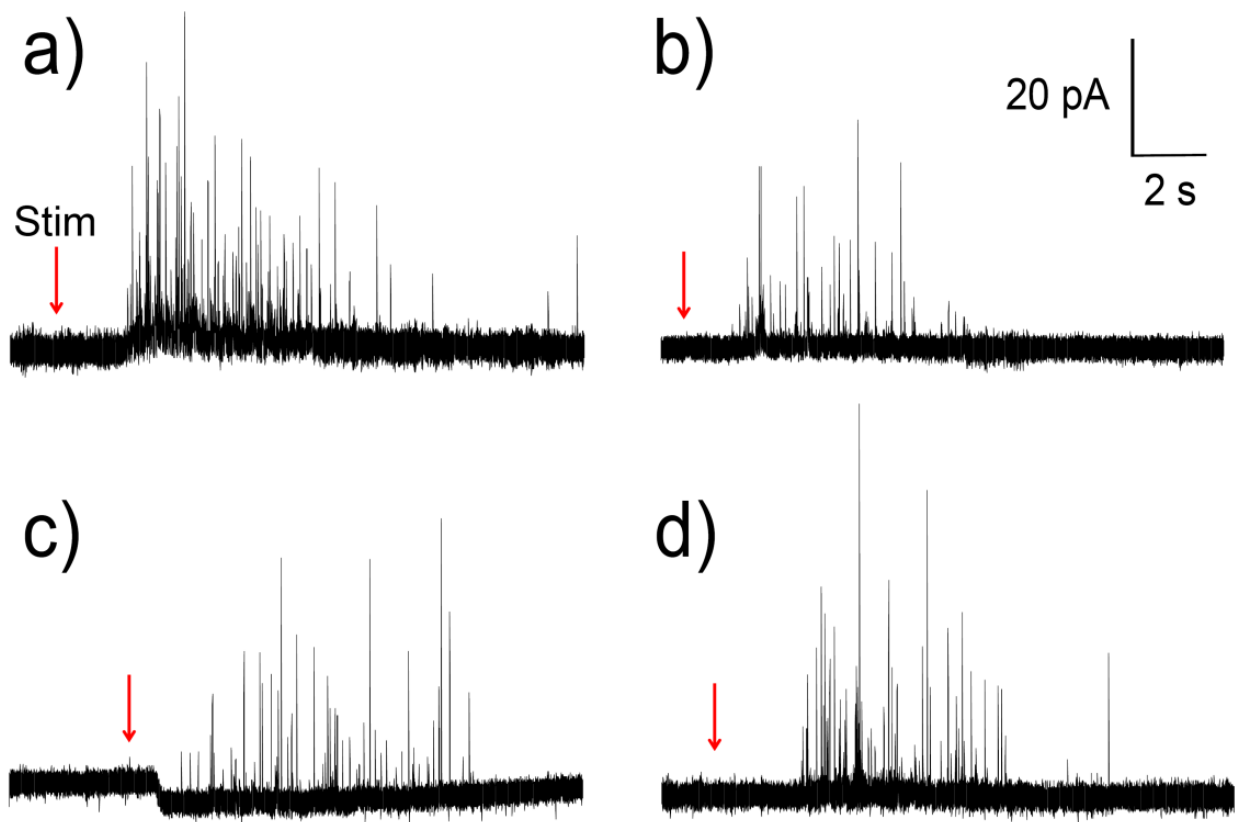


Figure 6-2. Representative amperometric traces showing the exocytotic response of PC12 cells at carbon fiber electrodes back-filled with different solutions. Electrodes were back-filled with a) colloidal graphite, b) 3 M KCl, c) 5 mM $Fe(CN)_6^{4-}$ in 3 M KCl, and d) 5 mM $Ru(NH_3)_6^{3+}$ in 3 M KCl. The red arrow indicates the time point at which a high K^+ stimulant was applied to the cell.

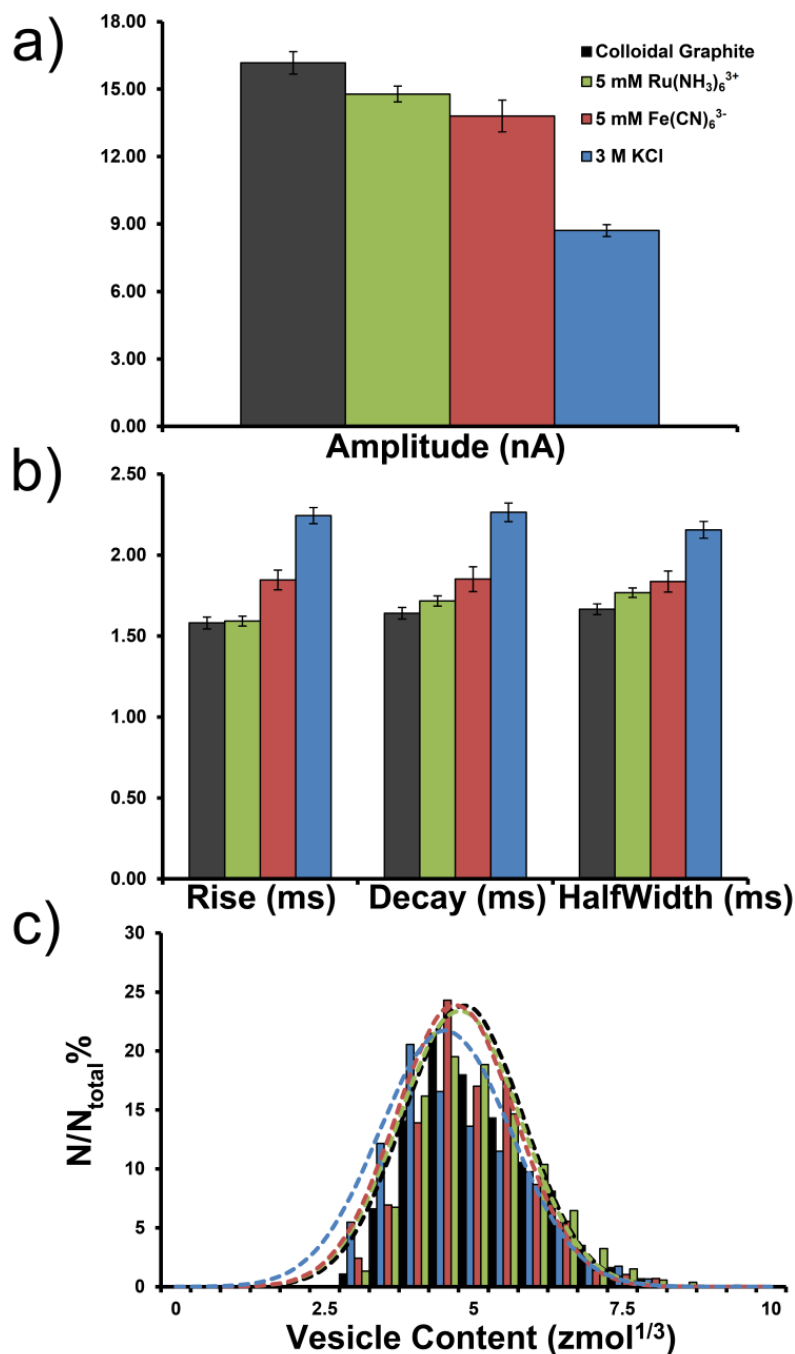


Figure 6-3. a) Mean peak amplitude and b) kinetic parameters observed for detection at different bipolar configurations. Cell data was pooled from detection at multiple cells with multiple electrodes; black – colloidal graphite (n = 13), green – 5 mM Ru(NH₃)₆³⁺ in 3 M KCl (n=13), red – 5 mM Fe(CN)₆⁴⁻ in 3 M KCl (n = 7), and blue – 3 M KCl (n=12). c) Distribution of vesicle content detected from PC12 plotted as the cube root of the catecholamine released as calculated from the charge on the electrode surface. Data is fit to Gaussian distributions shown in dashed lines.

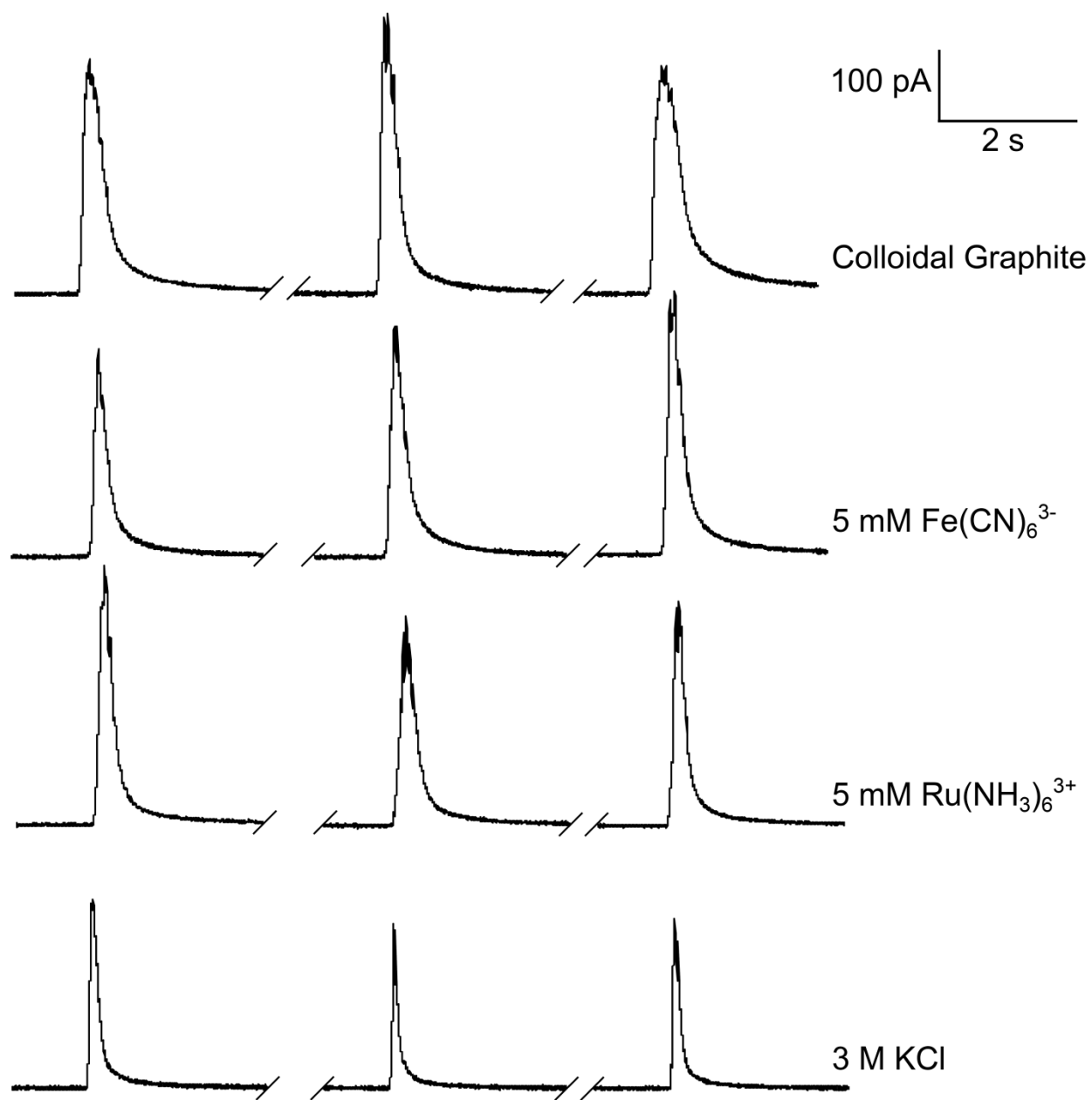


Figure 6-4. Representative amperometric peaks obtained from the detection of dopamine at a 5 μm CFE via micropipette injection. A micropipette filled with 100 μM dopamine was positioned directly next to a CFE and a 0.1 s 40 psi pulse injected sample directly to the electrode surface ($n = 3$ electrodes). Each spike represents an individual injection. The applied potential was +750 mV. Electrodes were back-filled with different solutions as indicated.

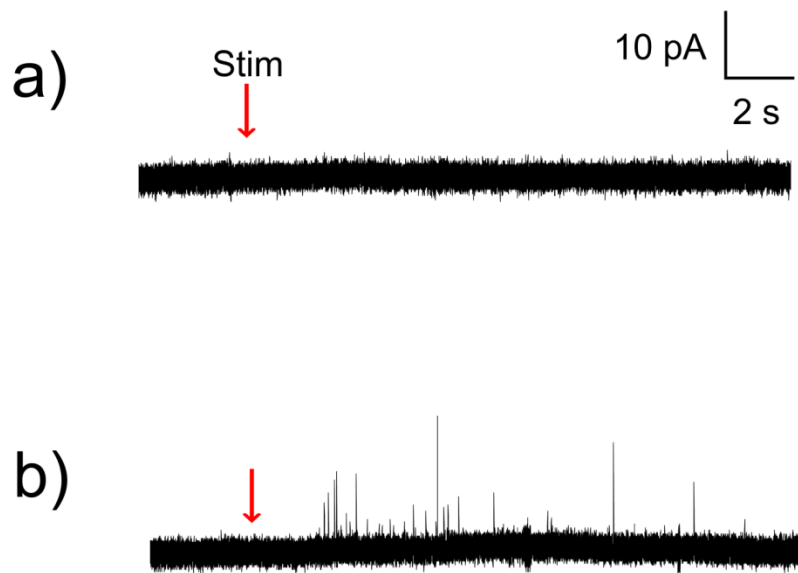


Figure 6-5. Voltage-dependence on amperometric detection. a) Current versus time amperometric trace of a single stimulation event with a CFE back-filled with 3 M KCl held at +100 mV. b) Current versus time amperometric trace at the same cell with the same electrode back-filled with 100 mM $\text{Fe}(\text{CN})_6^{4-}$ in 3 M KCl with the electrode potential held at +100 mV.

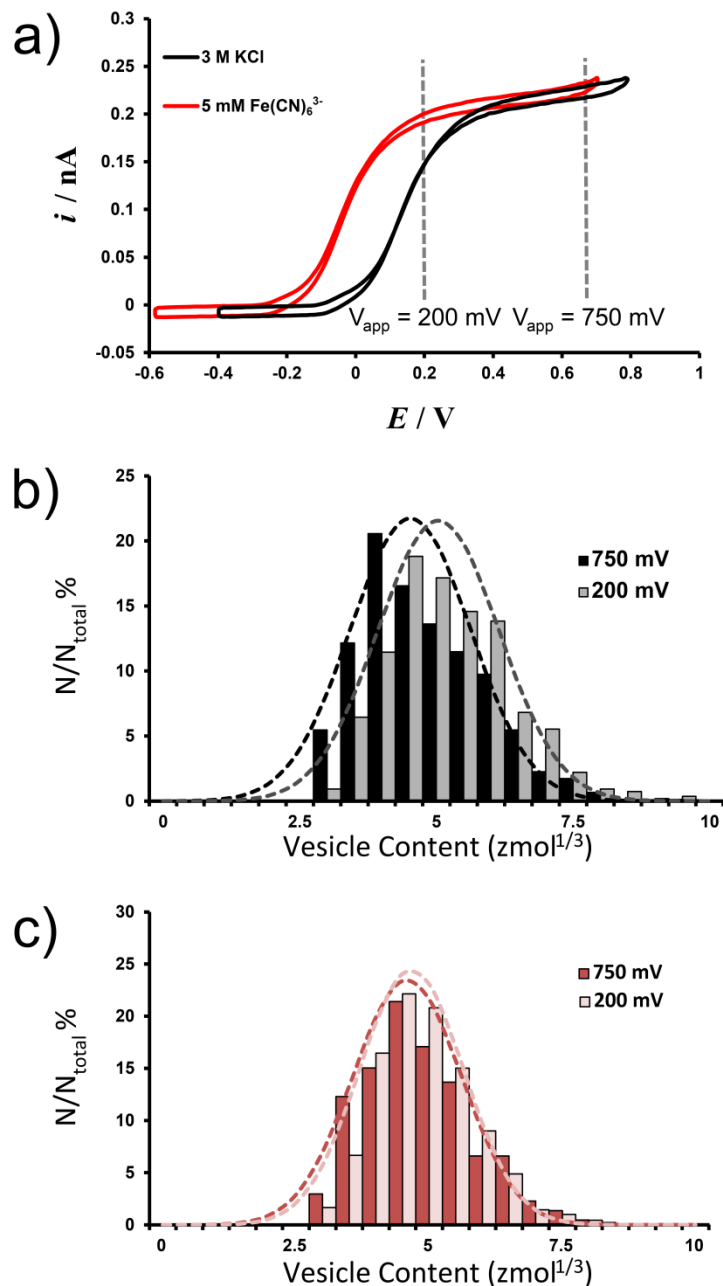


Figure 6-6. a) Voltammetric response from the oxidation of $100 \mu\text{M}$ DA at a $5 \mu\text{m}$ CFE back-filled with 3 M KCl (black) and 100mM $\text{Fe}(\text{CN})_6^{4-}$ in 3 M KCl (red). The gray dashed lines in the figure represent the relative location in the voltammogram at which potential was held during amperometric detection. Distribution of vesicle content detected from PC12 cells at different voltages with different electrolyte solutions, b) 3 M KCl, and c) 100mM $\text{Fe}(\text{CN})_6^{4-}$ in 3 M KCl, plotted as the cube root of the catecholamine released. Cell data was pooled from detection at multiple cells; 3 M KCl at +750 mV ($n=12$), 3 M KCl at +200 mV ($n=10$), 100mM $\text{Fe}(\text{CN})_6^{4-}$ at +750 mV ($n=12$), and 100mM $\text{Fe}(\text{CN})_6^{4-}$ at +200 mV ($n=15$). Dashed lines indicate Gaussian distributions that were fit to the data.

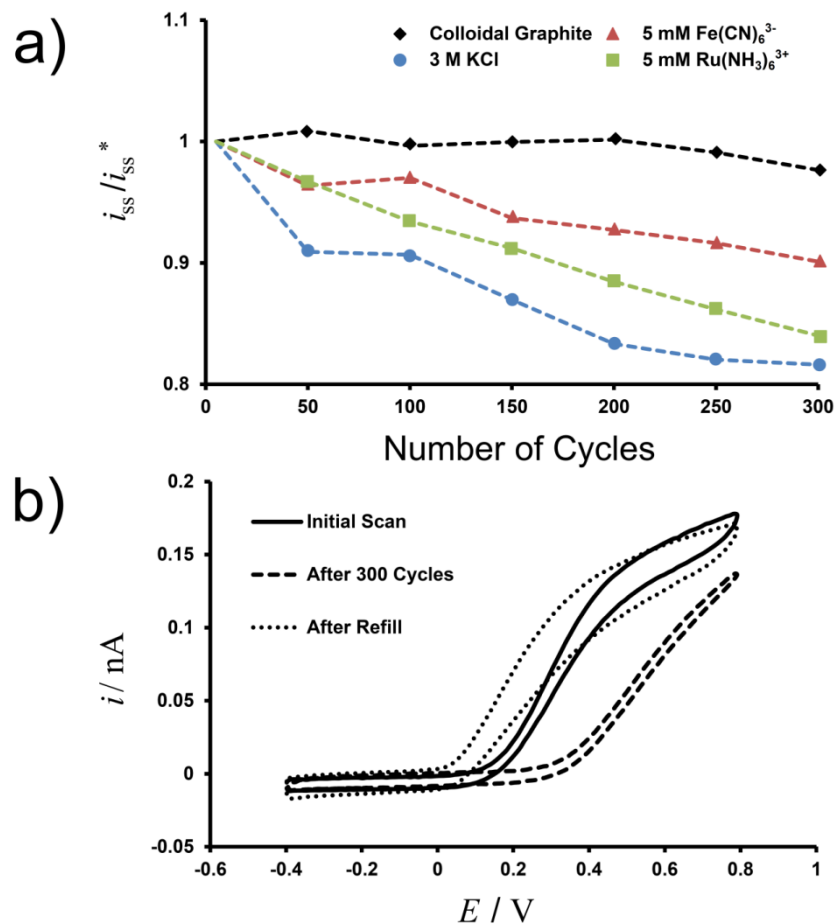


Figure 6-7. The effect of potential cycling on cyclic voltammetry. a) Plot of the normalized limiting current obtained from the oxidation of 100 μM DA at a carbon fiber disk electrode with various back-filled solutions versus the sequential scan number. Current is normalized with respect to the initial limiting current obtained from the first scan. b) Voltammetric response of a 5 μm CFE back-filled with 3 M KCl in a solution of 100 μM DA at different stages of potential cycling, the initial cycle (solid line), after 300 cycles (dashed line), and after cycling and replacing the back-fill solution with fresh 3 M KCl (dotted line).

CHAPTER 7 RESISTIVE-PULSE ANALYSIS OF SINGLE PHOSPHOLIPID VESICLES USING QUARTZ NANOCANNELS[§]

7.1. Introduction

Vesicles are key cellular components and play essential roles in numerous basic biological functions, such as intra- and intercellular transport,¹⁹¹ immune response,¹⁹² hormone release¹⁹³ and neurotransmission.¹⁹⁴ In addition, artificial large unilamellar vesicles (LUVs) have been extensively utilized as a model system for biologic membranes.¹⁹⁵ It is often important to characterize the size of phospholipid vesicles in order to more fully understand their biophysical and biochemical functionalities. Such characterizations have been traditionally carried out using several analytical techniques, including cryogenic transmission electron microscopy (TEM),¹⁹⁶ freeze-fracture electron microscopy,¹⁹⁷ and dynamic light scattering (DLS).¹⁹⁸ Electron microscopy-based techniques provide direct observation of the size and shape of individual vesicles. However, such characterizations normally involve time-consuming sample preparation and complicated instruments and the vesicle samples are destroyed in the imaging process. Light scattering techniques on the other hand, offer fast and noninvasive characterization of vesicles suspended in solution. It is important to note that such measurements often require relatively large amount of samples and can only yield statistical results based on analyzing many vesicles.¹⁹⁹

In many cases, it is advantageous to characterize individual vesicles in solution noninvasively so that other analytical techniques can be combined on the same vesicles to analyze their other properties,²⁰⁰ e.g., their neurotransmitter concentration, or vesicular protein content. The aforementioned analytical methods have failed to provide such opportunities. Harris and co-workers recently reported a method quantify the molecular occupancy of vesicles using quantitative fluorescence microscopy by encapsulating dye molecules inside the vesicle.²⁰¹ Chiu and co-workers also reported a powerful method of measuring the hydrodynamic size of single fluorescently-labeled vesicles by measuring their diffusion coefficient.²⁰² While these methods both deliver further insight into vesicle characterization, both require vesicle labeling. We have been interested in developing nanopore-based analytical methods to analyze individual vesicles directly isolated from single neurons or model neuronal cells without. Such vesicles

[§] Portions of this section are excerpted from a manuscript in preparation. Research was done in collaboration with Ernest Tomlinson, and Marissa Wood.

can range from below 50-nm for presynaptic neurons²⁰³ to as large as several hundred nm in diameter for certain model cells.²⁰⁴ Here, we wish to present our results in using resistive-pulse methods to quantitatively analyze the size of individual phospholipid vesicles ranging between 100 to 300 nm.

Since the advent of the Coulter counter²⁰⁵ the resistive-pulse methods have been extensively studied to analyze micro- and nanoparticles and single small molecules.²⁰⁶ In addition, commercial instruments based on resistive-pulse sensing are available to analyze biomedical samples and micrometer-scale particles. Resistive-pulse methods measure a transient change of an ionic current flowing through a nanopore or nanochannel, which occurs when an analyte particle translocates through the nanopore.²⁰⁷ The change of the ionic current is generally closely related to the volume of the analyte particle, which provides the basis for measuring the size of the analyte particle. Figure 7-1 shows a cartoon of a vesicle entering the sensing zone of a cylindrical nanochannel (not drawn to scale) and the corresponding current-time pulse response for a single detection event. As a vesicle passes through the nanochannel, a resistive current pulse is observed with amplitude that is directly related to the size of the particle,^{207,208}

$$\frac{\Delta i_c}{i_c} = S(d_s, d_c) \frac{d_s^3}{l'_c d_c^2} \quad (7-1)$$

where i_c is the baseline current, Δi_c is the amplitude of the current pulse, d_s is the diameter of the particle, d_c is the diameter of the nanochannel, and l'_c is the “end effect” corrected length given by: $l'_c = l_c + 0.785d_c$. The correction factor $S(d_s, d_c)$ is dependent on the ratio of d_s to d_c ,

$$S(d_s, d_c) = \frac{1}{1 - 0.8 \left(\frac{d_s}{d_c}\right)^3} \quad (7-2)$$

The Crooks' group has pioneered the use of novel carbon nanotubes to quantitatively analyze single polymer nanoparticles as small as ~55 nm in diameter.²⁰⁹ Further research has integrated resistive pulse sensors in microfluidic devices for the analysis of other nanoscale objects.²¹⁰ In addition to analyzing the size of single nanoparticles, resistive-pulse methods have been utilized to study molecular interactions

and molecule-pore interactions.²¹¹⁻²¹⁵ Here, we demonstrate that resistive-pulse methods are effective to analyze single phospholipid vesicles prepared by lipid extrusion. Single vesicles and polystyrene nanoparticles in the range of 100-400 nm in diameter have been analyzed using cylindrical quartz nanochannels prepared on glass micropipettes. In this work, nanoparticles and vesicles are driven through quartz nanochannels via an applied pressure. Polystyrene nanoparticles were used as a size standard for comparison with vesicle samples. Our results show that the nanochannel methods can be used to accurately detect and analyze single vesicles of different sizes. This method has a couple clear advantages. Nanochannels fabricated in this manner are robust and low-cost and lead to quick sample analysis. Furthermore this method may have important implications for vesicle analysis because there is no need for fluorescent labeling. This will allow direct analysis of vesicles isolated from cellular samples. Additionally because vesicle populations are not altered by the detection mechanism this method has potential to be coupled to other analytical methods to yield comprehensive information about the size and content of individual vesicles.

7.2. Experimental Section

7.2.1. Preparation of Phospholipid Vesicles

Vesicles were prepared by extruding a hydrated lipid solution through a polycarbonate membrane.²¹⁶ In this process a lipid film was prepared by taking 200 μ L of chloroform solution containing 5 μ g/mL lipids and evaporating the chloroform under a stream of nitrogen gas. The film was placed under vacuum in a desiccator for 2 hours to remove residual solvent. The lipid films were stored in a -15 °C freezer until further use. To hydrate the lipid films, 1 mL of 1x PBS buffer solution (pH = 7.3) was added and the resulting lipid solution was heated to 40 °C and allowed to hydrate for a minimum of 30 minutes. The hydrated lipid solution was diluted by a factor of 50 and extruded 15 times through a polycarbonate membrane. In order to obtain vesicles of different sizes, 100 nm and 200 nm pore size diameter polycarbonate membranes were used. Size distributions from the prepared vesicle population the size of the vesicles were determined by DLS using a Malvern Zetasizer Nano ZS. The results reported were the average of 3 DLS runs.

7.2.2. Resistive-Pulse Sensing of Single Nanoparticles and Vesicles

Particle detection was carried out in a custom built Lucite pressure cell with a 1 mL sample capacity. A schematic of the pressure cell is shown in Figure 7-1c. A constant pressure was supplied by a Femtojet microinjector (Eppendorf) in continuous flow mode. Unless otherwise noted, all the pressures are applied from the outside of the nanochannel vs. the inside. The nanochannel is fixed inside the Lucite cell and suspended in a buffer solution. The voltages reported in this work refer to voltages that were applied on the inner reference electrode versus the reference electrode on the outside of the channel in the bulk solution. Current-time traces for vesicles and polystyrene nanoparticles were recorded with an Axopatch 200B amplifier (Molecular Devices) and observed in real time with the Axoscope software package (Molecular Devices). The current-time traces were acquired using a Digidata 1440a (Molecular Devices) interfaced with a Dell computer. A 1.0 kHz low-pass filter on the 200B amplifier was used during the data acquisition. No further filtering was applied. Resistive pulses from the amperometric data were analyzed using Mini Analysis (Synptosoft Inc.). Pulses were counted as a detection event if the amplitude of the current and the area under the curve exceeded a threshold of five times the root-mean-squared noise for a flat 5-s recording at the beginning of each experiment. The data from Mini Analysis was manually evaluated to exclude double peaks and peaks that arose from electrical noise as well as manually include peaks that were not detected due to their proximity in the current trace.

7.3. Results and Discussion

7.3.1. Characterization of Cylindrical Quartz Nanochannels

Resistive-pulse sensing uses a transient current pulse to analyze individual nanoparticles. In order to analyze the size of single nanoparticles and vesicles, it is necessary to fully characterize the geometry of the nanochannels. For a cylindrical quartz nanochannel, the critical geometric factors are the diameter and length. In this work, the channel length is readily determined with ~10% uncertainty by optical microscopy for ones that are longer than 5 μm . This method is limited by the resolution of the microscope and it is difficult to measure shorter nanochannels. Once the length is measured, the diameter can be determined from its ionic resistance in a salt solution of known resistivity. The ionic resistance of a cylindrical-shaped nanochannel is proportional to its length, l_c , and inversely proportional to the square of its diameter, d_c^2 ,

$$R = \rho \frac{4l_c}{\pi d_c^2} \quad (7-3)$$

where R is the resistance and ρ is the resistivity of the solution. As an example, figure 7-2a shows the current-voltage response of a nanochannel in a 0.1 M KCl solution. The i - V response displays a linear behavior characteristic for a cylindrical nanochannel. The ionic resistance as determined from the slope of the plot is 82.5 M Ω , which corresponds to a diameter of 640 nm. Figure 7-2b shows an SEM image of the same nanochannel. The diameter of the orifice in this SEM image is ~670 nm in good agreement with that measured from resistance measurement.

7.3.2. Resistive-Pulse Sensing of Polystyrene Nanoparticles

The goal of our current work is to use cylindrical quartz nanochannels in the range of 400-600 nm in diameter to characterize the size of individual phospholipid vesicles. To test the applicability of using quartz nanochannels in this manner we used polystyrene nanoparticles between 170 and 400 nm in diameter as size standards to validate our methods. We have previously reported detection of nanoparticles as small as ~40 nm in diameter using quartz nanochannels below 150 nm in diameter.⁵⁸ The purpose of the previous work was to demonstrate the detection of nanoparticles. We did not previously explore the use of such nanochannels for sizing nanoparticles. Both the nanochannels and the analyte particles were significantly smaller than the ones used in the current study and were driven through the channel by electroosmotic force. The vesicles used in this study do not contain a significant surface charge and in order to drive the particles through the channel an external pressure was applied. By using the constructed Lucite cell a constant pressure is applied outside the nano channel and controlled so that particles will traverse the channel and their translocation monitored amperometrically without electroosmotic flow.

Figure 7-3a shows three current-time traces of a 470-nm-diameter quartz nanochannel ($l_c = 40 \mu\text{m}$) in a 0.1 M KCl solution containing 0.1% Triton X-100. The top trace is the result of a control experiment in which no nanoparticles were present in the solution. A steady baseline was observed at a voltage bias of -1 V and 1 PSI. The middle trace shows individual detection events for 175 nm polystyrene nanoparticles. Stochastic current pulses were clearly detected after particles were added to

the external solution indicating translocation of nanoparticles. The concentration of nanoparticles was 1.8×10^{10} particles/ml. Unlike conical nanopores, cylindrical quartz nanochannels give square resistive pulses due to their uniform diameter. The bottom trace shows an individual detection event with a characteristic square wave shape, however this is only true for cylindrical nanochannels with length much greater than their diameter.

For square resistive pulses shown in figure 7-3a, the pulse height can be readily determined. The average pulse height in this trace is about 5.5 pA corresponding to a nanoparticle size of ~210 nm in diameter. Figure 7-3b shows the size distribution of polystyrene nanoparticles measured by this nanochannel. About 700 nanoparticles were analyzed to yield a particle diameter of 213 ± 9 nm. We have repeated such measurements with multiple nanochannels of different sizes and compared our nanochannel results with particle diameters measured from DLS and SEM. Table 1 shows a comparison of the particle diameters determined from three different methods, DLS, SEM and the resistive-pulse method. For the 175-nm particles the particle size measured by DLS was 194 ± 31 nm in diameter, which is slightly larger than the mean particle size of 175 nm given by the manufacturer. From SEM the observed particle size was 186 ± 7 nm. We believe that the particles detected in this experiment are slightly larger than the value obtained by SEM because of particle swelling~~Error! Bookmark not defined.~~ and inherent differences in the experimental methods.²⁰⁹ DLS functions by correlating the diffusion of particles under Brownian motion to the particle size using the Stokes-Einstein relationship. In this method the hydrodynamic diameter of the particle is measured which is slightly larger due to the surface chemistry of the particles. The polystyrene spheres employed in this study are terminated with a sulfate ester and it has been demonstrated that in the presence of an aqueous or polar solvent, sulfonated polystyrene spheres will swell and slightly increase in size.²¹⁷ We assume that the diameter obtained from our nanochannel experiments is similar to the hydrodynamic radius obtained by DLS because the particles are suspended in the same running buffer. Conversely the particles analyzed via SEM are dry and hydrodynamic effects caused the particle's surface chemistry can be ignored yielding slightly smaller particle sizes.²⁰⁹ We repeated the detection experiments with 5 quartz nanochannels of different sizes and we observed the average particle size to be 198 ± 40 nm for the nominal 175 nm polystyrene spheres. This value is in good agreement with the DLS data and within 6% of the value obtained from

SEM. For the larger 356 nm particles similar results are obtained with the particle size closely matching the DLS data and within 3% of the diameter obtained by SEM imaging. This demonstrates that the size of nanoparticles can be accurately determined by the resistive pulse method using quartz nanochannels.

In our experiments the translocation of nanoparticles is mainly driven by the applied pressure rather than electrophoretic forces. There is a slight anionic charge on the particles from a sulfate ester groups on the surface however the surface charge is negligible. This is manifested in the data by the fact that particle detection occurred at both positive and negative voltages and there was no obvious difference in the frequency of particle detection. In addition, there was no dependence of particle size on pulse width but the scatter of the pulse width is the same for +1 and -1 V bias voltages. Figure 7-3c is a plot of calculated particle diameter against the pulse width at both positive and negative voltages under the same applied pressure. One can clearly see that the majority of the nanoparticles are around 200 nm in diameter with a translocation time τ of ~9 ms.

7.3.3. Resistive-Pulse Sensing of Vesicles

We have used the same principle to analyze single phospholipid vesicles in the range of 100 to 300 nm in diameter. *To the best of our knowledge, this is the first demonstration that nanopore/nanochannel sensors are used to quantify single phospholipid vesicles.* Figure 7-4a displays *i-t* traces of a 430-nm-diameter cylindrical quartz nanochannel ($l_c = 21 \mu\text{m}$) in a 1x PBS buffer solution containing 20 $\mu\text{g/ml}$ of 200 nm DOPC vesicles. The top panel of figure 7-4a is the result of a control experiment showing an *i-t* trace of this nanochannel in the absence of vesicles. A nice and stable baseline current is obtained. The middle panel shows an *i-t* trace of the same nanochannel in the buffer solution in the presence of vesicles. Individual current pulses are clearly seen indicating detection of single vesicles. One can immediately notice that the pulse magnitudes in this case are not as uniform as that in the case of the polystyrene nanoparticles. This is likely due to a broader distribution of vesicle sizes. An individual square-shape resistive pulse is shown in the bottom panel of figure 7-4a. The shape of this peak is similar to those observed from polystyrene nanoparticles suggesting that the vesicles can be analyzed in a similar manner.

Figure 7-4b shows the size distribution of 100 nm DOPC vesicles as determined from resistive-pulse sensing using a 570-nm-diameter nanochannel. Roughly 1700 vesicles were analyzed in this plot and the vesicle size as determined from equation 1 was 144 ± 23 nm in diameter. The mean particle size is in good agreement with the value obtained from DLS. Figure 7-4c also shows a similar distribution for a solution of 200 nm DOPC vesicles using a 490-nm-diameter nanochannel. The average vesicle size was calculated to be 213 ± 37 nm in diameter. The red curves in both graphs represent the size distribution determined from DLS measurements. From DLS the DOPC vesicles extruded through a 200 nm polycarbonate membrane were measured to be 188 ± 85 nm in diameter, and vesicles that were extruded through a 100 nm membrane were 140 ± 48 nm in diameter which is within typical range of vesicles prepared in this manner.²¹⁸

As one can see, in both cases the size distributions we observed via resistive-pulse sensing were significantly narrower than DLS. The differences in the mean diameters determined from DLS and resistive-pulse sensing are likely due to the limitation of our current nanochannel-based method. The analysis of single phospholipid vesicles using nanochannels is based on finite changes in the ionic current of the nanochannel caused by vesicle translocation. *Only vesicles in a certain size range can be analyzed due to size requirements in this strategy.* There are two geometric size thresholds that exist in this type of detection. First, some vesicles may not be detected if they are too large to pass through the nanochannel. At times this can be problematic and lead to the channel being blocked by larger particles. Blockage occurs randomly channels were unblocked by sonication or by rapidly changing the applied pressure and voltage. In some cases channels were unable to become unblocked. Secondly, some smaller vesicles are not detected because the change of the ionic current as they traverse the channel is not large enough to be detected by the nanochannel. For example the observed baseline current from the quartz nanochannel ($d_c = 570$ nm, $l_c = 6.8$ μ m) used for the detection of 100 nm vesicles at 1 V applied potential was roughly 40 nA with a RMS noise of 2.823 pA. In preliminary studies we observed that a value of 5 times the RMS noise was optimal threshold to use in the data analysis. When the threshold was set lower than that value it was observed upon manual inspection of the data that small fluctuations in the baseline current and random noise would be included as detection events. When analyzing the peaks from the current trace, a threshold of 5 times the RMS noise or 14.115 pA was used

thus eliminating any smaller pulses. This current threshold would correspond to a particle diameter of roughly 79 nm. Hence vesicles below that size would not be detected. In both these cases vesicles with diameters larger than the diameter of the channel and smaller than the detection limit are precluded in the analysis and the determined population statistics will differ. In order to offset these effects one can choose channel dimensions appropriate for the desired analysis. Knowing that vesicle samples can contain broad distributions of vesicle sizes, we chose to use larger diameter nanochannels so that we would include the bulk of the sample in our analysis. Because the size threshold exhibited by resistive-pulse sensing is dependent on both the channel diameter and length as shown in equation 1, with a larger diameter a shorter channel length is beneficial to lower the size detection threshold. For this reason we chose shorter channels when analyzing smaller vesicles to lower the size limit of detection.

7.3.4. Simultaneous Analysis of Nanoparticles and Vesicles

In order to explore the detection of mixtures of nanoparticles and vesicles, we sought to analyze solutions containing polystyrene particles of different sizes. Figure 7-5a is a plot of the particle size distribution from a current-time trace in a 0.1 M KCl solution containing 0.1% Triton X-100, 195-nm particles at nominal concentrations of 1.6×10^{10} particles/ml, and 375-nm particles at 1.6×10^{10} particles/ml. Two distinct populations of nanoparticles are clearly resolved, the first with a diameter of 210 ± 8 nm and the other of 393 ± 4 nm, both of which are in agreement with the DLS results. Although the concentrations of the particles were the same in solution, there were clearly less detection events for the larger particles. We observed roughly 600 events for the 195-nm particles and only ~100 for the 375-nm particles. We believe this is due to size exclusion due to geometric confinement of the nanochannel.²¹⁹ The effective concentration of the 375-nm particles is roughly 15% of that of the 195-nm particles inside a 470-nm nanochannel. Figure 7-5b contains a plot of the pulse width versus calculated particle size. The two distinct particle sizes are easily resolved. The size of the particle doesn't affect their translocation time, and larger particles translocate the channel at a similar velocity as the smaller ones. This is evident in the similarities between the pulse widths.

With the ability to discriminate between two different-sized particle populations, we desired to utilize the quartz nanochannels to analyze solutions containing both vesicles and nanoparticles. Figure 7-

6a shows current-time traces in a 1x PBS buffer, 0.002% Triton X-100 solution containing 20 mg/mL 100 nm DOPC vesicles with increasing amounts of 375 nm polystyrene nanoparticles. The same sample of vesicles was used and volumes of a polystyrene nanoparticle suspension were added to the sample yielding the concentrations shown. It can be qualitatively observed that as the amount of polystyrene spheres increases so do the counts of larger resistive pulses while the counts of vesicle detection events, smaller pulses, remains relatively unchanged. The current-time traces exhibit a stark contrast in the amplitude of the observed pulses and two distinct size ranges are observed. The observed particle size distributions coincide with the results for vesicle detection. Figure 7-6b contains the quantitative analysis and population distributions of the data from figure 7-6a. The two particle populations are easily resolved with the vesicle population centered around 160 nm and the polystyrene nanoparticles centered around 380 nm. The black trace is the solution before any nanoparticles have been added. In this sample the average vesicle diameter is 157 ± 22 nm and no polystyrene peaks are present. As the concentration of polystyrene spheres increases, a peak centered on 380 nm appears in the histogram which increases in size when more particles are added. As more polystyrene spheres are added there is a slight increase in the size of the smaller vesicle peaks and the population distribution broadens. We believe this result is a byproduct of adding surfactant to the solution as more polystyrene spheres are added. As shown in figure 7-6c, there is a linear dependence on the counts of polystyrene detection and the vesicle frequency is relatively unchanged. This experiment further demonstrates that we are indeed detecting polymer spheres and vesicles concurrently and that each particle population can be individually analyzed on the basis of their size.

7.4. Conclusions

Cylindrical quartz nanochannels have been used to analyze phospholipid vesicles and polystyrene nanoparticles using the resistive-pulse methods. Using these nanochannels we were able to analyze individual polystyrene nanoparticles and phospholipid vesicles in the range of 100 to 400 nm in diameter. Our results show that the particle size distributions obtained using quartz nanochannels are similar to those obtained from DLS and SEM. This is a powerful method for analyzing individual vesicles with several advantages compared to previous methods. First, it uses single glass nanochannels which can be

easily prepared from cheap materials using bench-top equipment. As an electronic-based technique, it allows for quick analysis of single vesicles within seconds. A limitation of this technique is that only particle size information can be determined from this method and if multiple particles types exist in a sample they will only be differentiated on the basis of size. However another distinct advantage of this method is that it can be combined with other analytical methods, such as amperometry and fluorescence microscopy, to yield more comprehensive information about biological and artificial vesicle samples.

7.5. Tables and Figures

Table 7-1. Measurements of polystyrene particle diameters using DLS, SEM, and nanochannel sensing.

Nominal size	DLS	SEM	Nanochannel
175 nm	194 ± 31	186 ± 7	198 ± 40
356 nm	375 ± 67	369 ± 6	378 ± 7

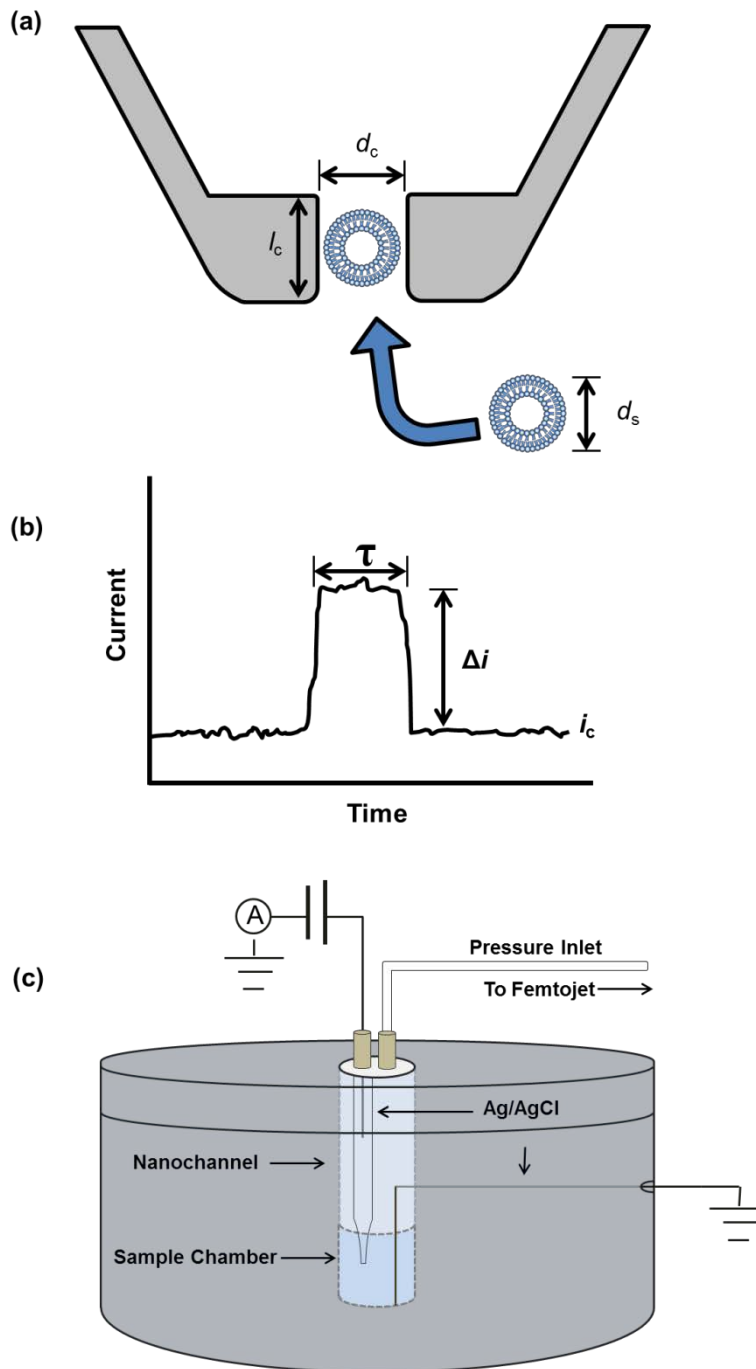


Figure 7-1. (a) A schematic diagram of a vesicle passing through a nanochannel. The length of the channel is given by l_c and the width by d_c , the diameter of the particle is d_s . (bottom) A current pulse caused by a vesicle passing through the channel. The pulse height, Δi , relative to the baseline current, i_c , reflects the change in the ionic resistance. τ is peak width and correlates to the amount of time the vesicle spends in the channel. (c) A schematic of the Lucite pressure cell constructed for this analysis.

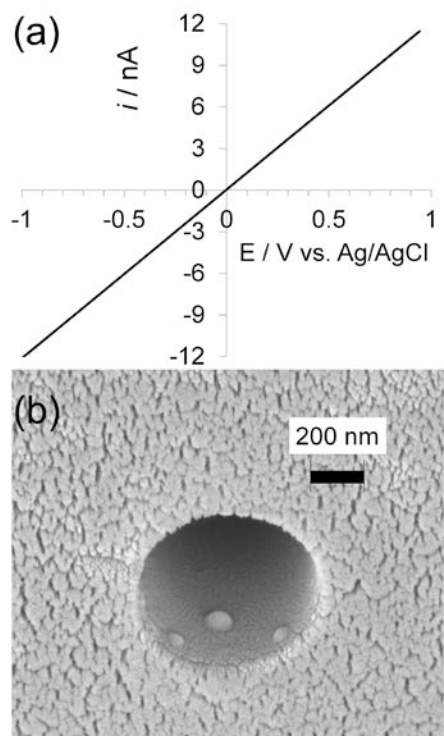


Figure 7-2. (a) An i - V response of a 640-nm-diameter quartz nanochannel in a 0.1 M KCl solution. (b) An SEM image of the same nanochannel.

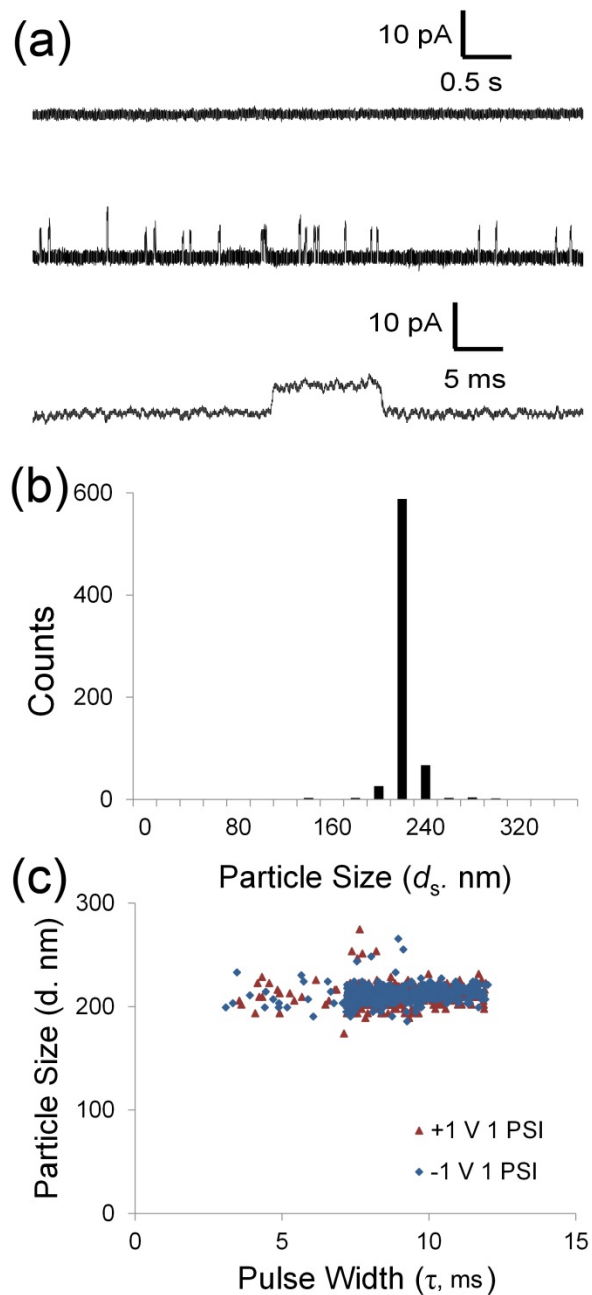


Figure 7-3. (a) Current–time traces for a quartz nanochannel ($l_c = 40 \mu\text{m}$, $d_c = 470 \text{ nm}$) in a 0.1 M KCl solution containing 0.1% Triton X-100 in the absence (top) and presence (middle) of 195 nm polystyrene spheres (1.8×10^{10} particles/mL) at a -1 V voltage bias and 1 PSI. (bottom) An individual detection event from the middle trace. (b) histogram of particle size detected by a nanochannel ($l_c = 40 \mu\text{m}$, $d_c = 470 \text{ nm}$) in a 0.1 M KCl and 0.1% Triton X-100 solution containing 195 nm polystyrene spheres (1.6×10^9 particles/mL) at voltage bias of -1 V and a pressure of 1 psi. (c) Plot of the calculated particle size versus the pulse width at +1 V applied voltage at the inner electrode (red), and -1 V applied voltage. In both cases a 1 PSI pressure was applied.

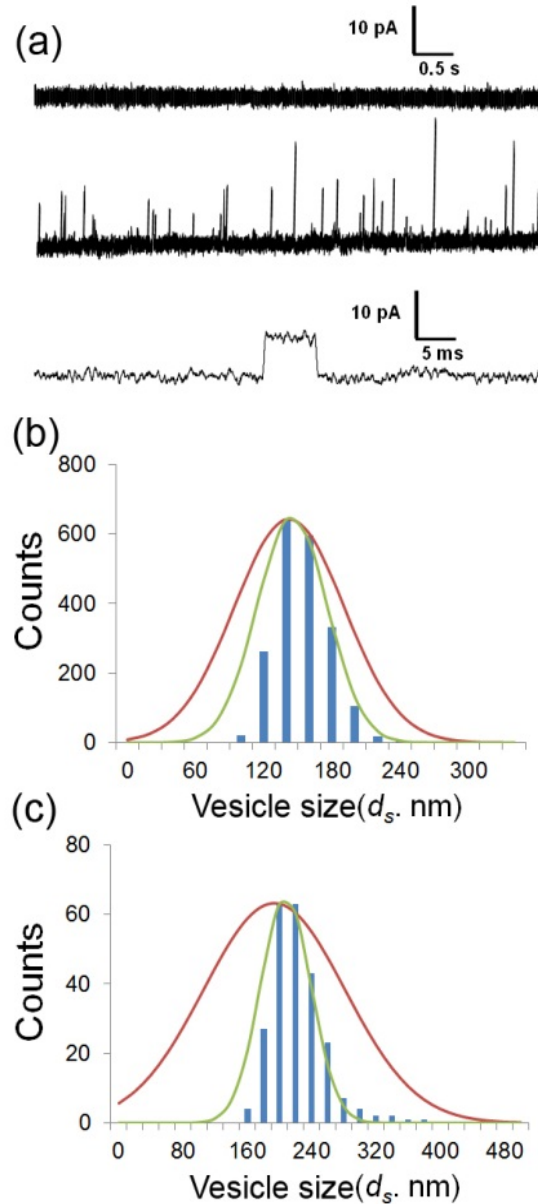


Figure 7-4 . (a) Current–time traces for a 430-nm nanochannel ($l_c = 21 \mu\text{m}$) in a 1x PBS buffer solution in the absence (top) and presence (middle) of 200 nm DOPC vesicles ($20 \mu\text{g}/\text{mL}$) at a -1 V voltage bias and 1 PSI. (bottom) Zoomed in current–time trace showing an individual detection event. (b) Histogram of vesicle size detected by a 570 nm nanochannel ($l_c = 7 \mu\text{m}$) in a 1x PBS buffer solution containing 100 nm DOPC Vesicles ($20 \mu\text{g}/\text{mL}$) at voltage bias of -1 V and 1 PSI. (c) Histogram of vesicle size detected by a 490 nm nanochannel ($l_c = 45 \mu\text{m}$) in a 1x PBS buffer solution containing 200 nm DOPC Vesicles ($20 \mu\text{g}/\text{mL}$) at voltage bias of -1 V and 1 PSI. Red curve represents the Gaussian distribution of particle size as determined by DLS, and the green curve represents a particle distribution as obtained from the nanochannel.

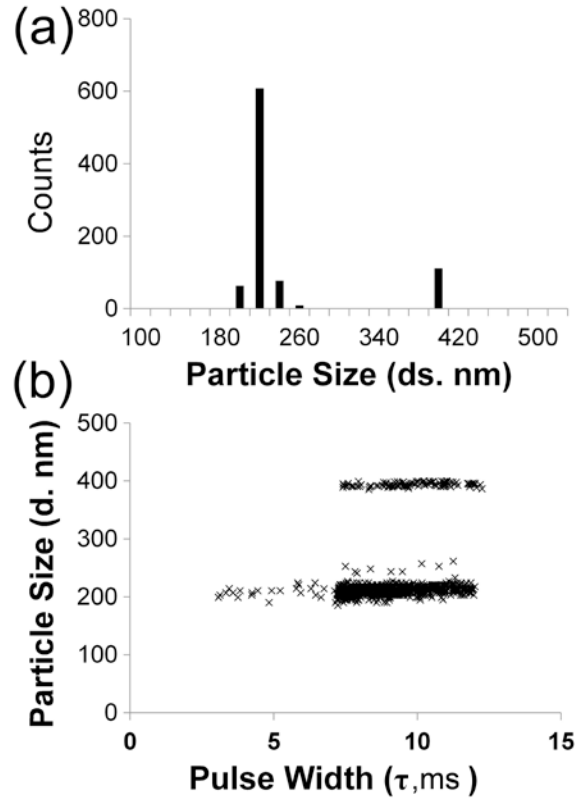


Figure 7-5. (a) Histogram of particle size detected by a 470-nm-diameter nanochannel ($l_c = 40 \mu\text{m}$) in a 0.1 M KCl and 0.1% Triton X-100 solution containing 195 nm and 375 nm polystyrene spheres (both at 1.6×10^9 particles/mL) at voltage bias of -1 V and a pressure of 1 PSI. (b) Relationship between pulse width and particle diameter for the mixed solution of 195 nm and 375 nm polystyrene spheres.

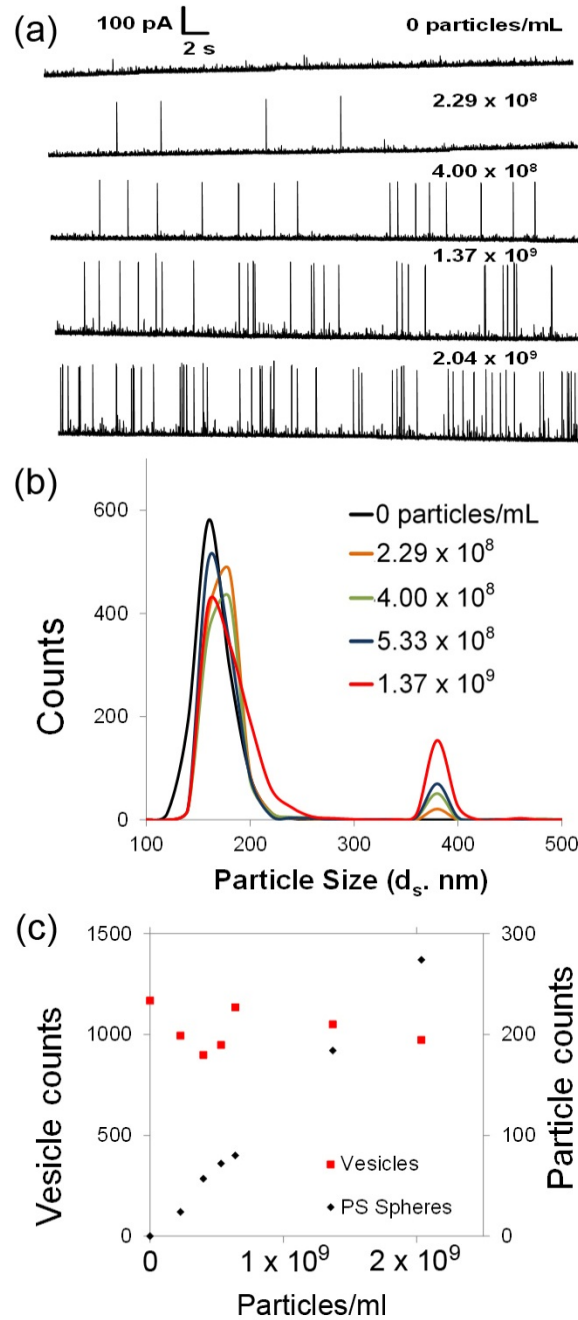


Figure 7-6. (a) Current-time traces for a 570-nm-diameter nanochannel (19.1 μm length) in a 1x PBS solution containing 0.002% Triton X-100 and 100 nm DOPC Vesicles (lipid concentration 20 $\mu\text{g}/\text{mL}$) with increasing concentrations of 375 nm polystyrene spheres at an applied potential of -1 V and a pressure of 1 PSI. Concentrations indicated reflect the concentration of polystyrene particles in the sample solution. (b) Histogram of additive particle detection data showing the population distributions of vesicles and increasing amounts of polystyrene spheres. (c) Particle detection counts plotted as a function of added polystyrene concentration.

BIBIOLGRAPHY

- (1) Wightman, R. M. *Analytical Chemistry* **1981**, *53*, 1125.
- (2) Penner, R. M.; Heben, M. J.; Longin, T. L.; Lewis, N. S. *Science* **1990**, *250*, 1118.
- (3) Morris, R. B.; Franta, D. J.; White, H. S. *Journal of Physical Chemistry* **1987**, *91*, 3559.
- (4) Bard, A. J.; Faulkner, L. R. *Electrochemical methods : fundamentals and applications*; 2nd ed.; Wiley: New York, 2001.
- (5) Wehmeyer, K. R.; Deakin, M. R.; Wightman, R. M. *Analytical Chemistry* **1985**, *57*, 1913.
- (6) Murray, R. W. *Chemical Reviews* **2008**, *108*, 2688.
- (7) Lanyon, Y. H.; Arrigan, D. W. M. *Sensors and Actuators B-Chemical* **2007**, *121*, 341.
- (8) Mirkin, M. V.; Fan, F. R. F.; Bard, A. J. *Journal of Electroanalytical Chemistry* **1992**, *328*, 47.
- (9) Watkins, J. J.; Zhang, B.; White, H. S. *Journal of Chemical Education* **2005**, *82*, 712.
- (10) Wang, G. L.; Zhang, B.; Wayment, J. R.; Harris, J. M.; White, H. S. *Journal of the American Chemical Society* **2006**, *128*, 7679.
- (11) Sun, P.; Mirkin, M. V. *Analytical Chemistry* **2006**, *78*, 6526.
- (12) Shao, Y. H.; Mirkin, M. V.; Fish, G.; Kokotov, S.; Palanker, D.; Lewis, A. *Analytical Chemistry* **1997**, *69*, 1627.
- (13) Sun, P.; Mirkin, M. V. *Analytical Chemistry* **2007**, *79*, 5809.
- (14) Zhan, D. P.; Velmurugan, J.; Mirkin, M. V. *Journal of the American Chemical Society* **2009**, *131*, 14756.
- (15) Li, Y.; Cox, J. T.; Zhang, B. *Journal of the American Chemical Society* **2010**, *132*, 3047.
- (16) Machado, S. A. S.; Tanaka, A. A.; Gonzalez, E. R. *Electrochimica Acta* **1991**, *36*, 1325.
- (17) Elliott, J. M.; Birkin, P. R.; Bartlett, P. N.; Attard, G. S. *Langmuir* **1999**, *15*, 7411.
- (18) Watkins, J. J.; Chen, J. Y.; White, H. S.; Abruna, H. D.; Maisonhaute, E.; Amatore, C. *Analytical Chemistry* **2003**, *75*, 3962.
- (19) Katemann, B. B.; Schuhmann, T. *Electroanalysis* **2002**, *14*, 22.
- (20) Sun, P.; Zhang, Z. Q.; Guo, J. D.; Shao, Y. H. *Analytical Chemistry* **2001**, *73*, 5346.
- (21) Liu, B.; Rolland, J. P.; DeSimone, J. M.; Bard, A. J. *Analytical Chemistry* **2005**, *77*, 3013.
- (22) Bach, C. E.; Nichols, R. J.; Beckmann, W.; Meyer, H.; Schulte, A.; Besenhard, J. O.; Jannakoudakis, P. D. *Journal of the Electrochemical Society* **1993**, *140*, 1281.
- (23) Schulte, A.; Chow, R. H. *Analytical Chemistry* **1996**, *68*, 3054.

- (24) Slevin, C. J.; Gray, N. J.; Macpherson, J. V.; Webb, M. A.; Unwin, P. R. *Electrochemistry Communications* **1999**, *1*, 282.
- (25) Zhang, B.; Galusha, J.; Shiozawa, P. G.; Wang, G. L.; Bergren, A. J.; Jones, R. M.; White, R. J.; Ervin, E. N.; Cauley, C. C.; White, H. S. *Analytical Chemistry* **2007**, *79*, 4778.
- (26) Arrigan, D. W. M. *Analyst* **2004**, *129*, 1157.
- (27) Zoski, C. G. *Electroanalysis* **2002**, *14*, 1041.
- (28) Cahill, P. S.; Walker, Q. D.; Finnegan, J. M.; Mickelson, G. E.; Travis, E. R.; Wightman, R. M. *Analytical Chemistry* **1996**, *68*, 3180.
- (29) Katemann, B. B.; Schumann, W. *Electroanalysis* **2002**, *14*, 22.
- (30) Li, Y.; Bergman, D.; Zhang, B. *Analytical Chemistry* **2009**, *81*, 5496.
- (31) Velmurugan, J.; Sun, P.; Mirkin, M. V. *Journal of Physical Chemistry C* **2009**, *113*, 459.
- (32) Jena, B. K.; Percival, S. J.; Zhang, B. *Analytical Chemistry* **2010**, *82*, 6737.
- (33) Zhang, B.; Zhang, Y. H.; White, H. S. *Analytical Chemistry* **2004**, *76*, 6229.
- (34) Agyekum, I.; Nimley, C.; Yang, C. X.; Sun, P. *Journal of Physical Chemistry C* **2010**, *114*, 14970.
- (35) Sun, Y.; Liu, Y. W.; Liang, Z. X.; Xiong, L.; Wang, A. L.; Chen, S. L. *Journal of Physical Chemistry C* **2009**, *113*, 9878.
- (36) Liu, Y. W.; He, R.; Zhang, Q. F.; Chen, S. L. *Journal of Physical Chemistry C* **2010**, *114*, 10812.
- (37) Liu, Y.; Zhang, Q.; Chen, S. *Electrochimica Acta* **2010**, *55*, 8280.
- (38) Lee, K. H.; Blaha, C. D.; Garris, P. A.; Mohseni, P.; Horne, A. E.; Bennet, K. E.; Agnesi, F.; Bledsoe, J. M.; Lester, D. B.; Kimble, C.; Min, H.-K.; Kim, Y.-B.; Cho, Z.-H. *Neuromodulation* **2009**, *12*.
- (39) Lama, R. D.; Charlson, K.; Anantharam, A.; Hashemi, P. *Analytical Chemistry* **2012**, *84*.
- (40) Kim, D.; Koseoglu, S.; Manning, B. M.; Meyer, A. F.; Haynes, C. L. *Analytical Chemistry* **2011**, *83*.
- (41) Adams, K. L.; Puchades, M.; Ewing, A. G. In *Annual Review of Analytical Chemistry* 2008; Vol. 1, p 329.
- (42) Kawagoe, K. T.; Zimmerman, J. B.; Wightman, R. M. *Journal of Neuroscience Methods* **1993**, *48*, 225.
- (43) Bruns, D. *Methods* **2004**, *33*.
- (44) Chen, T. K.; Luo, G. O.; Ewing, A. G. *Analytical Chemistry* **1994**, *66*.

- (45) Finnegan, J. M.; Pihel, K.; Cahill, P. S.; Huang, L.; Zerby, S. E.; Ewing, A. G.; Kennedy, R. T.; Wightman, R. M. *Journal of Neurochemistry* **1996**, *66*.
- (46) Sombers, L. A.; Hanchar, H. J.; Colliver, T. L.; Wittenberg, N.; Cans, A.; Arbault, S.; Amatore, C.; Ewing, A. G. *Journal of Neuroscience* **2004**, *24*, 303.
- (47) Schmitz, Y.; Lee, C. J.; Schmauss, C.; Gonon, F.; Sulzer, D. *Journal of Neuroscience* **2001**, *21*.
- (48) Chen, G. Y.; Gavin, P. F.; Luo, G. A.; Ewing, A. G. *Journal of Neuroscience* **1995**, *15*.
- (49) Schonfuss, D.; Reum, T.; Olshausen, P.; Fischer, T.; Morgenstern, R. *Journal of Neuroscience Methods* **2001**, *112*.
- (50) Ewing, A. G.; Wightman, R. M.; Dayton, M. A. *Brain Research* **1982**, *249*, 361.
- (51) Hochstetler, S. E.; Puopolo, M.; Gustincich, S.; Raviola, E.; Wightman, R. M. *Analytical Chemistry* **2000**, *72*.
- (52) Mosharov, E. V.; Sulzer, D. *Nature Methods* **2005**, *2*.
- (53) Wightman, R. M.; Jankowski, J. A.; Kennedy, R. T.; Kawagoe, K. T.; Schroeder, T. J.; Leszczyszyn, D. J.; Near, J. A.; Diliberto, E. J.; Viveros, O. H. *Proceedings of the National Academy of Sciences of the United States of America* **1991**, *88*.
- (54) Wipf, D. O.; Kristensen, E. W.; Deakin, M. R.; Wightman, R. M. *Analytical Chemistry* **1988**, *60*, 306.
- (55) Heien, M.; Johnson, M. A.; Wightman, R. M. *Analytical Chemistry* **2004**, *76*, 5697.
- (56) Sun, P. *Analytical Chemistry* **2010**, *82*, 276.
- (57) Adams, K. L.; Jena, B. K.; Percival, S. J.; Zhang, B. *Analytical Chemistry* **2011**, *83*, 920.
- (58) Zhang, B.; Wood, M.; Lee, H. *Analytical Chemistry* **2009**, *81*, 5541.
- (59) Rosi, N. L. M., C. A. *Chem. Rev.* **2005**, *105*, 1547.
- (60) Daniel, M. C. A., D. *Chem. Rev.* **2004**, *104*, 293.
- (61) Son, S. U. J., Y.; Park, J.; Na, H. B.; Park, H. M.; Yun, H. J.; Lee, J.; Hyeon, T. *J. Am. Chem. Soc.* **2004**, *126*, 5026.
- (62) Park, K. W. C., J. H.; Kwon, B. K.; Lee, S. A.; Sung, Y. E.; Ha, H. Y.; Hong, S. A.; Kim, H.; Wieckowski, A. *J. Phys. Chem. B* **2002**, *106*, 1869.
- (63) Gratzel, M. *J. Photochem. Photobiol A-Chem.* **2004**, *164*, 3.
- (64) Wang, Y. L., J. Y.; Deivaraj, T. C. *J. Electrochem. Soc.* **2004**, *151*, A1804.
- (65) Bell, A. T. *Science* **2003**, *299*, 1688.

- (66) Somorjai, G. A. C., A. M.; Montano, M.; Rioux, R. M. *Proc. Natl Acad. Sci. USA* **2006**, *103*, 10577.
- (67) Haruta, A. *Chem. Rec.* **2003**, *3*, 75.
- (68) Ye, H. C., R. M. *J. Am. Chem. Soc.* **2005** *127*, 4930.
- (69) Maillard, F. S., E. R.; Stimming, U. *J. Electroanal. Chem.* **2007**, *599*, 221.
- (70) Chen, W. K., J. M.; Sun, S. H.; Chen, S. W. *Langmuir* **2007**, *23*, 11303.
- (71) Markovic, N. M. S., T. J.; Stamenkovic, V.; Ross, P. N. *Fuel Cells* **2001**, *1*, 105.
- (72) Ahmadi, T. S. W., Z. L.; Green, T. C.; Henglein, A.; El-Sayed, M. A. *Science* **1996**, *272*, 1924.
- (73) Petroski, J. M. G., T. C.; El-Sayed, M. A. *J. Phys. Chem. A* **2001**, *105*, 5542.
- (74) Petroski, J. M. W., Z. L.; Green, T. C.; El-Sayed, M. A. *J. Phys. Chem. B* **2001**, *102*, 3316.
- (75) Inaba, M. A., M.; Hatanaka, A.; Nomoto, A.; Matsuzawa, K.; Tasaka, A.; Kinumoto, T.; Iriyama, Y.; Ogumi, Z. *Electrochim. Acta* **2006**, *52*, 1632.
- (76) Hernandez, J. S.-G., J.; Herrero, E.; Aldaz, A.; Feliu, J. M. *J. Phys. Chem. C* **2007**, *111*, 14078.
- (77) Solla-Gullon, J. V.-I., F. J.; Lopez-Cudero, A.; Garnier, E.; Feliu, J. M.; Aldaz, A. *Phys. Chem. Chem. Phys.* **2008**, *10*, 3689.
- (78) Stamenkovic, V. R. M., B. S.; Arenz, M.; Mayrhofer, J. J. J.; Lucas, C. A.; Wang, G. F.; Ross, P. N.; Markovic, N. M. *Nat. Mater.* **2007**, *6*, 241.
- (79) Somorjai, G. A. P., J. Y. *Topics in Catal.* **2008**, *49*, 126.
- (80) Crooks, R. M. Z., M.; Sun, L.; Chechik, V.; Yeung, L. K. *Acc. Chem. Res.* **2001**, *34*, 181.
- (81) Chen, M. G., D. W. *Acc. Chem. Res.* **2006**, *39*, 739.
- (82) Burda, C. C., X.; Narayanan, R.; El-Sayed, M. A. *Chem. Rev.* **2005**, *105*, 1025.
- (83) Lim, B. J., M.; Camargo, P. H. C.; Cho, E. C.; Tao, J.; Lu, X.; Zhu, Y.; Xia, Y. N. *Science* **2009**, *324*, 1302.
- (84) Ye, H. C., J. A.; Crooks, R. M. *Langmuir* **2007**, *23*, 11901.
- (85) Wang, C. D., H.; Lee, Y.; Kim, J.; Sun, S. *J. Am. Chem. Soc.* **2007**, *129*, 6974.
- (86) Cheng, W. D., S.; Wang, E. *Langmuir* **2002**, *18*, 9947.
- (87) Kumar, S. Z., S. Z. *Langmuir* **2009**, *25*, 574.
- (88) Ye, H. C. C., R. M. *J. Am. Chem. Soc.* **2007**, *129*, 3627.
- (89) Xiao, X. B., A. J. *J. Am. Chem. Soc.* **2007**, *129*, 9610.
- (90) Xiao, X. F., F.-R. F.; Zhou, J.; Bard, A. J. *J. Am. Chem. Soc.* **2008**, *130*, 16669.

- (91) Xiao, X. P., S.; Jang, J. S.; Fan, F.-R. F.; Bard, A. J. *J. Phys. Chem. C* **2009**, *113*, 14978.
- (92) Xu, W. S., H.; Kim, Y. J.; Zhou, X.; Liu, G.; Park, J.; Chen, P. *Nano Lett.* **2009**, in press.
- (93) Chen, S. L.; Kucernak, A. *Journal of Physical Chemistry B* **2004**, *108*.
- (94) Li, Y. B., D.; Zhang, B. *Anal. Chem.* **2009**, *81*, 5496.
- (95) Frens, G. *Nature* **1973**, *241*, 20.
- (96) Nath, N. C., A. *Anal. Chem.* **2004**, *76*, 5370.
- (97) Wang, G. Z., B.; Wayment, J. R.; Harris, J. M.; White, H. S. *J. Am. Chem. Soc.* **2006**, *128*, 7679.
- (98) Murray, R. W. *Acc. Chem. Res.* **1980**, *13*, 135.
- (99) Lenhard, J. R. M., R. W. *J. Electroanal. Chem.* **1977**, *78*, 195.
- (100) Chen, C. H. H., J. E.; Postlethwaite, T. A.; Richardson, J. N.; Murray, R. W. *Langmuir* **1994**, *10*, 3332.
- (101) Wang, Z. L. G., R. P.; Nikoobakht, B.; El-Sayed, M. A. *J. Phys. Chem. B* **2000**, *104*, 5417.
- (102) Grabar, K. C. S., P. C.; Musick, M. D.; Davis, J. A.; Walter, D. G.; Jackson, M. A.; Guthrie, A. P.; Natan, M. J. *J. Am. Chem. Soc.* **1996**, *118*, 1148.
- (103) Zhu, T. F., X.; Mu, T.; Wang, J.; Liu, Z. *Langmuir* **1999**, *15*, 5197.
- (104) Sun, P. M., M. V. *Anal. Chem.* **2006**, *78*, 6526.
- (105) Lanyon, Y. H. M., G. D.; Watson, Y. E.; Quinn, A. J.; Gleeson, J. P.; Redmond, G.; Arrigan, D. W. M. *Anal. Chem.* **2007**, *79*, 3048.
- (106) Kolb, D. M. P., M.; Gerische, H. J. *Electroanal. Chem.* **1974**, *54*, 25.
- (107) Tindall, G. W. B., S. *Electrochim. Acta* **1971**, *16*, 245.
- (108) Adzic, R. Y., E.; Cahan, B. D. *J. Electrochem. Soc.* **1974**, *121*, 474.
- (109) Tindall, G. W. C., S. H.; Bruckenstein, S. *J. Am. Chem. Soc.* **1969**, *91*, 2119.
- (110) Cadle, S. H. B., S. *Anal. Chem.* **1971**, *43*, 932.
- (111) Arrigan, D. W. M.; Iqbal, T.; Pickup, M. J. *Electroanalysis* **2001**, *13*.
- (112) Nakamura, M.; Endo, O.; Ohta, T.; Ito, M.; Yoda, Y. *Surface Science* **2002**, *514*.
- (113) Cadle, S. H. B., S. *Anal. Chem.* **1974**, *46*, 16.
- (114) Facci, J. M., R. W. *J. Electroanal. Chem.* **1980**, *112*, 221.
- (115) Biegler, T. R., D. A. J.; Woods, R. J. *Electroanal. Chem.* **1971**, *29*, 269.
- (116) Attard, G. S. B., P. N.; Coleman, N. R. B.; Elliott, J. M.; Owen, J. R.; Wang, J. H. *Science* **1997**, *278*, 838.
- (117) Peng, D. G., M.; Zhang, Q. *J. Phys. Chem. C* **2008**, *112*, 7036.

- (118) Brown, K. R. F., A. P.; Natan, M. J. *J. Am. Chem. Soc.* **1996**, *118*, 1154.
- (119) Shipway, A. N. K., E.; Willner, I. *ChemPhysChem* **2000**, *1*, 18.
- (120) Zhang, B. Z., Z.J.; Wang, B.; Yan, J.; Li, J. J.; Cai, S. M. *Acta Chim. Sinica* **2001**, *59*, 1932.
- (121) El-Deab, M. S. S., T.; Ohsaka, T. *Electrochem. Commun.* **2005**, *7*, 29.
- (122) Gong, K. D., F.; Xia, Z.; Durstock, M.; Dai, L. *Science* **2009**, *323*, 760.
- (123) Breiter, M. W. *Electrochimica Acta* **1996**, *11*, 905.
- (124) Johnson, D. C.; Napp, D. T.; Buckenst. *Electrochimica Acta* **1970**, *15*, 1493.
- (125) Rand, D. A. J.; Woods, R. *Journal of Electroanalytical Chemistry* **1972**, *35*, 209.
- (126) Kinoshita, K.; Lundquist, J. T.; Stonehart, P. *Journal of Electroanalytical Chemistry* **1973**, *48*, 157.
- (127) Ferreira, P. J.; la O, G. J.; Shao-Horn, Y.; Morgan, D.; Makharia, R.; Kocha, S.; Gasteiger, H. A. *Journal of the Electrochemical Society* **2005**, *152*, A2256.
- (128) Yasuda, K.; Taniguchi, A.; Akita, T.; Ioroi, T.; Siroma, Z. *Physical Chemistry Chemical Physics* **2006**, *8*.
- (129) Zhang, J.; Sasaki, K.; Sutter, E.; Adzic, R. R. *Science* **2007**, *315*, 220.
- (130) Ofstad, A. B.; Thomassen, M. S.; de la Fuente, J. L. G.; Seland, F.; Moller-Holst, S.; Sunde, S. *Journal of the Electrochemical Society* **2010**, *157*, B621.
- (131) Darling, R. M.; Meyers, J. P. *Journal of the Electrochemical Society* **2003**, *150*, A1523.
- (132) Sugawara, Y.; Okayasu, T.; Yadav, A. P.; Nishikata, A.; Tsuru, T. *Journal of the Electrochemical Society* **2012**, *159*.
- (133) Mitsushima, S.; Koizumi, Y.; Uzuka, S.; Ota, K. I. *Electrochimica Acta* **2008**, *54*, 455.
- (134) Sun, P.; Mirkin, M. V. *Journal of the American Chemical Society* **2008**, *130*, 8241.
- (135) Umeda, M.; Kuwahara, Y.; Nakazawa, A.; Inoue, M. *Journal of Physical Chemistry C* **2009**, *113*, 15707.
- (136) Sugawara, Y.; Yadav, A. P.; Nishikata, A.; Tsuru, T. *Journal of Electroanalytical Chemistry* **2011**, *662*.
- (137) Attard, G. S.; Bartlett, P. N.; Coleman, N. R. B.; Elliott, J. M.; Owen, J. R.; Wang, J. H. *Science* **1997**, *278*.
- (138) Guerrette, J. P.; Percival, S. J.; Zhang, B. *Langmuir* **2011**, *27*.
- (139) Bond, A. M.; Luscombe, D.; Oldham, K. B.; Zoski, C. G. *Journal of Electroanalytical Chemistry* **1988**, *249*, 1.

- (140) Feldberg, S. W.; Enke, C. G.; Bricker, C. E. *Journal of the Electrochemical Society* **1963**, 110.
- (141) Jerkiewicz, G.; Vatankhah, G.; Lessard, J.; Soriaga, M. P.; Park, Y. S. *Electrochimica Acta* **2004**, 49, 1451.
- (142) Yadav, A. P.; Nishikata, A.; Tsuru, T. *Journal of the Electrochemical Society* **2009**, 156.
- (143) Tseung, A. C. C.; Dhara, S. C. *Electrochimica Acta* **1975**, 20.
- (144) Shao-Horn, Y.; Sheng, W. C.; Chen, S.; Ferreira, P. J.; Holby, E. F.; Morgan, D. *Topics in Catalysis* **2007**, 46.
- (145) Mavre, F.; Anand, R. K.; Laws, D. R.; Chow, K.-F.; Chang, B.-Y.; Crooks, J. A.; Crooks, R. M. *Analytical Chemistry* **2010**, 82.
- (146) Klett, O.; Nyholm, L. *Analytical Chemistry* **2003**, 75.
- (147) Ordeig, O.; Godino, N.; del Campo, J.; Munoz, F. X.; Nikolajeff, F.; Nyholm, L. *Analytical Chemistry* **2008**, 80.
- (148) Zhan, W.; Alvarez, J.; Crooks, R. M. *Journal of the American Chemical Society* **2002**, 124.
- (149) Arora, A.; Eijkel, J. C. T.; Morf, W. E.; Manz, A. *Analytical Chemistry* **2001**, 73.
- (150) Chow, K.-F.; Mavre, F.; Crooks, R. M. *Journal of the American Chemical Society* **2008**, 130.
- (151) Chow, K.-F.; Chang, B.-Y.; Zaccheo, B. A.; Mavre, F.; Crooks, R. M. *Journal of the American Chemical Society* **2010**, 132.
- (152) Laws, D. R.; Hlushkou, D.; Perdue, R. K.; Tallarek, U.; Crooks, R. M. *Analytical Chemistry* **2009**, 81.
- (153) Dhopeswarkar, R.; Hlushkou, D.; Nguyen, M.; Tallarek, U.; Crooks, R. M. *Journal of the American Chemical Society* **2008**, 130.
- (154) Hlushkou, D.; Perdue, R. K.; Dhopeswarkar, R.; Crooks, R. M.; Tallarek, U. *Lab on a Chip* **2009**, 9.
- (155) Perdue, R. K.; Laws, D. R.; Hlushkou, D.; Tallarek, U.; Crooks, R. M. *Analytical Chemistry* **2009**, 81.
- (156) Hiddlest, J.; Douglas, A. F. *Nature* **1968**, 218.
- (157) Kazdoba, K.; Shvab, N.; Tsapakh, S. *Chemical Engineering Journal* **2000**, 79.
- (158) Ulrich, C.; Andersson, O.; Nyholm, L.; Bjorefors, F. *Analytical Chemistry* **2009**, 81.
- (159) Wang, Y.; Hernandez, R. M.; Bartlett, D. J., Jr.; Bingham, J. M.; Kline, T. R.; Sen, A.; Mallouk, T. E. *Langmuir* **2006**, 22.

- (160) Warakulwit, C.; Nguyen, T.; Majimel, J.; Delville, M.-H.; Lapeyre, V.; Garrigue, P.; Ravaine, V.; Limtrakul, J.; Kuhn, A. *Nano Letters* **2008**, *8*.
- (161) Ishiguro, Y.; Inagi, S.; Fuchigami, T. *Langmuir* **2011**, *27*.
- (162) Fosdick, S. E.; Crooks, R. M. *Journal of the American Chemical Society* **2012**, *134*.
- (163) Guerrette, J. P.; Oja, S. M.; Zhang, B. *Analytical Chemistry* **2012**, *84*, 1609.
- (164) Plana, D.; Jones, F. G. E.; Dryfe, R. A. W. *Journal of Electroanalytical Chemistry* **2010**, *646*, 107.
- (165) Hotta, H.; Akagi, N.; Sugihara, T.; Ichikawa, S.; Osakai, T. *Electrochemistry Communications* **2002**, *4*, 472.
- (166) Huffman, M. L.; Venton, B. J. *Analyst* **2009**, *134*.
- (167) Saito, Y. *Rev. Polarogr.* **1968**, *15*, 177.
- (168) Friend, J. A. N.; Smirles, W. N. *Journal of the Chemical Society* **1928**.
- (169) Song, C.; Zhang, J. In *PEM Fuel Cell Electrocatalysts and Catalyst Layers: Fundamentals and Applications*; Zhang, J., Ed. 2008; Vol. XXII, p 1137.
- (170) Cans, A.-S.; Ewing, A. G. *Journal of Solid State Electrochemistry* **2011**, *15*.
- (171) Leszczyszyn, D. J.; Jankowski, J. A.; Viveros, O. H.; Diliberto, E. J.; Near, J. A.; Wightman, R. M. *Journal of Biological Chemistry* **1990**, *265*.
- (172) Zerby, S. E.; Ewing, A. G. *Journal of Neurochemistry* **1996**, *66*.
- (173) Hermans, A.; Wightman, R. M. *Langmuir* **2006**, *22*.
- (174) Gerhardt, G. A.; Oke, A. F.; Nagy, G.; Moghaddam, B.; Adams, R. N. *Brain Research* **1984**, *290*.
- (175) Kristensen, E. W.; Kuhr, W. G.; Wightman, R. M. *Analytical Chemistry* **1987**, *59*.
- (176) Rice, M. E.; Oke, A. F.; Bradberry, C. W.; Adams, R. N. *Brain Research* **1985**, *340*.
- (177) Chen, R. S.; Huang, W. H.; Tong, H.; Wang, Z. L.; Cheng, J. K. *Analytical Chemistry* **2003**, *75*.
- (178) Swamy, B. E. K.; Venton, B. J. *Analyst* **2007**, *132*.
- (179) Hermans, A.; Seipel, A. T.; Miller, C. E.; Wightman, R. M. *Langmuir* **2006**, *22*.
- (180) Singh, Y. S.; Sawarynski, L. E.; Dabiri, P. D.; Choi, W. R.; Andrews, A. M. *Analytical Chemistry* **2011**, *83*, 6658.
- (181) Takmakov, P.; Zachek, M. K.; Keithley, R. B.; Walsh, P. L.; Donley, C.; McCarty, G. S.; Wightman, R. M. *Analytical Chemistry* **2010**, *82*, 2020.

- (182) Amatore, C.; Arbault, S.; Bouret, Y.; Guille, M.; Lemaitre, F.; Verchier, Y. *Analytical Chemistry* **2009**, *81*.
- (183) Wu, W. Z.; Huang, W. H.; Wang, W.; Wang, Z. L.; Cheng, J. K.; Xu, T.; Zhang, R. Y.; Chen, Y.; Liut, J. *Journal of the American Chemical Society* **2005**, *127*, 8914.
- (184) Wang, W.; Zhang, S. H.; Li, L. M.; Wang, Z. L.; Cheng, J. K.; Huang, W. H. *Analytical and Bioanalytical Chemistry* **2009**, *394*, 17.
- (185) Ge, S.; White, J. G.; Haynes, C. L. *Analytical Chemistry* **2009**, *81*, 2935.
- (186) Cox, J. T.; Guerrette, J. P.; Zhang, B. *Analytical Chemistry* **2012**, *84*, 8797.
- (187) Greene, L. A.; Sobeih, M. M.; Teng, K. K. Banker, G. and K. Goslin (Ed.). *Cellular and Molecular Neuroscience Series: Culturing Nerve Cells. Xiii+453p. Mit Press: Cambridge, Massachusetts, USA; London, England, Uk. Illus* **1991**, 208.
- (188) Kozminski, K. D.; Gutman, D. A.; Davila, V.; Sulzer, D.; Ewing, A. G. *Analytical Chemistry* **1998**, *70*.
- (189) Westerink, R. H. S.; Ewing, A. G. *Acta Physiologica* **2008**, *192*.
- (190) Bano, K.; Kennedy, G. F.; Zhang, J.; Bond, A. M. *Physical Chemistry Chemical Physics* **2012**, *14*, 4742.
- (191) Alberts, B.; Johnson, A.; Lewis, J.; Raff, M.; Roberts, K.; Peter, W. *Molecular Biology of the Cell*; Garland Science: New York, 2002.
- (192) Thery, C.; Ostrowski, M.; Segura, E. *Nature Reviews Immunology* **2009**, *9*, 581.
- (193) Sudhof, T. C. *Nature* **1995**, *375*, 645.
- (194) Jahn, R.; Sudhof, T. C. *Annual Review of Neuroscience* **1994**, *17*, 219.
- (195) Macdonald, R. C.; Macdonald, R. I.; Menco, B. P. M.; Takeshita, K.; Subbarao, N. K.; Hu, L. R. *Biochimica Et Biophysica Acta* **1991**, *1061*, 297.
- (196) Talmon, Y.; Burns, J. L.; Chestnut, M. H.; Siegel, D. P. *Journal of Electron Microscopy Technique* **1990**, *14*, 6.
- (197) Hallett, F. R.; Nickel, B.; Samuels, C.; Krygsman, P. H. *Journal of Electron Microscopy Technique* **1991**, *17*, 459.
- (198) Hallett, F. R.; Watton, J.; Krygsman, P. *Biophysical Journal* **1991**, *59*, 357.
- (199) Chong, C. S.; Colbow, K. *Biochimica Et Biophysica Acta* **1976**, *436*, 260.
- (200) Sun, B. Y.; Chiu, D. T. *Analytical Chemistry* **2005**, *77*, 2770.
- (201) Heider, E. C.; Peterson, E. M.; Barhoum, M.; Gericke, K.-H.; Harris, J. M. *Analytical Chemistry* **2011**, *83*, 5128.

- (202) Budzinski, K. L.; Allen, R. W.; Fujimoto, B. S.; Kensel-Hammes, P.; Belnap, D. M.; Bajjalieh, S. M.; Chiu, D. T. *Biophysical Journal* **2009**, *97*, 2577.
- (203) Sudhof, T. C.; Jahn, R. *Neuron* **1991**, *6*, 665.
- (204) Anderson, B. B.; Zerby, S. E.; Ewing, A. G. *Journal of Neuroscience Methods* **1999**, *88*, 163.
- (205) Coulter, W. H. United States, 1953.
- (206) Bayley, H.; Martin, C. R. *Chemical Reviews* **2000**, *100*, 2575.
- (207) Ito, T.; Sun, L.; Henriquez, R. R.; Crooks, R. M. *Accounts of Chemical Research* **2004**, *37*, 937.
- (208) Deblois, R. W.; Bean, C. P. *Review of Scientific Instruments* **1970**, *41*, 909.
- (209) Ito, T.; Sun, L.; Crooks, R. M. *Analytical Chemistry* **2003**, *75*, 2399.
- (210) Song, Y. X.; Zhang, H. P.; Chon, C. H.; Pan, X. X.; Li, D. Q. *Sensors and Actuators B-Chemical* **2011**, *155*, 930.
- (211) Piruska, A.; Gong, M.; Sweedler, J. V.; Bohn, P. W. *Chemical Society Reviews* **2010**, *39*, 1060.
- (212) Sexton, L. T.; Horne, L. P.; Sherrill, S. A.; Bishop, G. W.; Baker, L. A.; Martin, C. R. *Journal of the American Chemical Society* **2007**, *129*, 13144.
- (213) Fu, Y.; Tokuhisa, H.; Baker, L. A. *Chemical Communications* **2009**, 4877.
- (214) Saleh, O. A.; Sohn, L. L. *Proceedings of the National Academy of Sciences of the United States of America* **2003**, *100*, 820.
- (215) Saleh, O. A.; Sohn, L. L. In *Nano and Microsensors for Chemical and Biological Terrorism Surveillance*; Tok, J. B. H., Ed.; Royal Soc Chemistry, Thomas Graham House, Science Park, Cambridge Cb4 4wf, Cambs, Uk: 2008, p 60.
- (216) Hope, M. J.; Bally, M. B.; Webb, G.; Cullis, P. R. *Biochimica Et Biophysica Acta* **1985**, *812*, 55.
- (217) Gauthier, M. A.; Luo, J.; Calvet, D.; Ni, C.; Zhu, X. X.; Garon, M.; Buschmann, M. D. *Polymer* **2004**, *45*, 8201.
- (218) Lasic, D. D. *Liposomes in Gene Delivery*; CRC Press Inc: Florida, 1997.
- (219) Giddings, J. C.; Wiley: New York, 1991.

Curriculum Vitae

Jonathan T. Cox

EDUCATION

University of Washington, Seattle, WA Dec 2012
Ph.D. Analytical Chemistry

University of Utah, Salt Lake City, UT May 2008
B.S. in Chemistry, Minor in German

Salt Lake Community College, Salt Lake City, UT May 2006
A.S. in Chemistry

ACADEMIC AWARDS

- Outstanding Teaching Assistant for the 2010-2011 School year, Department of Chemistry, University of Washington
- Graduate Student Travel Award, University of Washington, 2011
- David A. Ritter Graduate Student Fellowship, University of Washington, 2008
- Research Internship for Scientists and Engineers (RISE), German Academic Exchange Service (DAAD), 2007
- Dean's List, University of Utah, 2007
- Honors at Entrance Scholarship, University of Utah, 2006
- Foundation Scholars Scholarship, Salt Lake Community College, 2003
- President's list during all semesters at Salt Lake Community College

RESEARCH AND LABORATORY EXPERIENCE

University of Washington, Seattle, WA Sep 2008 – Dec 2012
Graduate Student Research Assistant

- Research Advisor: Dr. Bo Zhang
- Research Mentor to Undergraduate students: Laura Belluzzi, Chan-li Chou, and Kayla Eychner

Tandem Laboratories, Salt Lake City, UT Jun 2008 – Sep 2008
Quality Control Auditor
Feb 2007 – Oct 2007
Technical Services Team

University of Utah, Salt Lake City, UT Oct 2007 – Jun 2008
Undergraduate Research Assistant

- Research Advisor: Dr. Joel M. Harris

Technische Universität Dortmund, Dortmund, Germany May 2007 – Aug 2007
DAAD-RISE Program Undergraduate Research Assistant

- Research Advisor: Dr. Börje Sellergren

TEACHING AND VOLUNTEER EXPERIENCE

University of Washington, Seattle, WA Sep 2011, Sep 2012
9th and 10th Annual TA/RA conference
Panel Moderator and Presenter TA/RA conference

Center for Teaching and Learning

University of Washington, Seattle, WA
Graduate Student Teaching Assistant and Lead Teaching Assistant

Sep 2008 – Jun 2012

Seattle Institute of Religion, Seattle, WA
Volunteer Teaching Faculty

Aug 2009 – Aug 2010

Salt Lake Community College, Salt Lake City, UT
Chemistry Tutor

Jan 2006 – May 2006

PUBLICATIONS

- Cox, J. T.; Li, Y.; Zhang, B. "The Stability of Platinum Nanoelectrodes in a Sulfuric Acid Solution under Potential Cycling" Manuscript in preparation, to be submitted to *Journal of Physical Chemistry C*
- Cox, J. T.; Zhang, B. "Using Bipolar Electrochemistry to Enhance Detection of Exocytosis from PC12 Cells with Carbon Fiber Microelectrodes" to be submitted to *Analytical Chemistry*.
- Cox, J. T.; Tomlinson, E.; Zhang, B. "Nanopore Analysis of Single Phospholipid Vesicles" to be submitted to *Analyst*.
- Cox, J. T.; Guerrette, J. P.; Zhang, B. "Steady-State Voltammetry of a Microelectrode in a Closed Bipolar Cell" *Analytical Chemistry*, 2012, 84 (20), pp. 8797-8804.
- Cox, J.T. ; Zhang, B. "Nanoelectrodes: Recent Advances in Fabrication and Application" *Annual Reviews of Analytical Chemistry*, Volume (5) 2012, pp. 253-272 (Invited)
- Li, Y.; Cox, J. T. ; Zhang, B. "Electrochemical Responses and Electrocatalysis at Single Au Nanoparticles" *Journal of the American Chemical Society*, 2010, 132 (9), pp. 3047-3054

PRESENTATIONS

- Cox, J. T., Plenary panel participant, 9th Annual TA/RA Conference on Teaching, Learning and Research at the University of Washington, Seattle, WA, Sep 2011.
- Cox, J.T., Jena, B. J., Li, Y., Percival, S. J., Zhang, B. "Electrochemistry and Electrocatalysis of Single Nanoparticles" PITTCOON 2011, SEAC Poster session, Atlanta, GA, Mar 2011.
- Cox, J. T. "Fire - How will we power our Planet?" Panel moderator and plenary session presenter, DAAD Alumni Conference New York, NY, Oct 2010.
- Cox, J. T.; Li, Y.; Zhang, B. "The Electrochemistry, Electrocatalysis and Photoenergy Conversion of Single Nanoparticles" NORM (Northwest Region of the American Chemical Society), Tacoma, WA, Jun 2009.